NASA TECHNICAL NOTE

NASA TN D-7192

NASA TN D-7192

EFFECT OF FINENESS RATIO ON BOATTAIL DRAG OF CIRCULAR-ARC AFTERBODIES HAVING CLOSURE RATIOS OF 0.50 WITH JET EXHAUST AT MACH NUMBERS UP TO 1.30

by David E. Reubush and Jack F. Runckel

Langley Research Center
Hampton, Va. 23665

NATIONAL AERONAUTICS AND SPACE ADMINISTRATION • WASHINGTON, D. C. • MAY 1973

1. Report No.	2. Government Accession No.	3. Recipient's Catalog No.
NASA TN D-7192		

4. Title and Subtitle	5. Report Date
EFFECT OF FINENESS RATIO ON THE BOATTAIL DRAG OF CIRCULAR-ARC AFTERBODIES HAVING CLOSURE RATIOS OF 0.50 WITH JET EXHAUST AT MACH NUMBERS UP TO 1.30	May 1973
	6. Performing Organization Code

7. Author(s)	8. Performing Organization Report No.
David E. Reubush and Jack F. Runckel	L-8705
	10. Work Unit No.
9. Performing Organization Name and Address	501-24-06-01
NASA Langley Research Center Hampton, Va. 23665	11. Contract or Grant No.
	13. Type of Report and Period Covered
12. Sponsoring Agency Name and Address	Technical Note
National Aeronautics and Space Administration Washington, D.C. 20546	14. Sponsoring Agency Code

15. Supplementary Notes

16. Abstract

An investigation has been conducted to determine the effect of fineness ratio on the drag of circular-arc boattails at subsonic and low supersonic speeds. The boattails had closure ratios of 0.50 and incorporated convergent nozzles. The investigation was conducted statically and at Mach numbers from 0.40 to 1.30 at 0^{o} angle of attack with jet total-pressure ratios varying from jet off to about 6, depending on Mach number. Low-fineness-ratio boattails (<1.00) had large separated-flow regions and the highest drag at all Mach numbers. Subsonic pressure-plus-friction drag levels were generally similar for boattails which did not have large separated regions. Drag-rise Mach number increased as boattail fineness ratio increased.

17. Key Words (Suggested by Author(s))	18. Distribution Statement
Afterbody drag Jet effects Jet engine exhaust nozzle	Unclassified – Unlimited

19. Security Classif. (of this report)	20. Security Classif. (of this page)	21. No. of Pages	22. Price*
Unclassified	Unclassified	92	$3.00

*For sale by the National Technical Information Service, Springfield, Virginia 22151

EFFECT OF FINENESS RATIO ON THE BOATTAIL DRAG OF CIRCULAR-ARC AFTERBODIES HAVING CLOSURE RATIOS OF 0.50 WITH JET EXHAUST AT MACH NUMBERS UP TO 1.30

By David E. Reubush and Jack F. Runckel
Langley Research Center

SUMMARY

An investigation has been conducted in the Langley 16-foot transonic tunnel to determine the effect of varying boattail fineness ratio on the drag of circular-arc boattails having a constant boattail closure ratio of 0.50. This investigation was conducted statically and at Mach numbers from 0.40 to 1.30 at 0^{o} angle of attack. Jet total-pressure ratio was varied from jet off to about 6, depending on Mach number. Reynolds number based on maximum model diameter varied from approximately 1.50×10^{6} to 2.14×10^{6}.

Results of this investigation indicate that below a Mach number of about 0.80 the total drag (pressure plus calculated skin friction) of all the configurations except the configuration with the lowest fineness ratio (0.80) is about the same when the configurations are compared at a typical full-scale engine operating pressure ratio; the low-fineness-ratio nozzle had higher drag because of extensive flow separation. At higher subsonic and low supersonic speeds, the higher the fineness ratio was, the lower the drag was. Also, drag-rise Mach number increased as boattail fineness ratio increased.

INTRODUCTION

Aircraft that must operate at both subsonic and supersonic speeds require propulsion nozzles with variable-geometry features for efficient performance over a wide range of engine power settings. Considerable research has been conducted on a wide variety of nozzle concepts to effect performance compromises between the internal propulsive performance and nozzle external drag (refs. 1 to 6). The actuation mechanisms needed for varying primary- and secondary-nozzle flaps, thrust reversers, and noise-suppression components can make the exhaust system quite heavy and result in a considerable impact on aircraft weight and balance. Efforts to reduce nozzle weight have led to shorter nozzles which usually have steep boattailed afterbodies during the subsonic portion of flight. Fighter-type airplanes, in particular, tend to incorporate low-fineness-ratio nozzles which may be prone to external flow separation. To assess the performance characteristics of some typical short exhaust nozzles and to provide information on the

drag reduction available by increasing the nozzle fineness ratio (ratio of afterbody length to maximum model diameter), a series of circular-arc boattailed convergent nozzles of varying fineness ratio have been investigated at subsonic and transonic speeds. The circular-arc shape was chosen since it generally corresponds to the shape of current military aircraft nozzles during subsonic cruise and it is a relatively simple geometric shape for theoretical calculations. The convergent internal contour was chosen since most multimission aircraft cruise at subsonic speeds with unaugmented power and with the nozzle in some configuration of the convergent type.

The present investigation was conducted in the Langley 16-foot transonic tunnel to determine the effect of varying nozzle boattail fineness ratio for a constant boattail closure ratio (0.50) corresponding to that typical for fighter airplane nozzles during subsonic cruise. Three nozzles with fineness ratios of 0.80, 1.00, and 1.77 were tested on a sting-strut-mounted air-powered nacelle model having a maximum diameter of 15.24 cm. The model configurations were investigated at 0° angle of attack at static conditions and at Mach numbers from 0.40 to 1.30 with variations in jet total-pressure ratio from jet off to about 6, depending on Mach number. Also included are data on the Supersonic Tunnels Association (STA) standard exhaust nozzle (described in ref. 1). This particular nozzle was tested previous to the tests of the other three nozzles and was mounted on a floor-strut support system because the sting-strut was not yet available. The STA nozzle has a fineness ratio of 1.29 and the same closure ratio as the other nozzles tested.

SYMBOLS

A cross-sectional area, m^2

A_b nozzle base area, m^2

A_{bel} effective annular area between metal bellows and surrounding sleeve, m^2

A_e nozzle exit area, m^2

A_m maximum cross-sectional area of model, m^2

A_t nozzle throat area, m^2

A_β incremental area assigned to a boattail static-pressure orifice for drag integration, m^2

C_D drag coefficient, $\frac{\text{Drag}}{qA_m}$

$C_{D,n}$ total boattail drag coefficient, $\frac{D_n}{qA_m}$

$C_{D,\beta}$ boattail pressure drag coefficient, $\frac{D_\beta}{qA_m}$

C_d discharge coefficient, $\frac{\dot{m}}{\dot{m}_i}$

$C_{F,s}$ stream thrust coefficient, $\frac{F_s}{A_e p_{t,j}}$

$C_{F,i}$ aerodynamic ideal thrust coefficient, $\frac{F_i}{qA_m}$

C_p boattail pressure coefficient, $\frac{p_\beta - p_\infty}{q}$

$C_{p,b}$ base pressure coefficient, $\frac{p_b - p_\infty}{q}$

$D_{f,cyl}$ calculated flat-plate skin-friction drag of cylindrical portion of model between stations 52.07 cm and 121.92 cm, N

$D_{f,n}$ calculated flat-plate skin-friction drag on boattail (i.e., aft of station 121.92 cm), N

D_n total drag of boattail, $D_\beta + D_{f,n}$, N

D_β pressure drag on boattail, N

d_b base diameter of afterbody, m

d_e exit diameter of nozzle, m

d_m maximum diameter of model, m

d_{th} throat diameter for STA nozzle, m

F_{bal} force measured by balance, N

F_i ideal isentropic gross thrust, $\dot{m}\sqrt{\frac{2\gamma}{\gamma - 1} RT_{t,j}\left[1 - \left(\frac{p_\infty}{p_{t,j}}\right)^{\frac{\gamma-1}{\gamma}}\right]}$, N

F_j nozzle gross thrust, $\dot{m}V_j + (p_e - p_\infty)A_e$, N

F_s stream thrust, $\dot{m}V_j + A_e p_e$, N

l length of boattail, m

M free-stream Mach number

M_l local internal Mach number in STA nozzle

$\dot{m}$ mass-flow rate measured by flow meter, kg/s

$\dot{m}_c$ mass-flow rate measured in high-pressure chamber, kg/s

$\dot{m}_i$ ideal mass-flow rate, $A_t p_{t,j}\sqrt{\frac{\gamma}{RT_{t,j}}\left(\frac{2}{\gamma + 1}\right)^{\frac{\gamma+1}{\gamma-1}}}$ for choked flow and

$A_t p_{t,j}\left(\frac{p_\infty}{p_{t,j}}\right)^{1/\gamma}\sqrt{\frac{2\gamma}{(\gamma - 1)RT_{t,j}}\left[1 - \left(\frac{p_\infty}{p_{t,j}}\right)^{\frac{\gamma-1}{\gamma}}\right]}$ for unchoked flow, kg/s

p_a ambient pressure, N/m^2

p_b base pressure, N/m^2

p_{bd} downstream bellows pressure, N/m^2

p_{bu} upstream bellows pressure, N/m^2

p_{cav} internal cavity pressure, N/m^2

p_e nozzle exit static pressure, N/m^2

$p_{t,j}$ jet total pressure, N/m^2

p_∞ free-stream static pressure, N/m^2

p_β boattail static pressure, N/m^2

q free-stream dynamic pressure, N/m^2

R gas constant, 287.3 N-m/kg-K; boattail circular-arc radius, m

r radial distance from center line of model, m

S nozzle convergence length, m

s axial coordinate in nozzle convergence section, m

$T_{t,j}$ jet stagnation temperature, K

t nozzle throat length, m

V_j jet exit velocity, m/sec

X axial distance aft from model nose, m

x axial distance aft from start of boattail, m

β terminal boattail angle, deg

β_c boattail chord angle, deg

γ ratio of specific heats

ϕ meridional angle about model axis, positive clockwise when viewed from rear, 0^o at top of model, deg

Abbreviation:

STA Supersonic Tunnels Association

APPARATUS AND PROCEDURE

Wind Tunnel

This investigation was conducted in the Langley 16-foot transonic tunnel, which is a single-return, continuous, atmospheric tunnel. The test section is a regular octagon in cross section with slots at the corners of the octagon. The tunnel speed is continuously variable from Mach 0.20 to 1.30. A description of the Langley 16-foot transonic tunnel can be found in references 7 and 8.

Model and Support Systems

A sketch of the single-engine nacelle model used in this investigation is shown in figure 1 with a typical circular-arc boattail configuration attached. Figure 2 is a photograph of the nacelle model installed in the Langley 16-foot transonic tunnel. The cone-cylinder nacelle had a rounded shoulder at the junction of the conical nose and cylindrical section. In this nacelle, dry, high-pressure air at a stagnation temperature of about 274 K is introduced perpendicularly to the model axis into the portion supported by the balance (shown by the fine hatching in fig. 1). Air passage from the high-pressure plenum to the low-pressure plenum is through eight sonic nozzles spaced at equal angles around the axis of the high-pressure plenum. Since the eight nozzles are not supported by the balance and the air is introduced perpendicularly to the model axis, the internal force measured by the balance is only the thrust developed by the rearward acceleration of the air. The low-pressure air chamber into which the air is introduced is sealed by a set of flexible metal bellows arranged so that axial forces caused by the pressurization of the system are compensating. The flow-smoothing screens in the model tailpipe were constructed of 0.635-cm-mesh, 0.0635-cm-diameter-wire screen supported by four vanes.

The model was supported in the tunnel by a sting-strut support system, the swept strut being attached to the nose of the model as shown in figures 1, 2, and 3. The center line of the model was located on the wind-tunnel center line, with the center line of the sting 55.88 cm below that level. The sting was 5.08 cm by 10.16 cm in cross section with the top and bottom capped by half-cylinders of 2.54-cm radius. The strut blade was 5 percent thick with a 50.8-cm chord in the streamwise direction and with leading and trailing edges swept 45°.

A sketch of the model and support system is shown in figure 3 along with corresponding cross-sectional area distributions. The model blockage was 0.099 percent of the test-section cross section, and the maximum blockage cross section of the model and support system was 0.148 percent. The sting-strut positioned the nose of the model at tunnel station 39.93 meters.

The model on which the STA standard exhaust nozzle was tested was nearly the same as the one used for this investigation except that it was slightly shorter and the nozzle boattail started at station 102.32 cm rather than at 121.92 cm as for the other configurations. Also differing was the support system used for the STA nozzle. This model was supported from the tunnel floor by a 5-percent-thick strut with its leading edge swept back 45° and trailing edge swept 52.5° with respect to the flow direction and having a 50.8-cm chord in the streamwise direction at the model center line. A photograph of the model with the STA nozzle installed and part of the support strut is shown in figure 4. The floor strut was located forward in the test section which positioned the model nose at tunnel station 39.20 meters with the model center line 91.40 cm below the tunnel center line. This type of support system had been used for earlier air-model investigations since the design was also adaptable for investigating the air-powered nacelle model in supersonic tunnels at Langley Research Center (ref. 2). Information on calibrations of the floor-strut model in the Langley 16-foot transonic tunnel is given in reference 1. A sketch of the model with the floor strut and the corresponding area distributions are shown in figure 5. The maximum blockage cross section of the model and support was 0.183 percent.

Afterbody Models

A detailed sketch of a typical afterbody model and a table of dimensions for the three configurations are presented in figure 6. The internal contour of each of the nozzles is essentially an ASME long-throat nozzle (ref. 9) modified to fit within dimensional constraints imposed by the external contour of each afterbody. The throat (length t in fig. 6) was circular in cross section. A photograph of the three models is shown in figure 7.

Details of the STA standard exhaust nozzle are shown in the sketch in figure 8. Accompanying the sketch is a table of dimensions and geometric parameters. The internal contour of this nozzle is also a modification of the ASME long-throat nozzle.

Instrumentation and Tests

The three basic afterbody models were equipped with static-pressure orifices distributed longitudinally on an equal-annular-area basis at the locations given in table I. Each model had 72 orifices which were connected to individual, remotely located, electrical pressure transducers. Simultaneously with the pressure measurements, forces and moments on the model downstream of the gap at model station 52.07 cm (see fig. 1) were measured by using a three-component strain-gage balance. Jet total pressure and temperature were measured in the internal flow just ahead of the nozzle connect station by use of an area-weighted five-tube total-pressure rake and a thermocouple (see figs. 1

and 6). A flowmeter with an axial-flow impeller was used to measure the mass flow of the simulator air.

Base pressures were obtained for each of the three configurations at jet-off conditions through the use of an instrumented base plate which fitted inside the nozzle and was flush with the exit. (Orifices were located on the plate at three points: (1) 2.79 cm from center toward 0°, (2) center, and (3) 2.79 cm from center toward 180°.)

The instrumentation for the test of the STA nozzle was slightly different from that just described. There were only 27 orifices on the surface of the afterbody and the distribution of the orifices was not on an equal-annular-area basis. (See table I.) Also, base pressures at jet-off conditions were obtained from two static orifices in the nozzle near the exit.

All tests were conducted in the Langley 16-foot transonic tunnel statically ($M = 0$) and at Mach numbers from 0.40 to 1.30 at an angle of attack of 0°. Model attitude was set so as to account for tunnel upflow, but no account was taken of possible sting deflection which was found to be extremely small. The ratio of jet total pressure to free-stream static pressure varied from jet off to approximately 6 (from jet off to approximately 16 for STA nozzle), depending on Mach number. While the Mach number and total-pressure ratio were held constant, 13 complete sets of force, moment, and pressure data were recorded; the average of these sets was used to compute the values of force, moment, and pressure coefficients and of jet stagnation temperature. The Reynolds number based on maximum diameter varied from approximately 1.50×10^6 to 2.14×10^6. Boundary-layer transition was fixed by a 0.254-cm strip of No. 100 grit, 2.54 cm from the nose, in accordance with techniques described in references 10 and 11.

Data Reduction

Pressure drag coefficients were computed from the measured pressures on each boattail. These coefficients are based on maximum cross-sectional area of the model and were obtained from the pressure data by assigning an equal annular area to each orifice in the top row and computing them from the equation

$$C_{D,\beta} = \frac{1}{qA_m} \sum_{i=1}^{10} (p_\infty - p_{\beta,i}) A_{\beta,i}$$

The top row of orifices was used exclusively because of the possibility of support-strut interference (see appendix) and the data from this row of orifices were found to be interference free. No attempt was made to include the forces on the small rim at the nozzle exit between d_b and d_e (see fig. 6).

Also, the validity of the step integration scheme employed here was checked if large pressure gradients existed. The accuracy of the step integration was spot checked by plotting C_p of the top row as a function of A/A_m and integrating with a planimeter.

For the STA nozzle, with far fewer pressure taps and taps not distributed on an equal-annular-area basis, the step-integration scheme was only valid at the lower Mach numbers (as pointed out in ref. 1). When the pressure distribution included steep or irregular gradients such as occur at high subsonic Mach numbers, this method tended to give erroneous answers so the planimeter method mentioned was used.

Thrust minus drag on the metric portion of the model was measured with an internal three-component strain-gage balance (see fig. 1). The forces measured by the balance F_{bal} include nozzle gross thrust F_j, external pressure and viscous forces from the gap station (52.07 cm) to the end of the boattail, and internal pressure tare forces. The nozzle thrust minus drag was computed by using the following equation:

$$F_j - D_n = F_{bal} + (p_{cav} - p_\infty)A_m + (p_{bd} - p_{bu})A_{bel} + D_{f,cyl}$$

In the foregoing expression, the first term on the right F_{bal} is the axial force indicated by the balance corrected for weight tares and balance interactions. The second term $(p_{cav} - p_\infty)A_m$ is a tare force which accounts for the difference between the pressure inside the model and free stream (see fig. 1). The cavity pressure was measured at 13 points within the model (10 for STA nozzle test), and each pressure was assumed to act on an element of area of which the sum equaled A_m, the maximum cross-sectional area. The third term $(p_{bd} - p_{bu})A_{bel}$ is a bellows tare correction (see fig. 1) which by design should be essentially zero. However, when internal flow velocities are large, a small pressure difference between the ends of the bellows can exist. In the present investigation the maximum bellows tare correction was about 0.5 percent of ideal gross thrust F_i. The test of the STA nozzle had only an upstream bellows pressure measurement and, as such, the tare could not be evaluated; as a result, the measured thrust is too high. The last term $D_{f,cyl}$ is the calculated flat-plate skin-friction drag on the cylindrical portion of the model between the metric break and the start of the afterbody (between stations 52.07 cm and 121.92 cm).

The static thrust performance (gross thrust) was obtained at $M = 0$ from the preceding expression for $F_j - D_n$, since the external drag force is zero and no detectable induced flow effects were observed from the boattail pressure measurements. Nozzle internal gross thrust was obtained for wind-on operation at various Mach numbers from the relation

$$F_j = (F_j - D_n) + D_\beta + D_{f,n}$$

where D_β is the boattail pressure drag obtained from the integration of all pressure orifices and $D_{f,n}$ is the calculated skin friction on the boattail only.

The stream thrust was obtained from the static gross thrust by adjusting for the ambient pressure area term as follows:

$$F_s \equiv \dot{m}V_j + p_e A_e = F_j + p_a A_e$$

The boattail drag was obtained from the force balance measurement for jet-off conditions only by adjusting the balance data to eliminate the base drag as follows:

$$D_n = -\left[F_{bal} + (p_{cav} - p_\infty)A_m + D_{f,cyl}\right] + (p_b - p_\infty)A_b$$

where p_b is the average of the pressures on the base plate and A_b is the base area (see fig. 6). A comparison was made between the boattail drag obtained from the balance and that obtained by using all the pressure orifices with calculated flat-plate skin friction added.

PRESENTATION OF RESULTS

The results obtained in this investigation are presented in the following figures.

DISCUSSION

Jet-Off Measurements

Pressure distributions.- Presented in figure 9 are jet-off longitudinal pressure distributions for all four configurations at various Mach numbers. The pattern of the pressure distributions depicted in these plots shows that the steep, low-fineness-ratio configurations having the highest rates of boattail curvature cause rapid flow accelerations over the boattail which result in an expansion region with the lowest pressures occurring at about one-fourth of the boattail length. As fineness ratio is increased, the rate of boattail curvature becomes less and the negative pressure peaks diminish in magnitude. The expansion region is followed by a recompression and the steeper boattails have tendencies to compress further on the rear portion in accordance with potential flow theory. Rapid recompression on the boattails, however, promotes separation of the flow over the rear of the steeper boattails. The uniformity of the pressure coefficients on the rear portion of configuration 1 $\left(l/d_m = 0.80\right)$ indicates that the flow over this boattail is substantially separated for all test Mach numbers, and the flow over configuration 2 $\left(l/d_m = 1.00\right)$ is at least partially separated for all test Mach numbers. The data for the STA configuration $\left(l/d_m = 1.29\right)$ do not seem to indicate separation until a shock has formed on the boattail (shock-induced separation). The boattail with the highest fineness ratio, configuration 3, has the least expansion and compression and exhibits the smallest pressure variation with change in Mach number because it reaches critical pressure coefficients at a higher Mach number than the other configurations.

Also shown in these plots (as solid symbols) are base pressure coefficients obtained with the base plates (configurations 1, 2, and 3). Although the pressure coefficient distributions shown were obtained without the base plates in place, the base pressure coefficients are in good agreement with them.

Base pressures.- Figure 10 presents the jet-off base pressure coefficients for all configurations as a function of Mach number. Generally, all four have positive base pressure coefficients below a Mach number of about 0.90. At supersonic speeds the base pressure coefficients tend to remain relatively constant for a given configuration, with the highest fineness ratio afterbody having the highest pressures.

Jet-off drag variation with Mach number.- Shown in figure 11 are the variations of jet-off pressure drag with Mach number for all four configurations. As was expected, based on the results of reference 4, the lower the fineness ratio is, the lower the drag-rise Mach number is, and the higher the supersonic drag is. (The drag-rise Mach number is indicated by the intersection of a linear fairing through the subsonic slope of the drag curve with a linear extrapolation of the steep supercritical portion of the curve for this paper.) The two lower fineness ratio afterbodies do not have the highest subsonic

drag before the drag rise, as would be expected. Configuration 3 $(l/d_m = 1.77)$ has the lowest drag at all subsonic Mach numbers, configuration 1 $(l/d_m = 0.80)$ has the second lowest drag before its drag rise, configuration 2 $(l/d_m = 1.00)$ has next to the highest drag before its drag rise, and the STA $(l/d_m = 1.29)$ has the highest drag before the drag rises of the two lower fineness ratio afterbodies. The reason that these two configurations have relatively lower drag than would be expected can be shown by figure 12 in which the pressure coefficient distributions for configurations 1 and 2 at three representative Mach numbers are shown as a function of A/A_m. At $M = 0.40$ the drag levels of both configurations are about the same (fig. 11) and, correspondingly, in figure 12 the total areas (algebraic sum of area enclosed by negative part of pressure coefficient curve and area enclosed by positive part of pressure coefficient curve) under both curves are about the same; at $M = 0.70$ the drag of configuration 1 is lower and, correspondingly, the total area (which has a negative sign) under the curve is smaller for configuration 1 than for configuration 2; and at $M = 0.92$ the drag of configuration 1 is much higher than that for configuration 2 and, correspondingly, the negatively signed area under the curve for configuration 1 is much larger. These comments would also apply if both of these configurations were compared with the STA nozzle. At $M = 0.40$ all three have about the same drag and therefore the same area under their pressure coefficient curves; at $M = 0.70$ the STA would have a larger (negative) area under its pressure coefficient curve and thus higher drag; and at $M = 0.92$ the STA would have less area (negative) under its pressure coefficient curve and, as a result, a correspondingly lower drag.

Jet-On Measurements

Effect of jet operation on pressure coefficient distributions.- Figure 13 shows the effect of jet total-pressure ratio on the longitudinal pressure distributions for configuration 1 $(l/d_m = 0.80)$ at the test Mach numbers. For this configuration there were only small increases in boattail pressure coefficients with jet operation until a Mach number of about 0.92. At Mach numbers of 0.92 to 0.96, operation of the jet caused a reduction in the pressures in the separated region after the shock (as found in ref. 12). At supersonic speeds, turning the jet on lowered the pressures in the separated region after the shock whereas the further increase in pressure ratio to the maximum resulted in a higher than jet-off pressure level in the separated region (where the underexpanded jet is obviously pressurizing the separated region).

Longitudinal pressure distributions at various Mach numbers are shown in figure 14 for configuration 2 $(l/d_m = 1.00)$. Generally, at subsonic speeds, operation of the jet resulted in higher pressures over most, if not all, of the boattail; the largest effect on the pressures occurred when the jet was turned on and further increases in jet total-pressure ratio did not appreciably affect the distribution. At supersonic speeds the reverse was true, and turning the jet on had little, if any, effect whereas the increase in

pressure ratio to the maximum did increase pressures downstream of the shock and moved the shock forward on the boattail.

Figure 15 shows the distributions for the STA configuration $\left(l/d_m = 1.29\right)$ at various Mach numbers and pressure ratios. This afterbody was tested over a much larger pressure-ratio range than any of the other configurations. However, the largest relative changes are still observed when the jet is turned on at subsonic speeds (a discussion of this phenomenon can be found in ref. 13) and when the pressure ratio is increased to the maximum at supersonic speeds. Also, it must be noted that in contrast to the effects observed on the highly separated boattails of configurations 1 and 2, the effects of jet operation are relatively greater in magnitude at all Mach numbers for this boattail. That is, as the amount of separation decreases the effect of the jet increases (especially after the flow has become supercritical).

Shown in figure 16 are the jet-on longitudinal pressure distributions at several jet total-pressure ratios and Mach numbers for configuration 3 $\left(l/d_m = 1.77\right)$. At subsonic speeds these results are similar to those found for the STA configuration in that the largest effects (for the test range of pressure ratios) occurred when the jet was first turned on.

Comparison with theory.- Shown in figure 17 are comparisons of the measured pressure distributions at two representative Mach numbers (0.40 and 0.80) for the configurations at a pressure ratio of 2 with the theory of reference 14 using a circular cylinder to simulate the jet shape (this theory includes a correction for compressibility effects but does not include any correction for viscous effects). It was believed that this theory would be representative of the current state of the art in theoretical prediction techniques and that using a circular cylinder would be representative of the jet shape for the nozzle at design pressure ratio. As can be seen the theory predicts the minimum negative pressure levels for all the configurations at both Mach numbers very well. Also, it predicts most of the distributions for configurations 1 and 2 at $M = 0.40$ and configuration 3 and the STA configuration at both Mach numbers fairly well; it breaks down only near the end of the boattail where the theory forces the flow toward a stagnation point. However, the predictions for configurations 1 and 2 are not too good at $M = 0.80$ where the flow over both has separated. It must therefore be concluded that present theoretical techniques are good for predicting pressure distributions for nonseparated configurations in clean uniform flow fields but are not good for configurations on which separation has occurred.

Effect of jet operation on boattail drag.- Figures 18 to 21 present integrated boattail pressure drag coefficients as a function of jet total-pressure ratio for all four configurations at most test Mach numbers. Similarly, boattail total drag coefficients (pressure plus calculated skin friction) as a function of pressure ratio are shown in figures 22

to 25. The following comments apply to either drag coefficient since skin friction is constant for a given configuration at a given Mach number. Flags on symbols indicate repeat points.

The results for configuration 1 $\left(l/d_m = 0.80\right)$ are shown in figures 18 and 22. At Mach numbers below about 0.92, there was little effect of the jet on boattail drag when the jet was choked. At Mach numbers of 0.94 and 0.96, increasing jet total-pressure ratio resulted in increasing boattail drag. At supersonic speeds, boattail drag increased as the pressure ratio was increased until a pressure ratio of about 3 was reached, at which point further increases in pressure ratio reduced the drag from the maximum value.

Shown in figures 19 and 23 are results for configuration 2 $\left(l/d_m = 1.00\right)$. At subsonic Mach numbers, turning the jet on generally decreased boattail drag, but further increases in pressure ratio had little effect. At supersonic speeds, the results were similar to those found for configuration 1 except the peak drag at $p_{t,j}/p_\infty = 3$ was not as far above the jet-off value as that for configuration 1.

Figures 20 and 24 present the results for the STA configuration $\left(l/d_m = 1.29\right)$. At subsonic Mach numbers, increasing jet total-pressure ratio generally reduced boattail drag. (Data at high pressure ratios are shown for $C_{D,n}$ to illustrate large effects possible for high pressure ratios.) At supersonic Mach numbers, increasing jet total-pressure ratio also resulted in decreased boattail drag.

Results for configuration 3 $\left(l/d_m = 1.77\right)$ are presented in figures 21 and 25. Generally, for both subsonic and supersonic speeds, increasing jet total-pressure ratio resulted in decreased boattail drag for this configuration.

In summary, jet operation generally decreased boattail pressure drag on configurations having fineness ratios of 1.0 or greater. The shortest boattail $\left(l/d_m = 0.80\right)$ had extensive areas of separation; jet operation aspirated the separated region which caused the drag to increase, particularly at the higher subsonic Mach numbers.

Figure 26 is a plot of the jet total-pressure ratio as a function of Mach number for a typical fighter airplane. This pressure-ratio schedule is used in the following analysis of the previously shown drag data.

Cross plots of the boattail pressure drag coefficients of the various configurations at the schedule of figure 26 are shown in figure 27. As was expected, generally the higher the fineness ratio was, the lower the pressure drag (both at subsonic and supersonic speeds) was, and the higher the drag-rise Mach number was. The jet-off anomaly (fig. 11) is therefore attributed to base effects.

Figure 28 presents the total (pressure plus friction) drag coefficients cross-plotted at the pressure-ratio schedule of figure 26. As was found in reference 4, at subsonic Mach numbers below about 0.80 the addition of the friction drag to the pressure

drag results in a total boattail drag which is about the same for all configurations except configuration 1 $\left(l/d_m = 0.80\right)$ which was higher than the rest because of extensive flow separation. Above $M = 0.80$ the higher skin-friction drag for the higher fineness ratio afterbodies was not enough to offset the lower pressure drag; as a result, for all Mach numbers above about 0.80 the higher the fineness ratio was, the lower the drag was. Also, the higher the fineness ratio was, the higher the drag-rise Mach number was.

FORCE DATA

Figures 29 to 37 present the force data obtained from this investigation. The results for the STA configuration are generally presented separately from the data. As pointed out previously the thrust measurements are believed to be slightly high because the bellows-tare-correction term could not be evaluated.

Static Performance

The variation of nozzle internal performance (thrust ratio) with jet total-pressure ratio for configurations 1, 2, and 3 is presented in figure 29 for static conditions. Also shown are the theoretical one-dimensional thrust-ratio variation and thrust ratios for a long-radius ASME nozzle (ref. 9). The thrust ratios are in good agreement with those of reference 15 in the choked pressure-ratio range. However, at pressure ratios below the critical, data scatter increases due to inherent inaccuracies of the measuring equipment in the low-output range. Results from two separate runs are shown to indicate data repeatability.

Mass-flow ratios (discharge coefficients C_d) at static conditions (fig. 30) show the expected high values for long-radius-throat ASME-type nozzles operating at high Reynolds numbers (ref. 9). As with the thrust-ratio plots, results from two runs are shown to indicate data repeatability.

Figure 31 shows both thrust and mass-flow ratios for the STA nozzle. Due to the unevaluated tare correction, thrust ratios equal to or greater than one-dimensional values were measured with this nozzle. Two mass-flow measurements are presented for this nozzle, one based on flow meter data and the other based on instrumentation installed in the high-pressure plenum. Both methods provide about the same value of discharge coefficient. Again the values are as expected for a long-radius ASME-type nozzle operating at high Reynolds numbers.

Stream thrust coefficients for static tests are presented in figure 32. Data for configurations 1, 2, and 3 are shown in figure 32(a) and these results are compared with one-dimensional theoretical values. As would be expected for nozzles having similar interior contours, the values are about the same for all three configurations. A similar com-

parison is shown in figure 32(b) for the STA nozzle. This nozzle had slightly higher values since the thrust-ratio measurements were high (fig. 31). Above a pressure ratio at which the flow is choked, the stream thrust coefficient of a convergent nozzle remains constant.

Local internal Mach numbers for the STA nozzle calculated from wall static-pressure measurements and the average rake total pressure are shown in figure 33. The Mach number indicated by these measurements was subsonic in the forward cylindrical throat region and tends to be supersonic near the wall at the exit station. A local supersonic region near this wall exit has been found for nozzles having zero convergence at the exit because of the curvature of the Mach line such as shown by the measurements presented in reference 16. The two-dimensional effects of sonic-line curvature can have a major influence on convergent-nozzle internal performance (ref. 17).

Wind-On Performance

The variation of thrust-minus-drag ratio with jet total-pressure ratio at several Mach numbers is shown in figure 34 for all configurations. As previously noted, the values for the STA nozzle are high relative to the other configurations because of higher, but not fully adjusted, measured internal performance; the data points are therefore not faired. This is evident in figure 34(a) where the STA values would be expected to fall between those for configurations 2 and 3 but, in fact, are higher than those for all the other configurations. At the higher Mach numbers (figs. 34(b) and (c)) the comparison is more representative because of the greater influence of external drag.

The variation of internal performance F_j/F_i with jet total-pressure ratio is given in figure 35 for several Mach numbers. The external airstream effects on internal performance do not appear significant with a data scatter of about ±1 percent relative to static thrust values (figs. 29 and 31) at the higher pressure ratios. One-dimensional theory is indicated in figure 35 for reference. Again the STA results are presented separately due to the higher uncorrected data for this nozzle.

In figure 36 jet-off boattail total drag coefficients for the various configurations found by using data from all pressure orifices are compared with the corresponding total drag coefficients found by using the force data corrected for base drag and base-plate effects. The correlation is generally not good. It is believed that the primary reason for this is that the balance (which is accurate to ±0.5 percent of full scale) was sized for the maximum anticipated thrust (3558 N) and with the jet off it was only measuring drag on the order of, at most, 111 N. An error on the order of 0.5 percent of full scale on the balance would be on the order of 16 percent or greater in drag. The STA force measurements, which are known to be high, are indicated by solid symbols.

Values of $C_{F,i} = F_i/qA_m$ are plotted in figure 37 as a function of jet total-pressure ratio for the nozzles of this investigation at various Mach numbers. These plots can be used to convert from aerodynamic coefficients based on qA_m to propulsion coefficients based on F_i.

CONCLUSIONS

An investigation at 0^o angle of attack has been conducted in the Langley 16-foot transonic tunnel at Mach numbers from 0.40 to 1.30 to determine the effects of variations in boattail fineness ratio (ratio of boattail length to maximum diameter l/d_m) on the boattail drag of circular-arc boattails having a constant boattail closure ratio (ratio of nozzle exit diameter to maximum diameter d_e/d_m) of 0.50. The results of this investigation indicate the following conclusions:

1. At subsonic speeds, the lower the afterbody fineness ratio was, the lower the negative pressure in the expansion region of the boattail was, and the higher the positive pressure in the recompression region was (if separation has not occurred). At supersonic speeds, the higher the fineness ratio was, the higher the level of pressures on the afterbody was before the shock.

2. Drag-rise Mach number increased with increasing boattail fineness ratio with the jet both off and on.

3. Jet operation generally decreased boattail pressure drag on configurations having fineness ratios of 1.0 or greater. The shortest boattail $(l/d_m = 0.80)$ had extensive areas of separation; jet operation aspirated the separated region which caused the drag to increase, particularly at the higher subsonic Mach numbers.

4. At Mach numbers below about 0.80, the total drag (pressure plus calculated skin friction) of all the configurations except the configuration with the lowest fineness ratio $(l/d_m = 0.80)$ is about the same when the configurations are compared at a scheduled pressure ratio; the low-fineness-ratio nozzle had higher drag because of extensive flow separation.

Langley Research Center,
National Aeronautics and Space Administration,
Hampton, Va., April 10, 1973.

APPENDIX

STRUT INTERFERENCE EFFECTS

References 1 and 4 have indicated that for some configurations there is interference from the support system on the measured boattail pressures. The results of investigating this phenomenon for the configurations of this test are presented in figures 38 to 43.

Jet-off pressure-coefficient data from three axial rows of orifices (0^o, 90^o, and 180^o) were plotted as a function of x/l for the four configurations at three representative Mach numbers (fig. 38). At subsonic speeds it was found that there was an effect of the strut (for configurations 1 and 2 of the sting-strut-supported models and the strut-supported STA model) which primarily affected pressures in the expansion regions of the boattails and caused the pressures in the 90^o and 180^o rows to be lower than these in the 0^o row (larger effect in the 180^o row which was directly behind strut). This effect increased with a decrease in fineness ratio or an increase in subsonic Mach number. At supersonic speeds there was no discernible effect for any configuration. To illustrate more fully the subsonic effects, the remaining subsonic longitudinal pressure coefficient distributions ($\phi = 0^o$, 90^o, and 180^o) for configuration 2 $\left(l/d_m = 1.00\right)$ on the sting-strut and the STA $\left(l/d_m = 1.29\right)$ on the strut are presented in figures 39 and 40. Both configurations exhibit similar effects which increase with Mach number, and configuration 2, with its lower fineness ratio, exhibits larger effects than does the STA configuration.

Although the data of references 1 and 4 had indicated that there would be support interference effects, a prior check of the sting-strut with a cylindrical afterbody longer than any of the test configurations had indicated no variation in static pressure around the afterbody. Figure 41 shows the results of this check at three representative Mach numbers with the relative locations of the three configurations of this test shown above the plot. It is therefore believed that the strength of the interference is in some way tied in with the magnitude of the pressure gradients on the boattails, with the boattails having larger pressure gradients exhibiting larger interference effects.

To assess more fully the extent of the interference, all pressures for configurations 1, 2, and 3 were plotted in figure 42 as a function of peripheral location at two subsonic Mach numbers for both jet off and a jet-on pressure ratio of about 4. There were large effects on configurations 1 and 2 at jet-off conditions which fed almost all the way around the boattails whereas the jet-on data showed only relatively slight influence of the strut. Configuration 3, both jet off and jet on, showed almost no effect of the strut.

In references 1 and 4 it was reported that the data from the $\phi = 0^o$ row of orifices could be assumed to be interference free, and unpublished data from the present investigation which compared pressures on these boattails mounted on the sting-strut with a

solid cylinder to simulate the jet and on the same boattails mounted on a sting with the same cylinder support this belief. A comparison of the drag coefficients obtained by using the top row of orifices with that from all the rows is shown in figure 43 for two Mach numbers. Even though jet operation brought the two drag values closer together than the jet-off values (for configurations 1 and 2) there was still a noticeable difference. As with the pressures there was effectively no difference in the two methods for configuration 3. As a result, all longitudinal pressure distributions shown in previous figures have been from the top row of orifices and all pressure drag data were obtained from integration of the top row only. The only exception to this is in figure 36 which compares force and pressure data for which an integration based on all orifices is required.

REFERENCES

1. Compton, William B., III; and Runckel, Jack F.: Jet Effects on the Boattail Axial Force of Conical Afterbodies at Subsonic and Transonic Speeds. NASA TM X-1960, 1970.

2. Compton, William B., III: Jet Effects on the Drag of Conical Afterbodies at Supersonic Speeds. NASA TN D-6789, 1972.

3. Harrington, Douglas E.: Jet Effects on Boattail Pressure Drag of Isolated Ejector Nozzles at Mach Numbers From 0.60 to 1.47. NASA TM X-1785, 1969.

4. Reubush, David E.: Effects of Fineness and Closure Ratios on Boattail Drag of Circular-Arc Afterbody Models With Jet Exhaust at Mach Numbers up to 1.30. NASA TN D-7163, 1973.

5. Swihart, John M.; Mercer, Charles E.; and Norton, Harry T., Jr.: Effect of Afterbody-Ejector Configurations on the Performance at Transonic Speeds of a Pylon-Supported Nacelle Model Having a Hot-Jet Exhaust. NASA TN D-1399, 1962. (Supersedes NASA MEMO 1-4-59L.)

6. Shrewsbury, George D.: Effect of Boattail Juncture Shape on Pressure Drag Coefficients of Isolated Afterbodies. NASA TM X-1517, 1968.

7. Ward, Vernon G.; Whitcomb, Charles F.; and Pearson, Merwin D.: Air-Flow and Power Characteristics of the Langley 16-Foot Transonic Tunnel With Slotted Test Section. NACA RM L52E01, 1952.

8. Schaefer, William T., Jr.: Characteristics of Major Active Wind Tunnels at the Langley Research Center. NASA TM X-1130, 1965.

9. Anon.: Flow Measurement by Means of Thin Plate Orifices, Flow Nozzles and Venturi Tubes. Supplement on Instruments and Apparatus, pt. 5, ch. 4, Power Test Codes, ASME, 1959, pp. 5-91.

10. Braslow, Albert L.; and Knox, Eugene C.: Simplified Method for Determination of Critical Height of Distributed Roughness Particles for Boundary-Layer Transition at Mach Numbers From 0 to 5. NACA TN 4363, 1958.

11. Braslow, Albert L.; Hicks, Raymond M.; and Harris, Roy V., Jr.: Use of Grit-Type Boundary-Layer-Transition Trips on Wind-Tunnel Models. NASA TN D-3579, 1966.

12. Cubbage, James M., Jr.: Jet Effects on the Drag of Conical Afterbodies for Mach Numbers of 0.6 to 1.28. NACA RM L57B21, 1957.

13. Bergman, Dave: Effects of Engine Exhaust Flow on Boattail Drag. AIAA Paper No. 70-132, Jan. 1970.

14. Hess, J. L.; and Smith, A. M. O.: Calculation of Potential Flow About Arbitrary Bodies. Progress in Aeronautical Sciences, Vol. 8, D. Kuchemann, ed., Pergamon Press Ltd., c.1967, pp. 1-138.

15. Holdhusen, James S.; and Lamb, Owen P.: Scale Model Studies of Exhaust Nozzle Performance. AIAA Paper No. 66-641, June 1966.

16. Thornock, Russel L.: Experimental Investigation of the Flow Through Convergent Conical Nozzles. Doc. No. D6-20375, Boeing Co., Sept. 26, 1968. (Available from DDC as AD 841 418.)

17. Thornock, R. L.; and Brown, E. F.: An Experimental Study of Compressible Flow Through Convergent-Conical Nozzles, Including a Comparison With Theoretical Results. Paper No. 71-WA/FE-3, Amer. Soc. Mech. Eng., 1971.

TABLE I.- AFTERBODY-SURFACE ORIFICE LOCATIONS

Configuration 1		Configuration 2		Configuration 3		ϕ, deg								
x/l	x/d_m	x/l	x/d_m	x/l	x/d_m	0	30	60	90	120	150	180	225	315
0	0	0	0	0	0	X		X	X		X	X	X	X
.217	.173	.213	.213	.209	.370	X	X		X	X		X		
.378	.302	.372	.372	.366	.647	X		X	X		X	X		
.491	.393	.485	.485	.478	.845	X	X	X	X	X	X	X	X	X
.586	.469	.580	.580	.572	1.012	X	X	X	X	X	X	X		
.671	.537	.665	.665	.657	1.162	X	X	X	X	X	X	X		
.750	.600	.744	.744	.737	1.303	X	X	X	X	X	X	X	X	X
.825	.660	.820	.820	.815	1.440	X	X	X	X	X	X	X		
.898	.719	.895	.895	.891	1.576	X	X	X	X	X	X	X		
.972	.777	.971	.971	.969	1.714	X	X	X	X	X	X	X	X	X

STA configuration		ϕ, deg								
x/l	x/d_m	0	30	60	90	120	150	180	225	315
0	0	X			X			X		
.15	.19	X			X			X		
.29	.38	X			X			X		
.44	.56	X			X			X		
.58	.75	X			X			X		
.72	.93	X			X			X		
.86	1.11	X			X			X		
.93	1.19	X			X			X		
.99	1.27	X			X			X		

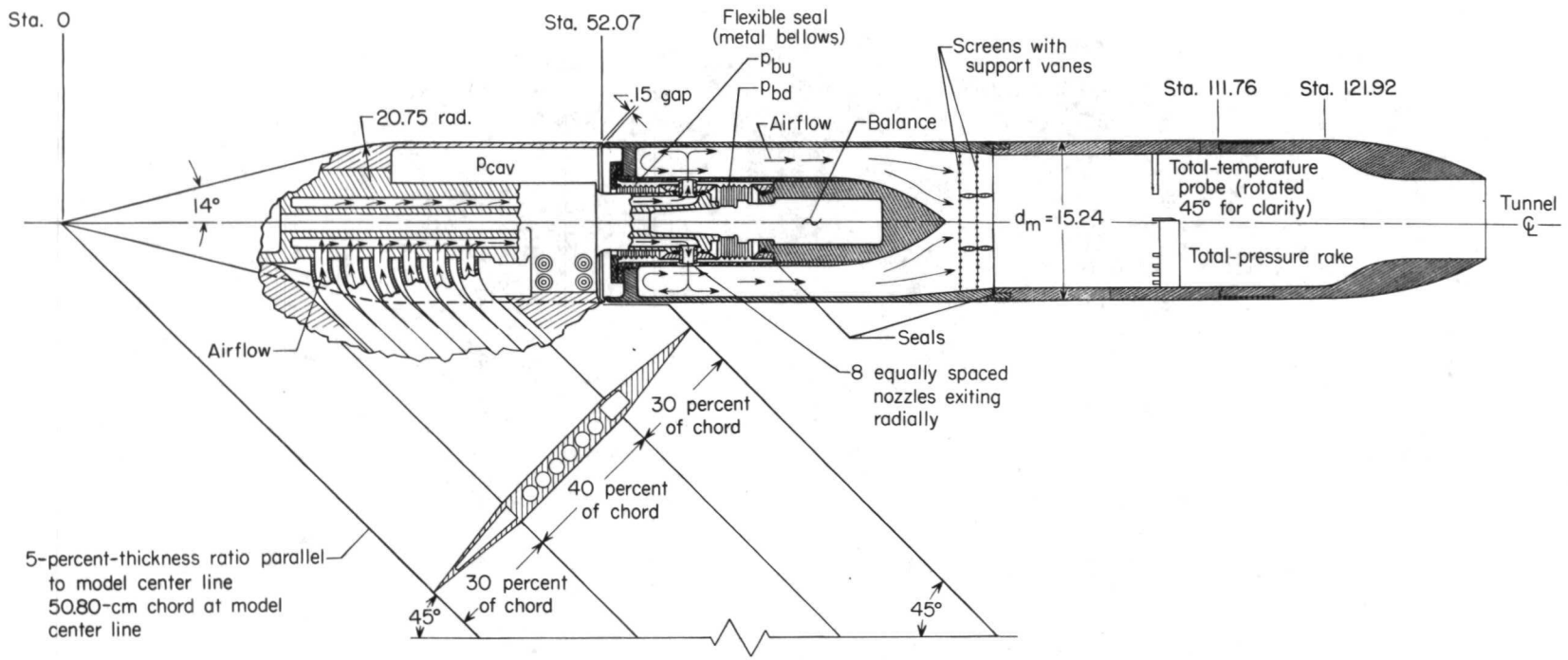

Figure 1.- Sketch of air-powered cone-cylinder model with a typical circular-arc convergent nozzle installed. All dimensions are in centimeters unless otherwise noted.

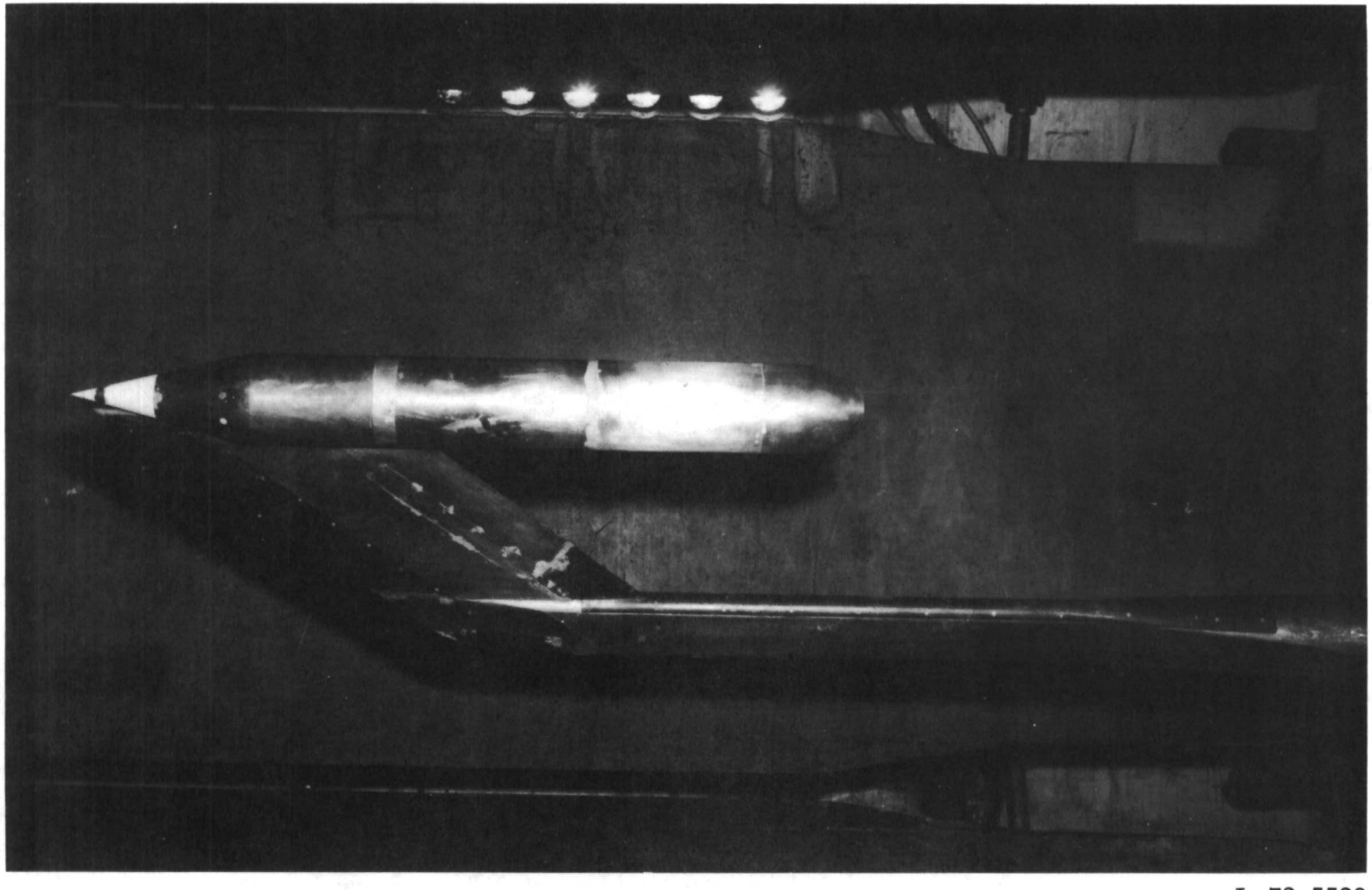

L-72-5523

Figure 2.- Nacelle model installed in Langley 16-foot transonic tunnel with configuration 1 attached.

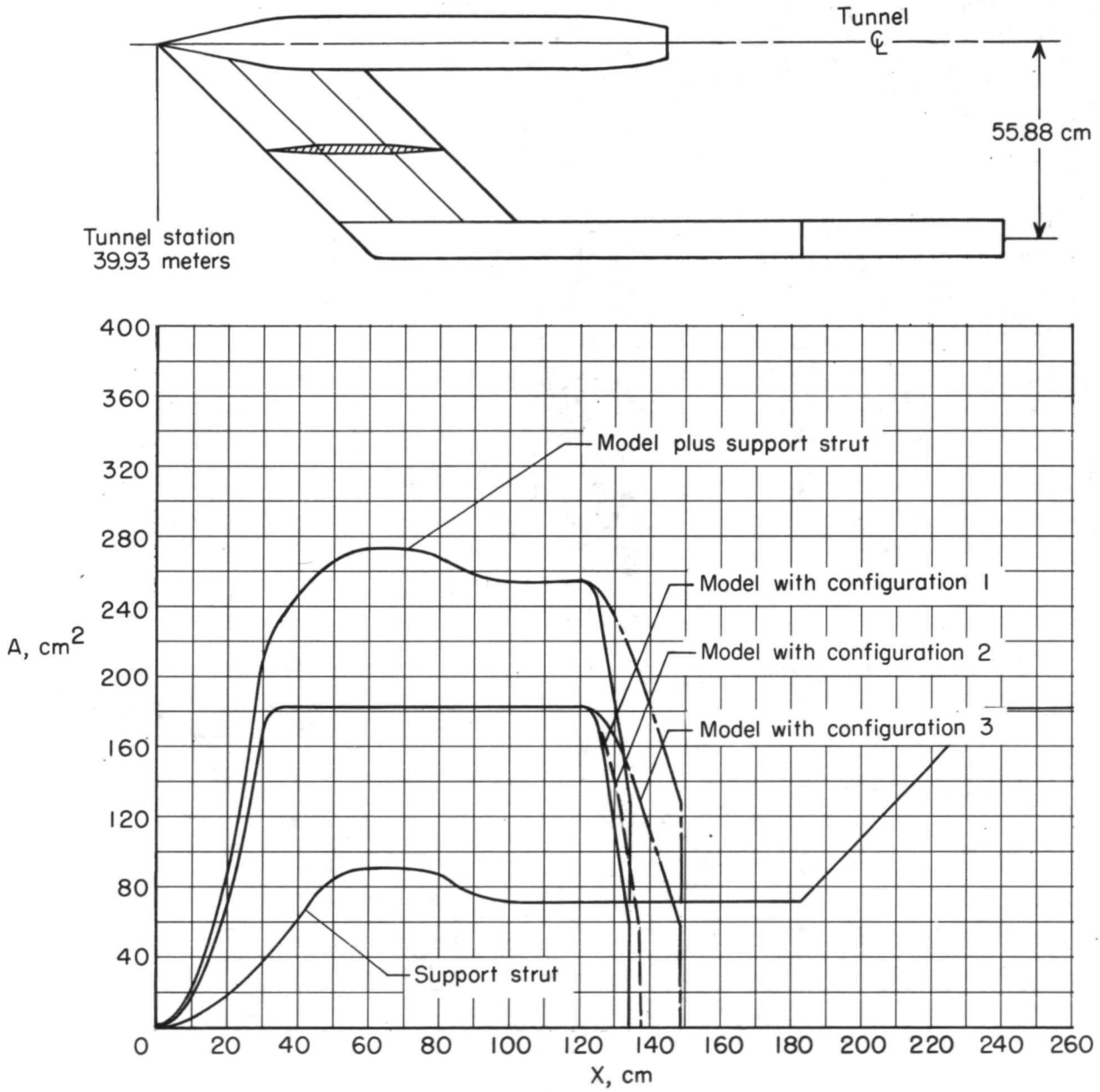

Figure 3.- Cross-sectional area distributions of support system and model.

L-70-1354

Figure 4.- Nacelle model with STA configuration attached.

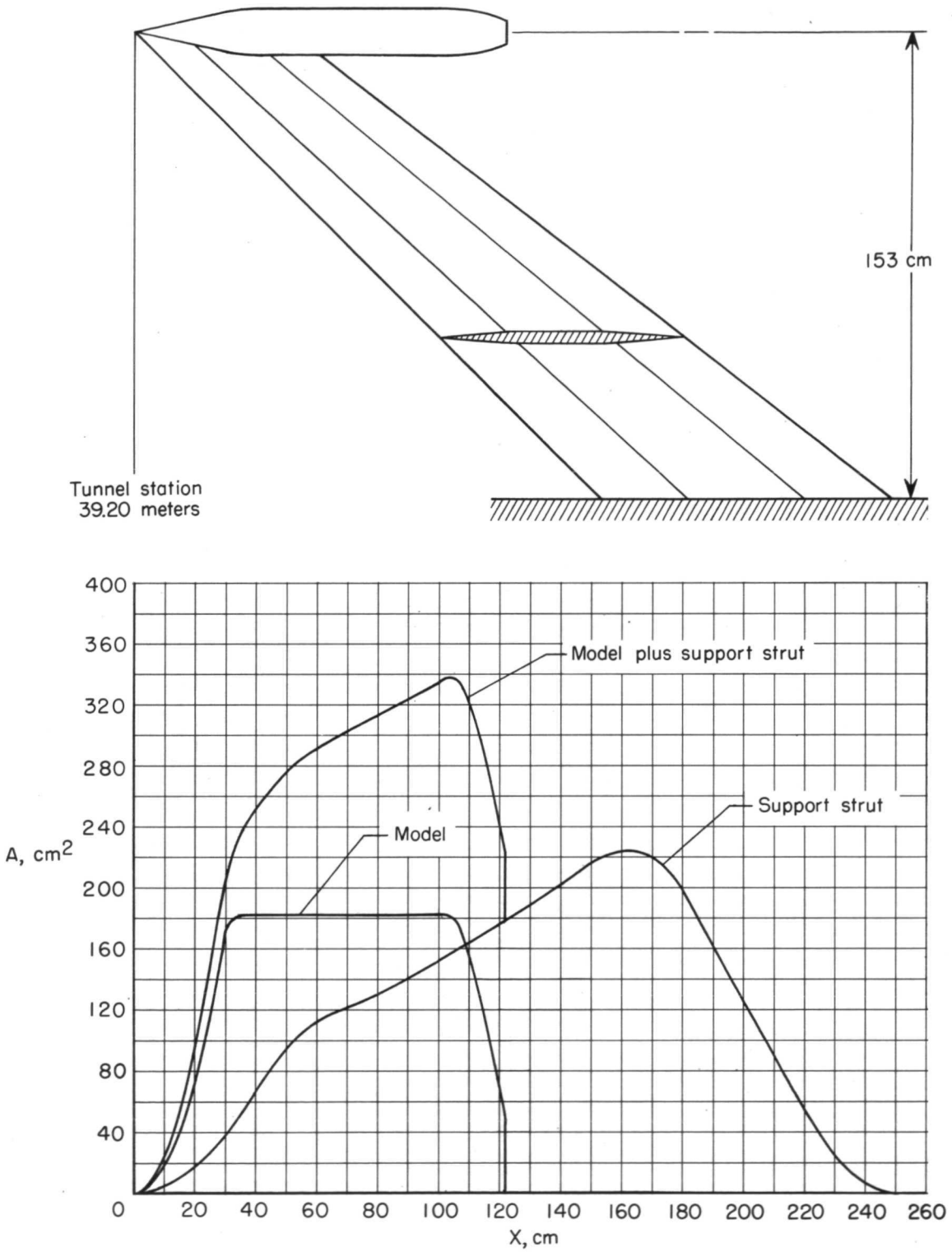

Figure 5.- Cross-sectional area distributions for model and support strut used with STA configuration.

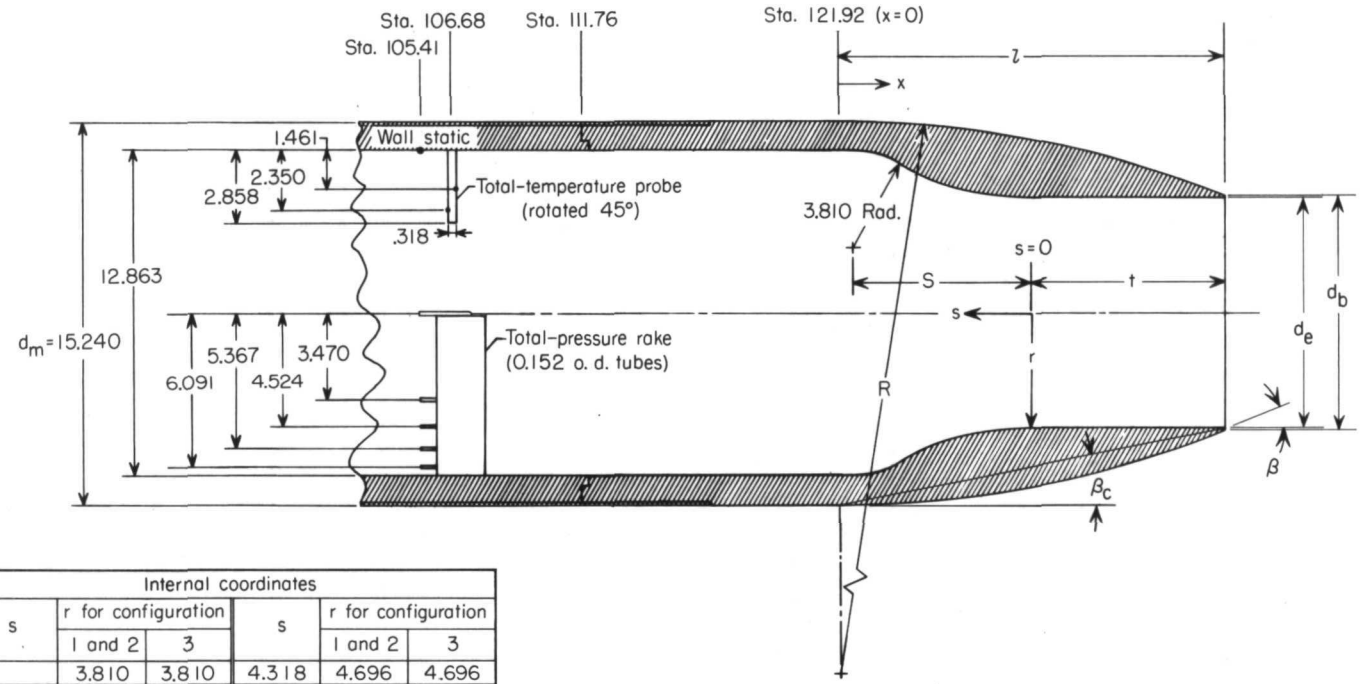

Internal coordinates					
s	r for configuration		s	r for configuration	
	1 and 2	3		1 and 2	3
0	3.810	3.810	4.318	4.696	4.696
.254	3.813	3.813	4.445	4.755	4.755
.508	3.820	3.820	4.572	4.816	4.816
.762	3.835	3.835	4.699	4.882	4.882
1.016	3.856	3.856	4.826	4.948	4.948
1.270	3.881	3.881	4.953	5.019	5.019
1.524	3.912	3.912	5.080	5.090	5.090
1.778	3.950	3.950	5.207	5.169	5.169
2.032	3.993	3.993	5.334	5.248	5.248
2.286	4.041	4.041	5.461	5.334	5.334
2.540	4.097	4.097	5.588	5.420	5.420
2.794	4.161	4.161	5.715	5.514	5.514
3.048	4.229	4.229	5.842	5.611	5.611
3.302	4.308	4.308	5.969	5.715	5.715
3.556	4.392	4.392	6.096	5.822	5.822
3.810	4.483	4.483	6.223	5.939	——
3.937	4.534	4.534	6.350	6.060	——
4.064	4.585	4.585	6.477	6.190	——
4.191	4.641	4.641			

Geometric parameters								
Configuration	l/d_m	d_e/d_m	d_b/d_m	R/d_m	t/d_m	S/d_m	β, deg	$β_c$, deg
1	0.800	0.50	0.51	1.429	0.50	0.533	34.037	17.018
2	1.000	.50	.51	2.163	.50	.533	27.518	13.759
3	1.768	.50	.51	6.500	.50	.458	15.773	7.886

Figure 6.- Detailed sketch of typical configuration with tables of geometric parameters and internal coordinates. All dimensions are in centimeters unless otherwise noted.

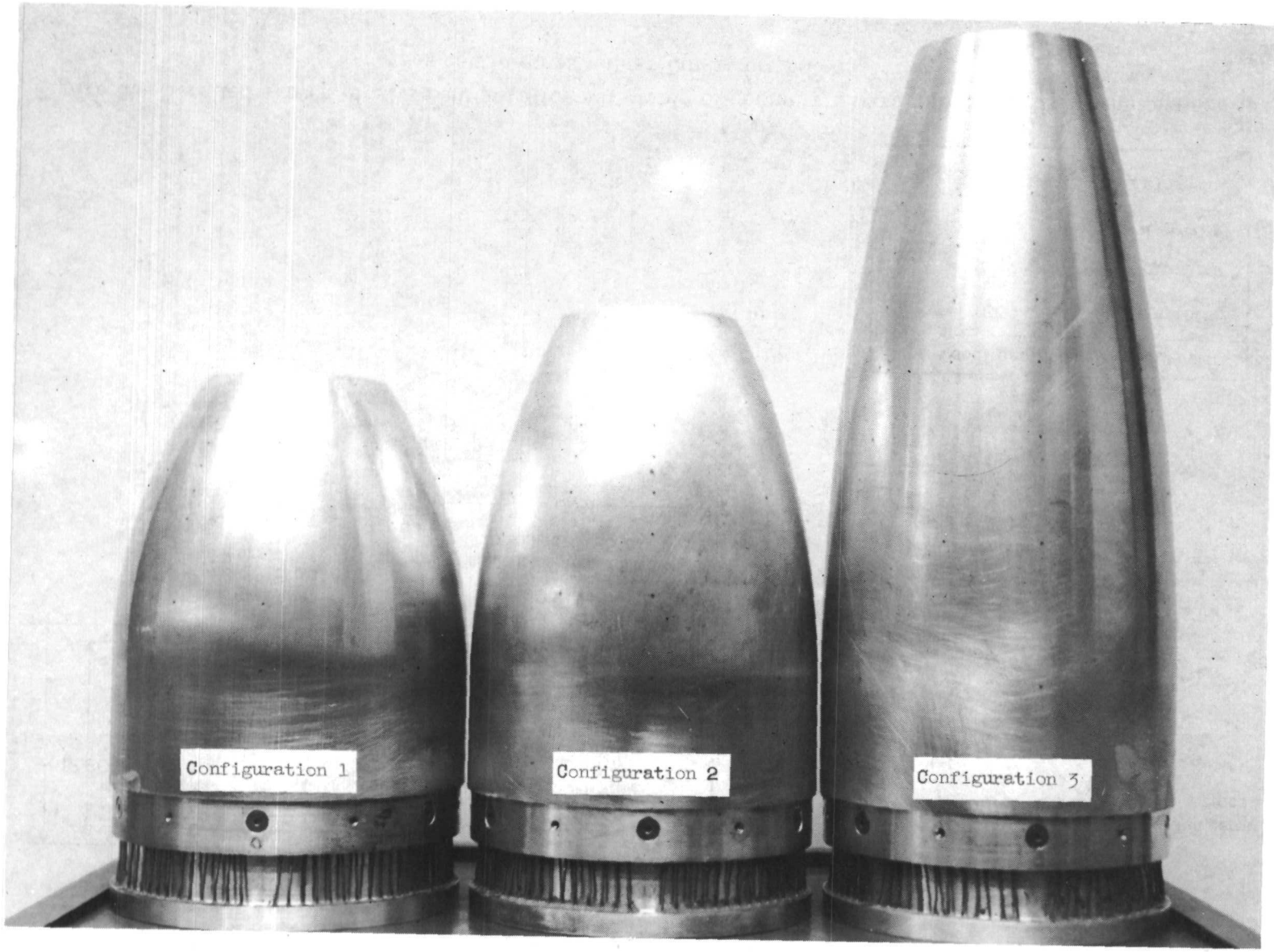

L-72-5522

Figure 7.- Afterbody models.

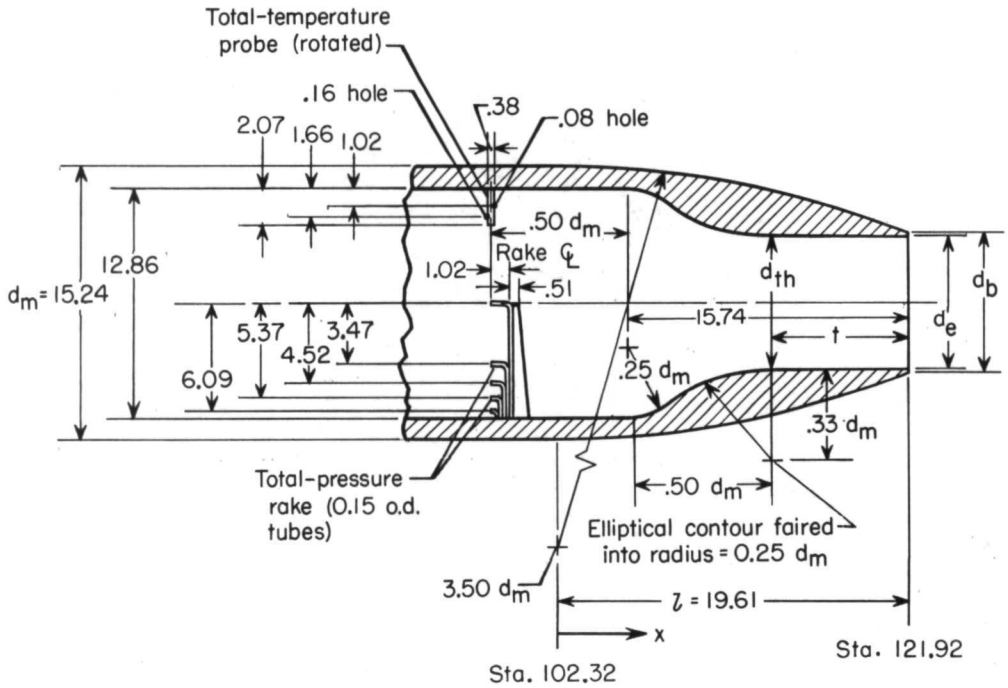

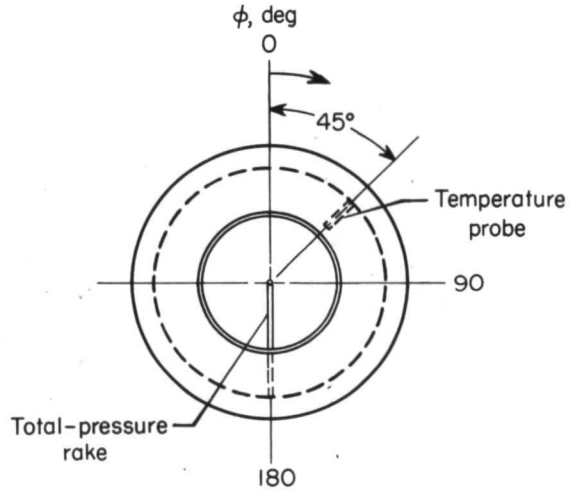

Base pressures located at $\phi = 315°$, 0.22 and 3.81 cm from exit

Dimensional and geometric parameters	
$\ell/d_m = 1.286$	$t/d_m = 0.50$
$d_e/d_m = 0.50$	$d_{th}/d_m = 0.50$
$d_b/d_m = 0.51$	$\beta = 21.561°$
$R/d_m = 3.50$	$\beta_c = 10.781°$

Figure 8.- Detailed sketch of STA configuration with table of geometric parameters. All dimensions are in centimeters unless otherwise noted.

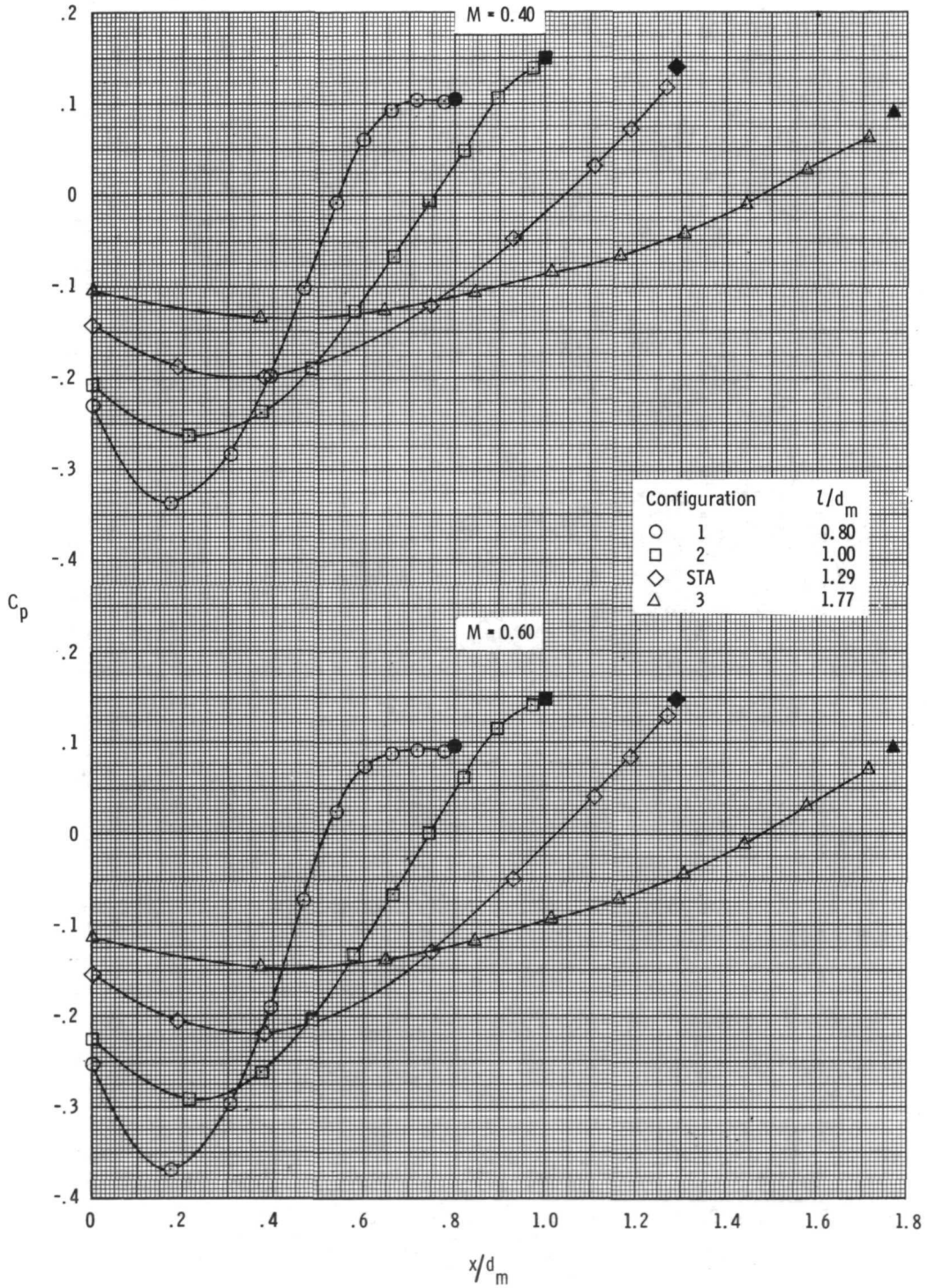

(a) M = 0.40 and 0.60.

Figure 9.- Jet-off boattail pressure coefficient distributions for all configurations. Tick marks indicate critical pressure coefficients. Solid symbols indicate base pressure coefficients.

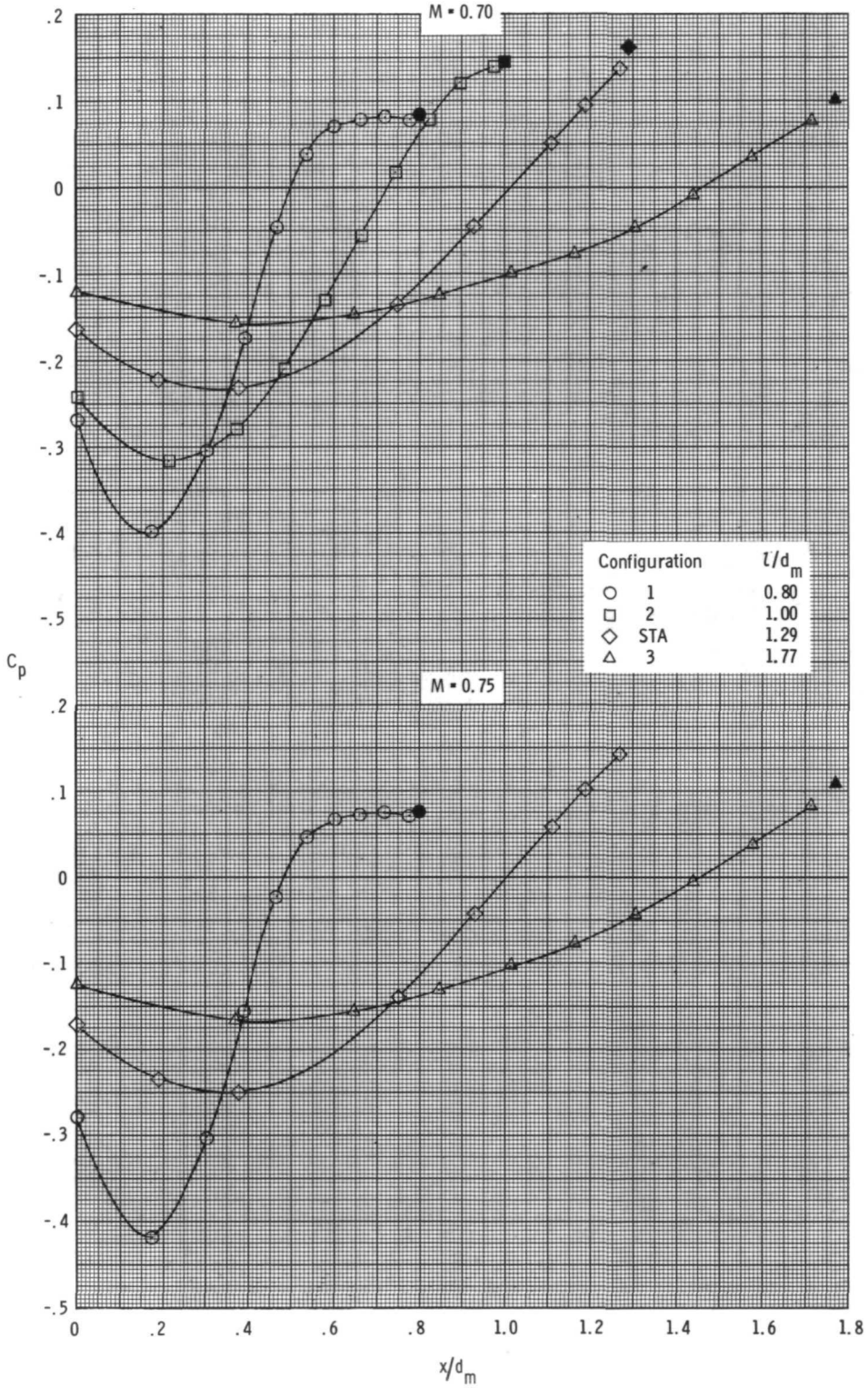

(b) M = 0.70 and 0.75.

Figure 9.- Continued.

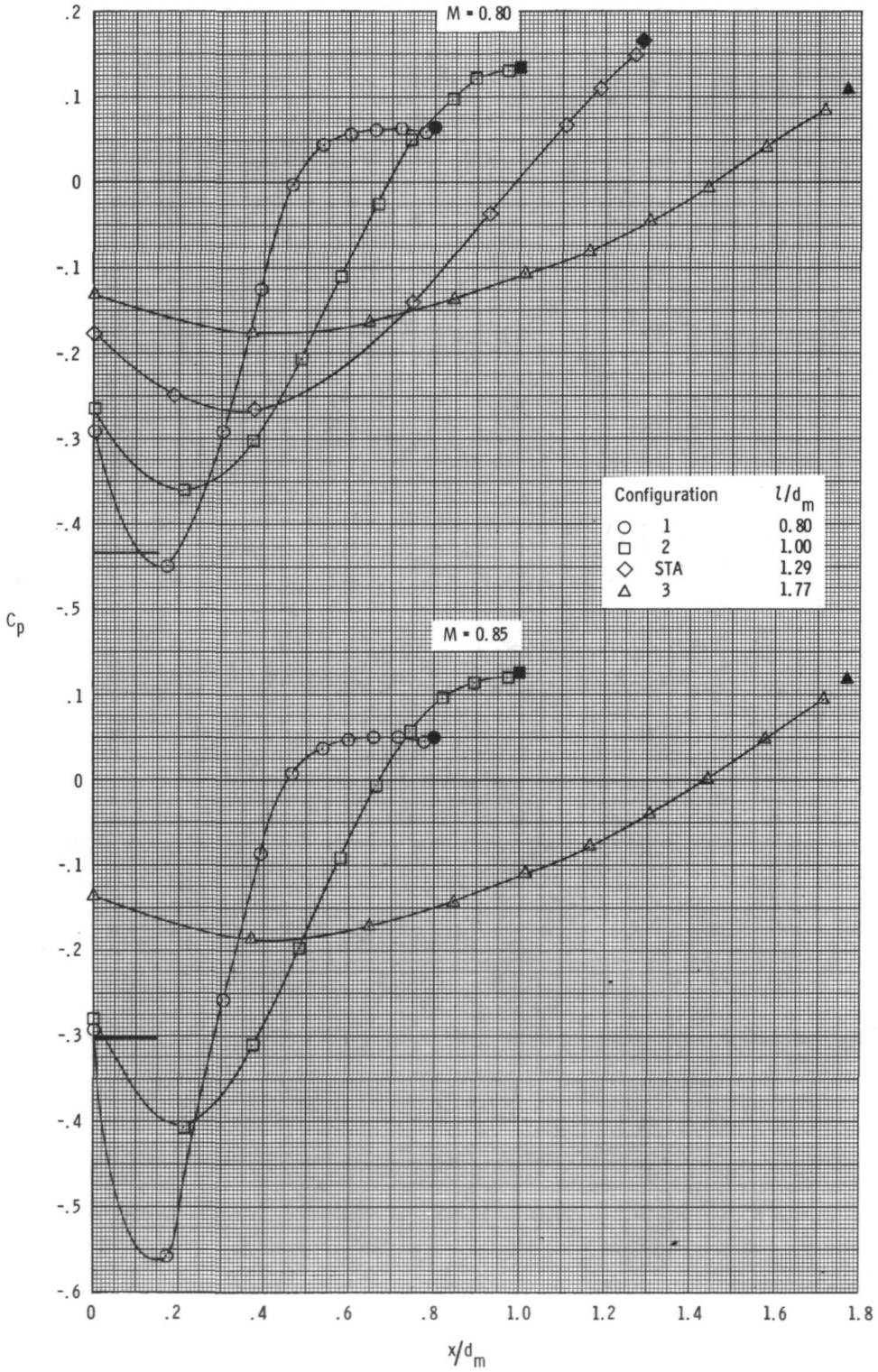

(c) M = 0.80 and 0.85.

Figure 9.- Continued.

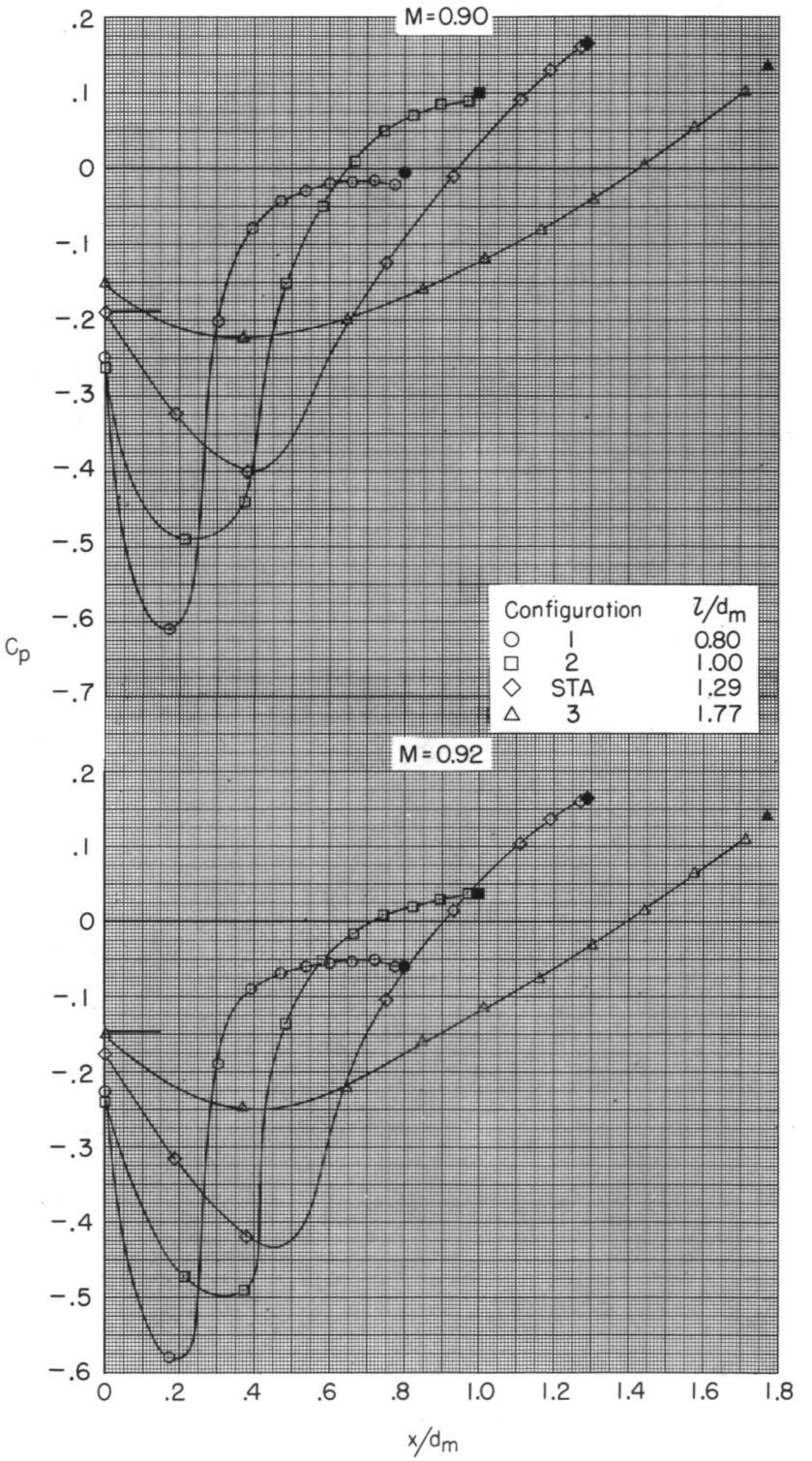

(d) M = 0.90 and 0.92.

Figure 9.- Continued.

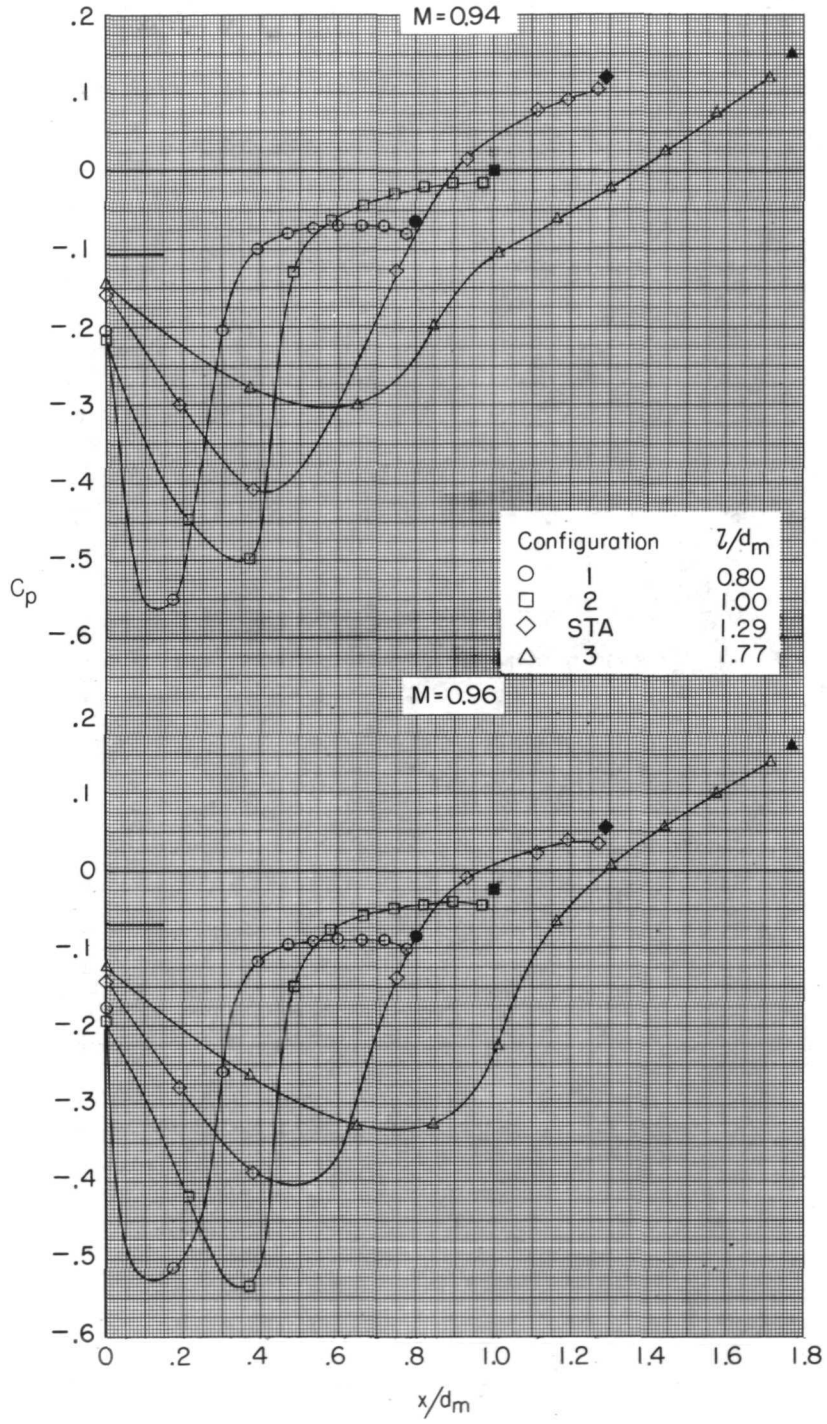

(e) M = 0.94 and 0.96.

Figure 9.- Continued.

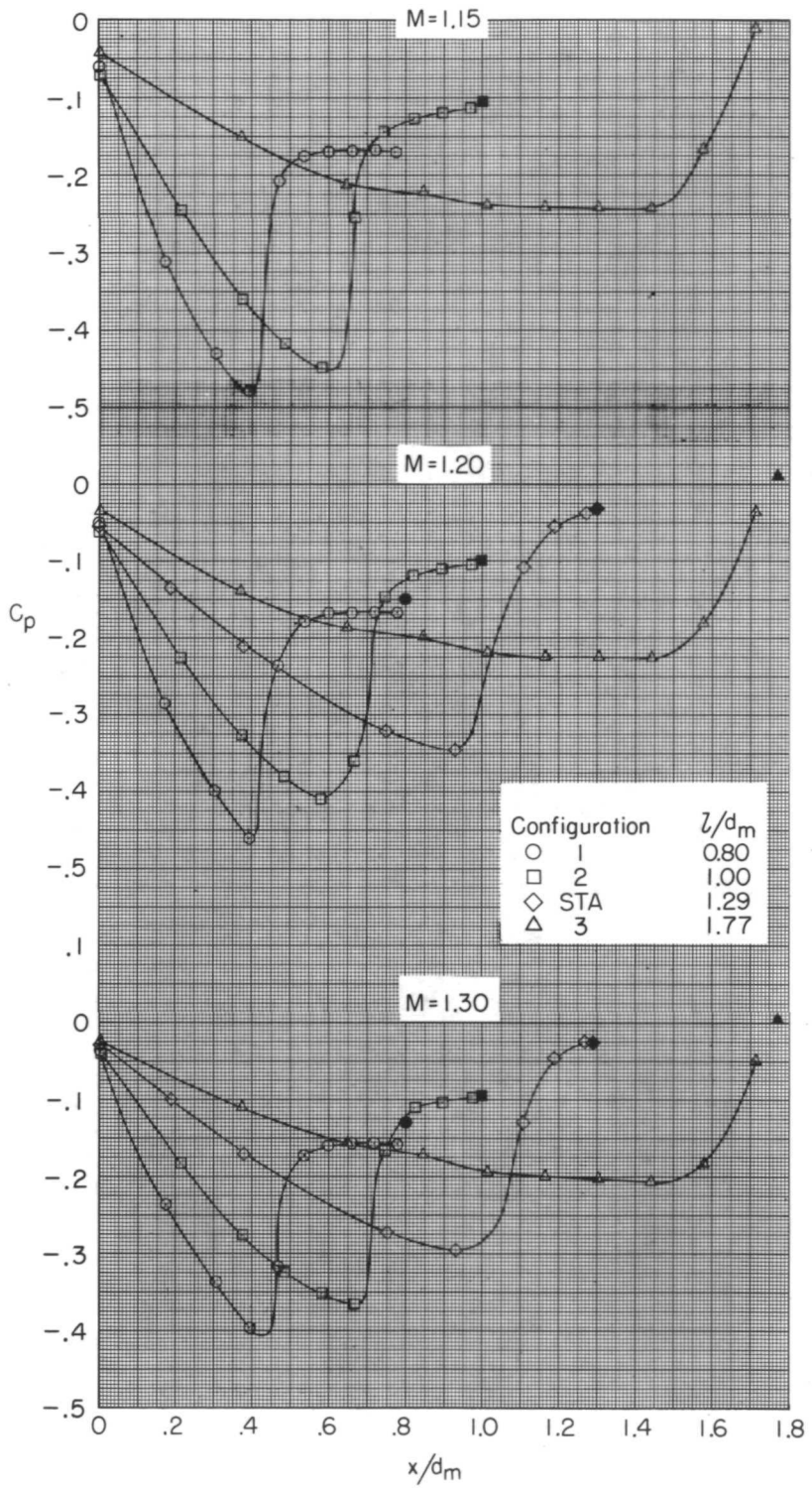

(f) M = 1.15, 1.20, and 1.30.

Figure 9.- Concluded.

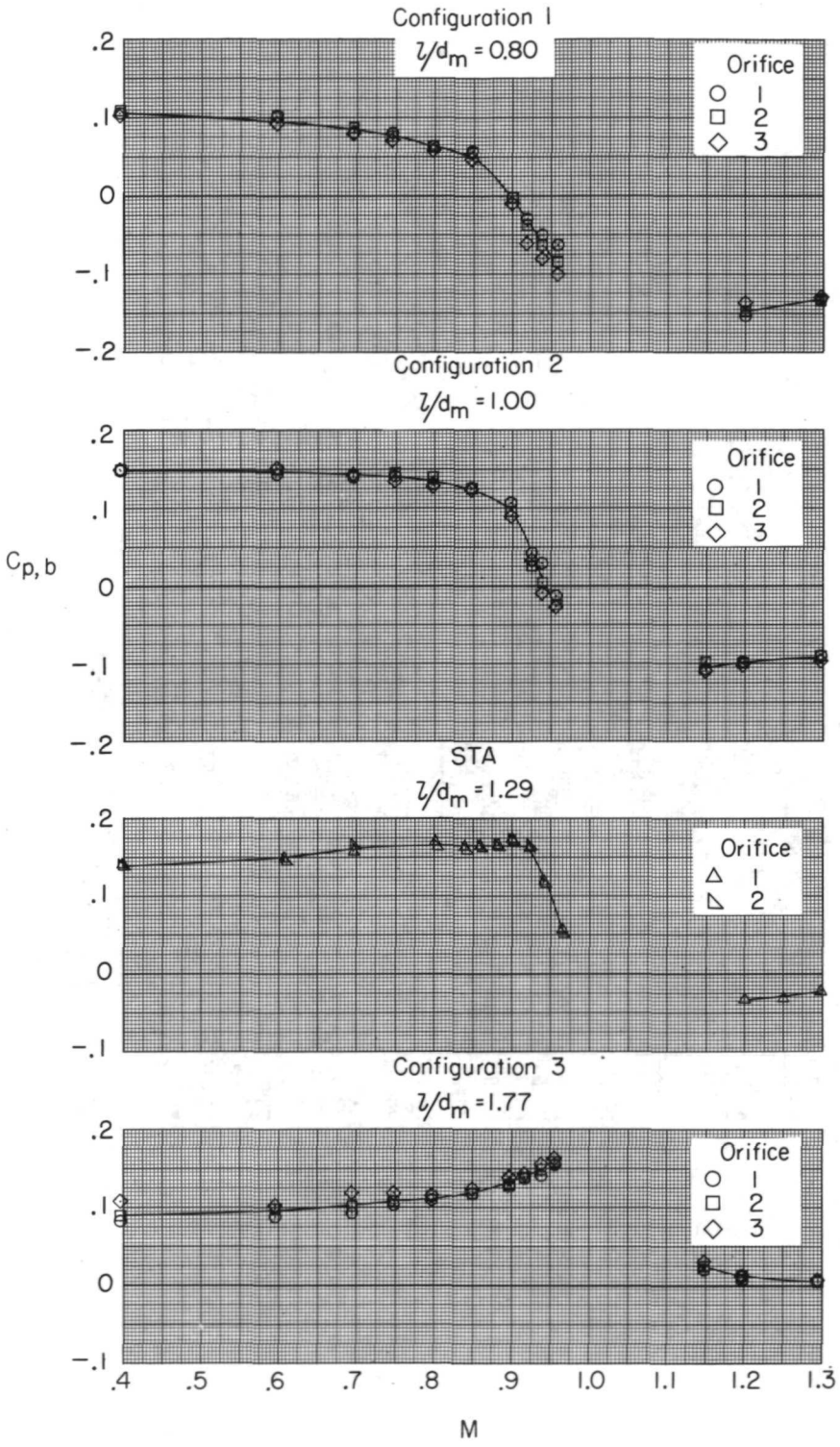

Figure 10.- Variation of jet-off base pressure coefficients with Mach number for all configurations.

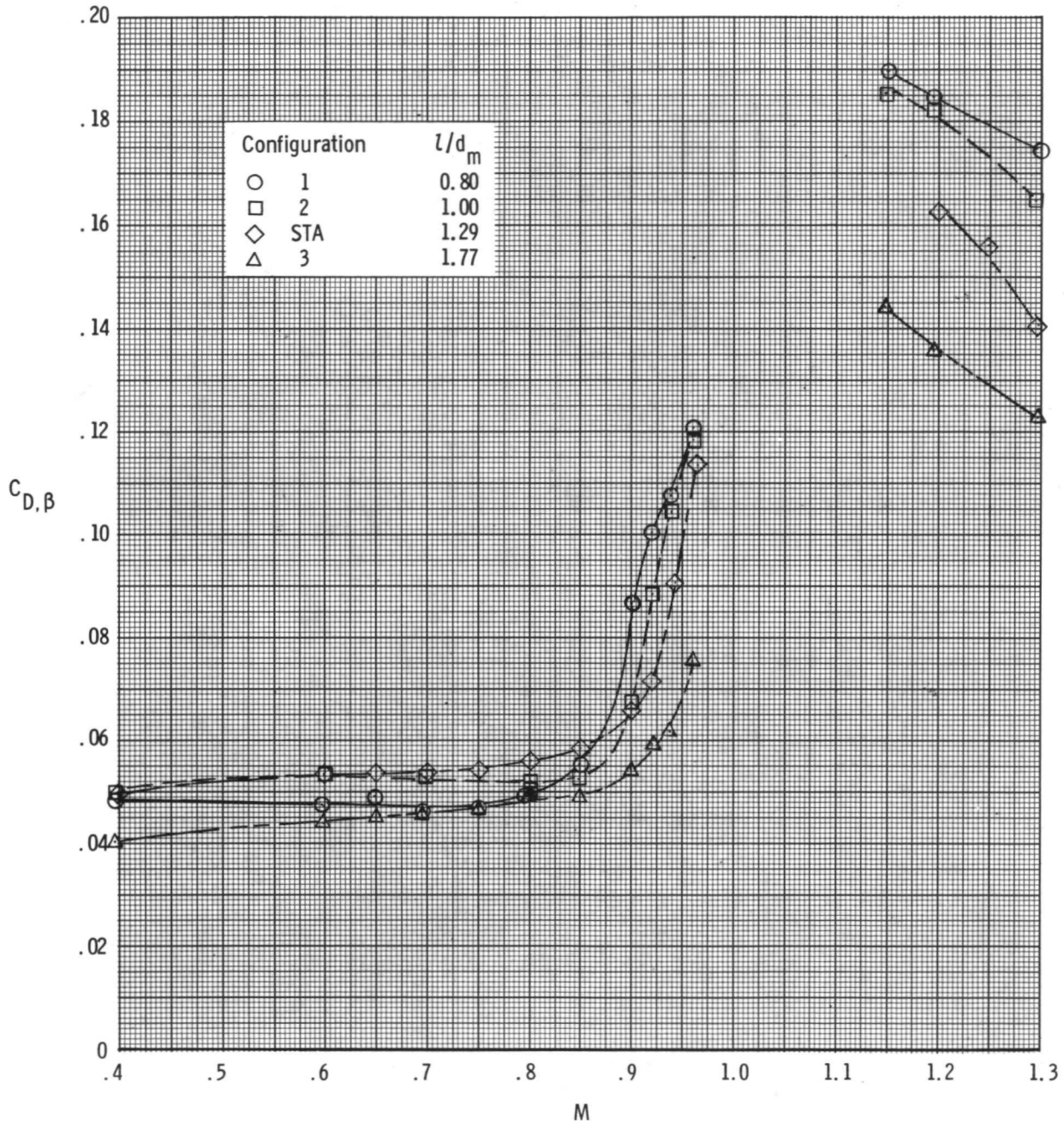

Figure 11.- Variation of jet-off boattail pressure drag with Mach number for all configurations.

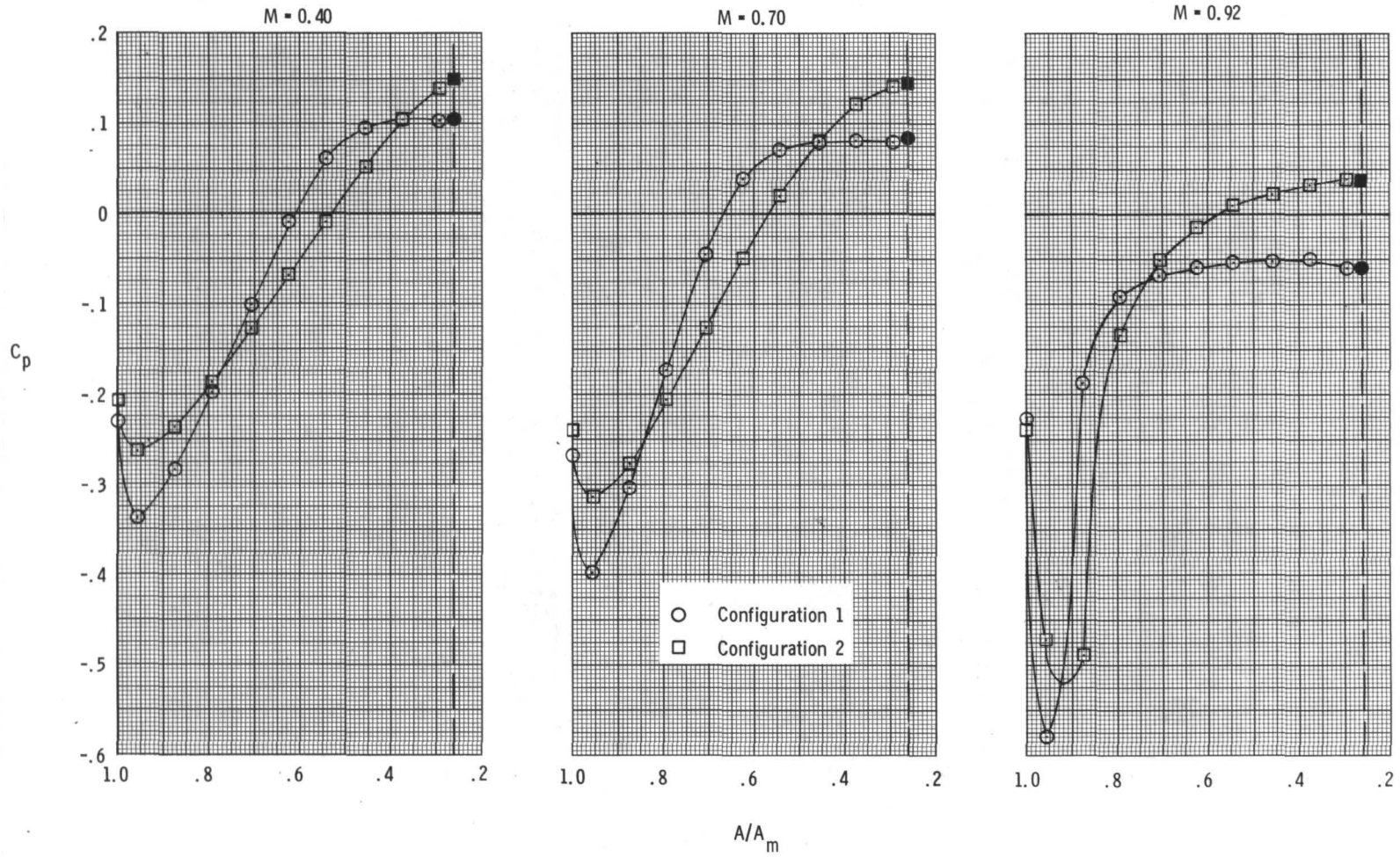

Figure 12.- Jet-off boattail pressure coefficient distributions as a function of area ratio for configurations 1 and 2 $\left(l/d_m = 0.80 \text{ and } 1.00\right)$ at three Mach numbers. Dash line indicates end of boattail. Solid symbols indicate base pressure coefficients.

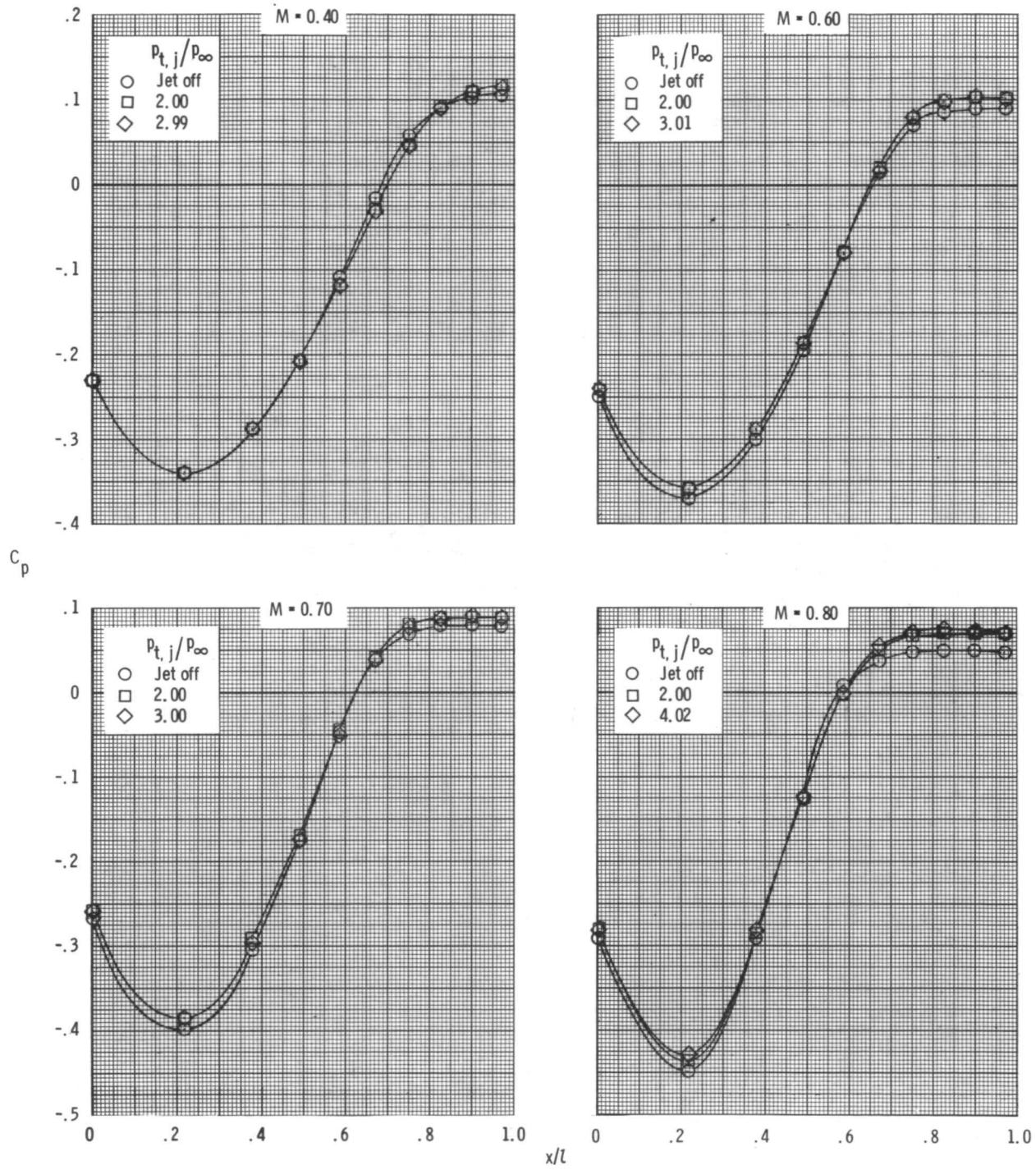

(a) M = 0.40, 0.60, 0.70, and 0.80.

Figure 13.- Boattail pressure distributions on configuration 1 $\left(l/d_m = 0.80\right)$ at various Mach numbers and three values of jet total-pressure ratio.

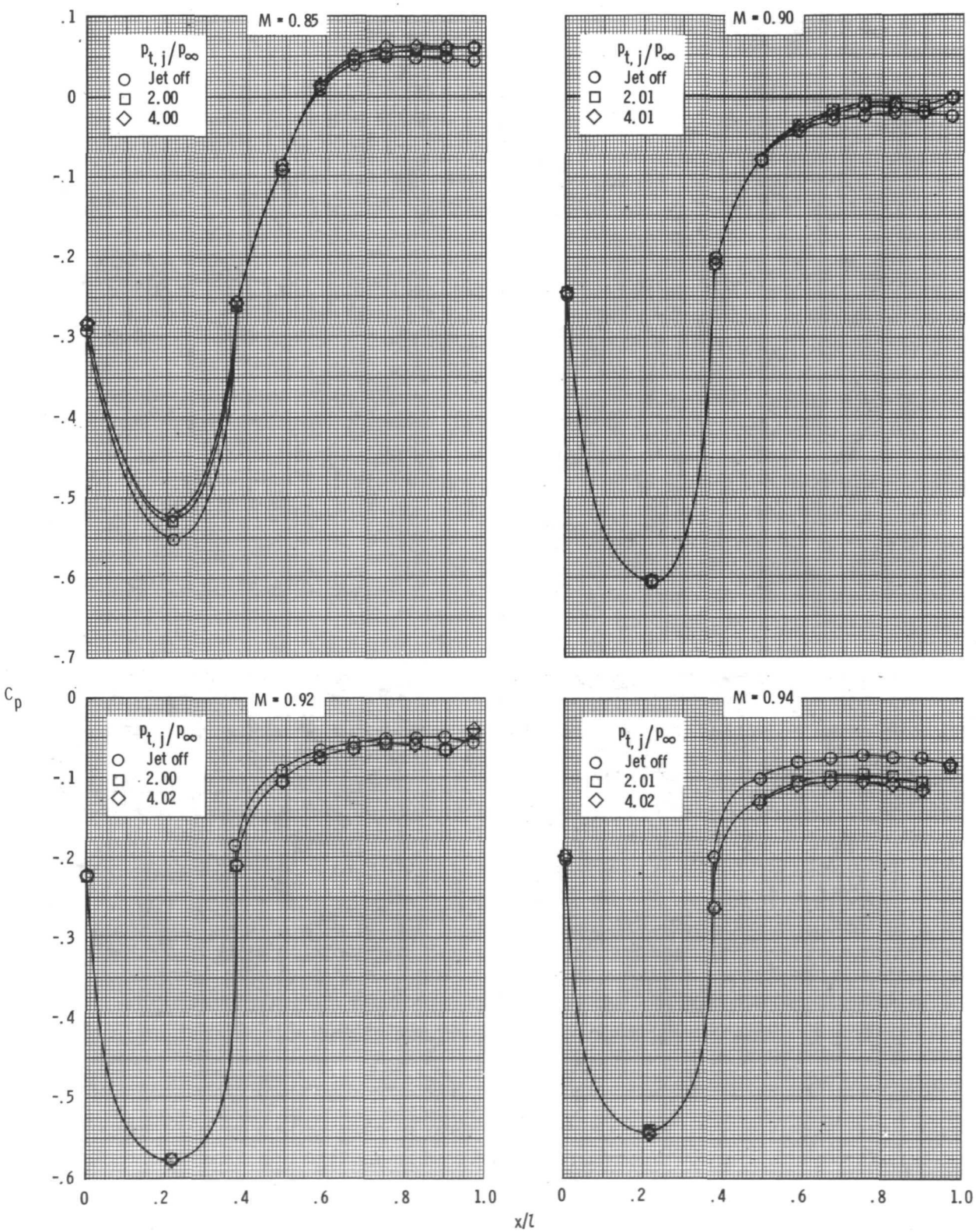

(b) M = 0.85, 0.90, 0.92, and 0.94.

Figure 13.- Continued.

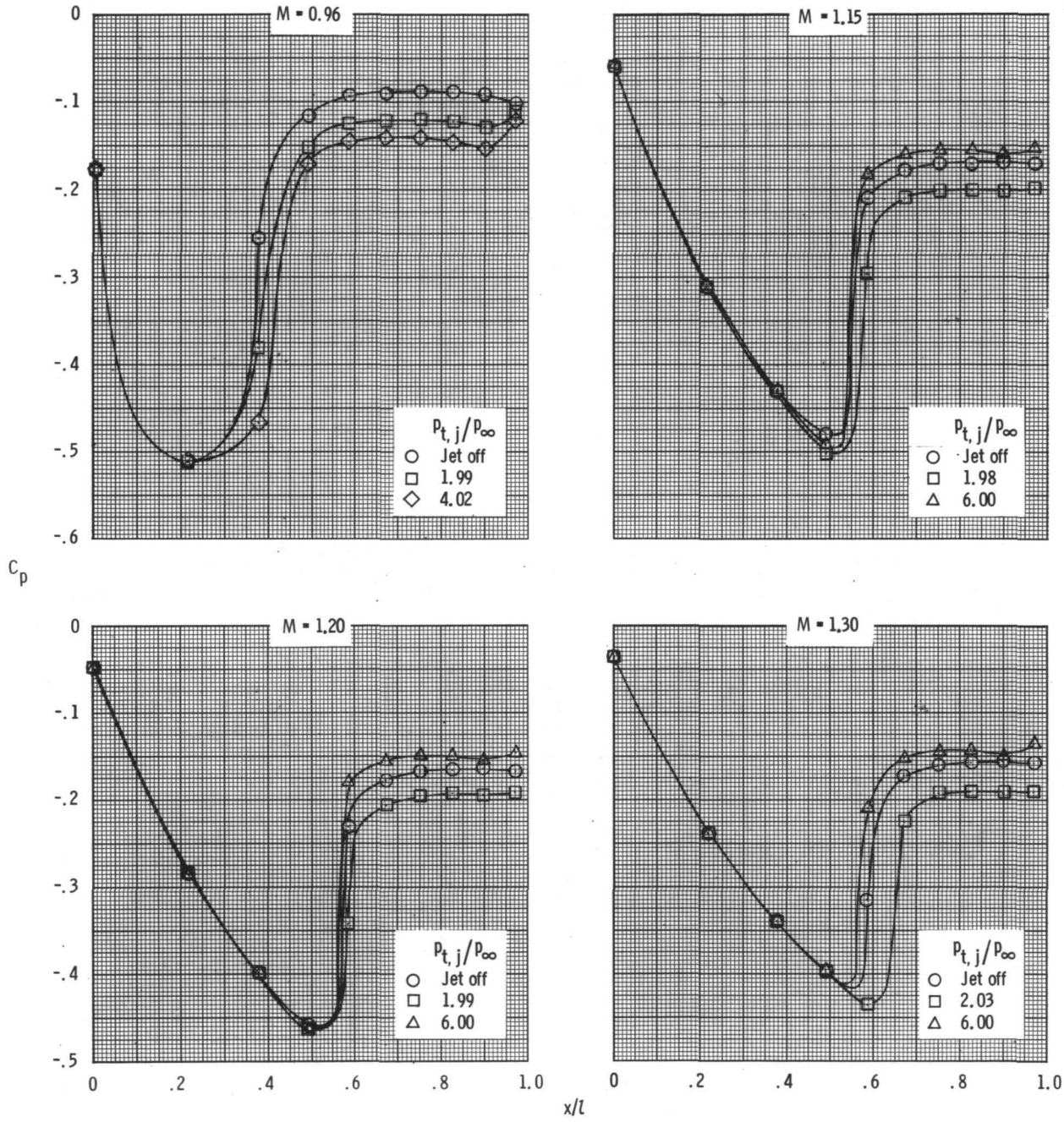

(c) M = 0.96, 1.15, 1.20, and 1.30.

Figure 13.- Concluded.

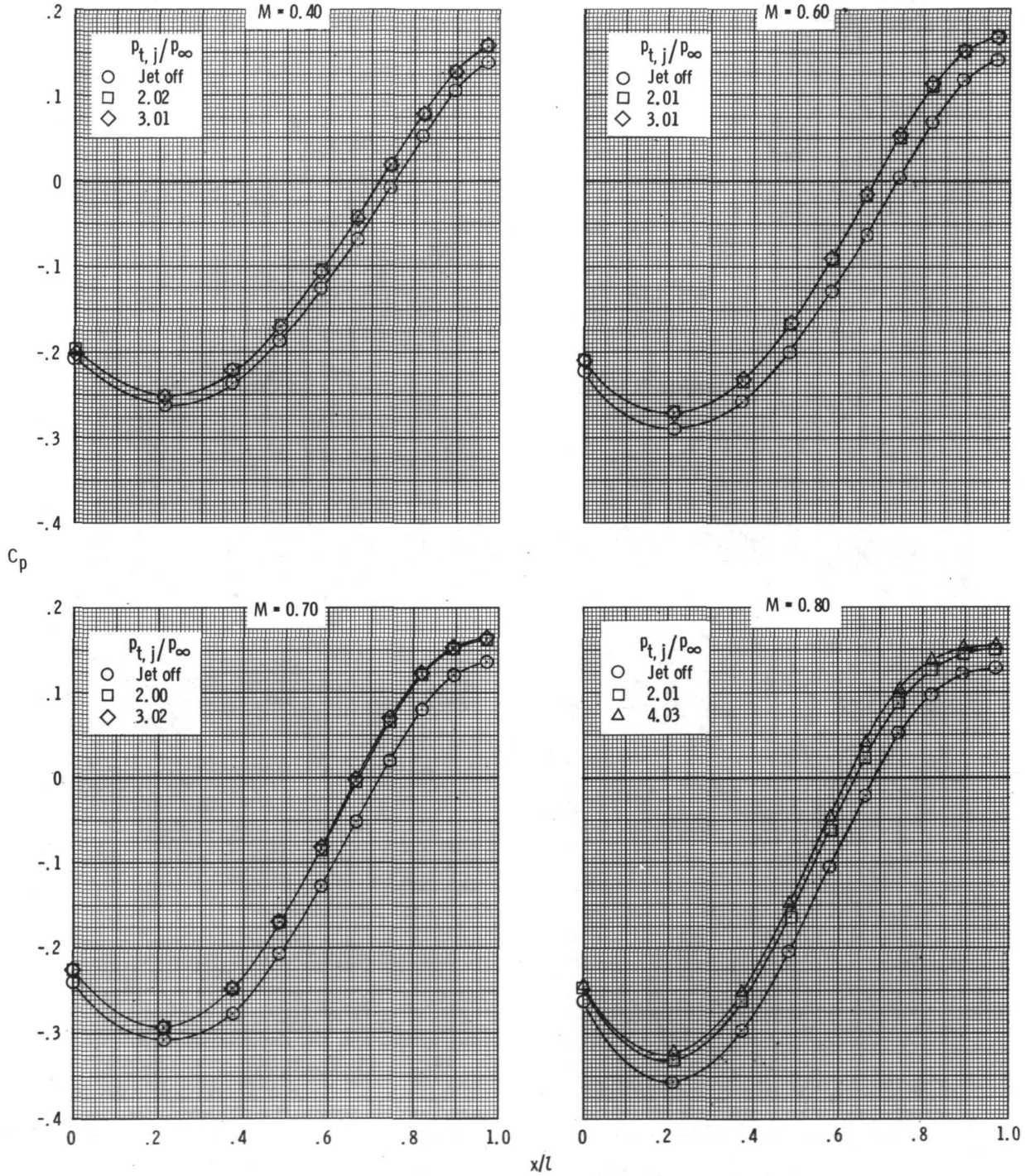

(a) M = 0.40, 0.60, 0.70, and 0.80.

Figure 14.- Boattail pressure distributions on configuration 2 $\left(l/d_m = 1.00\right)$ at various Mach numbers and three values of jet total-pressure ratio.

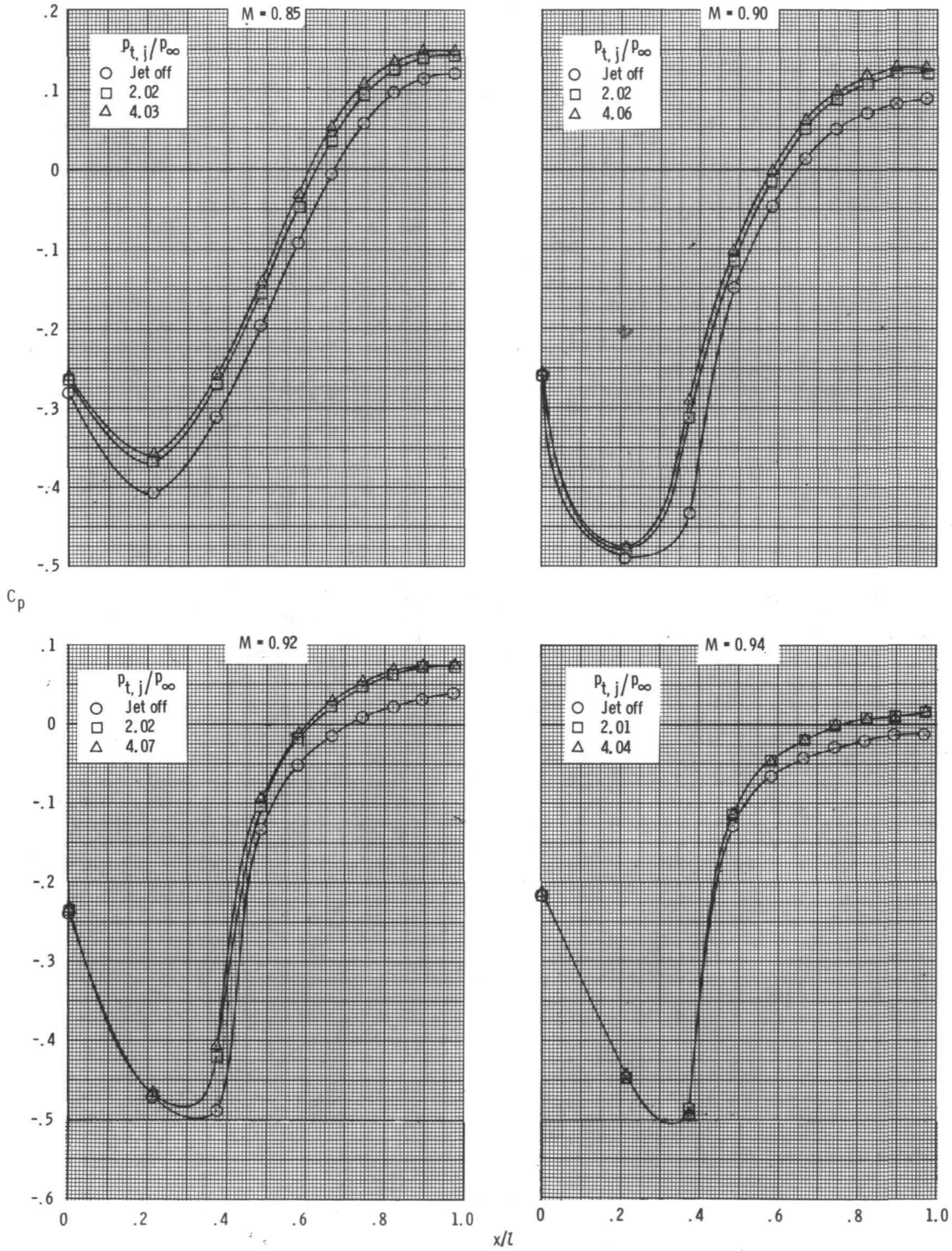

(b) M = 0.85, 0.90, 0.92, and 0.94.

Figure 14.- Continued.

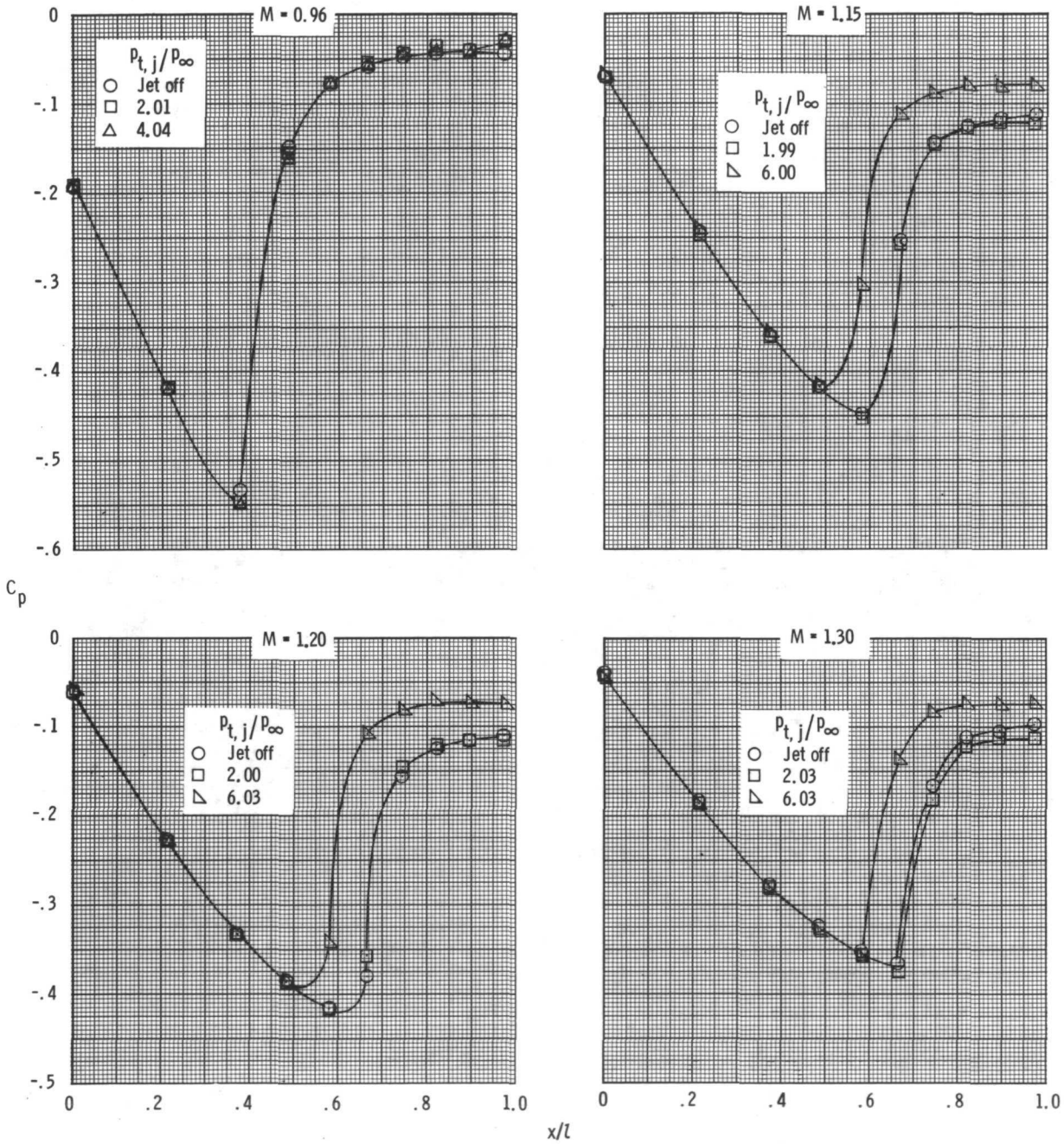

(c) M = 0.96, 1.15, 1.20, and 1.30.

Figure 14.- Concluded.

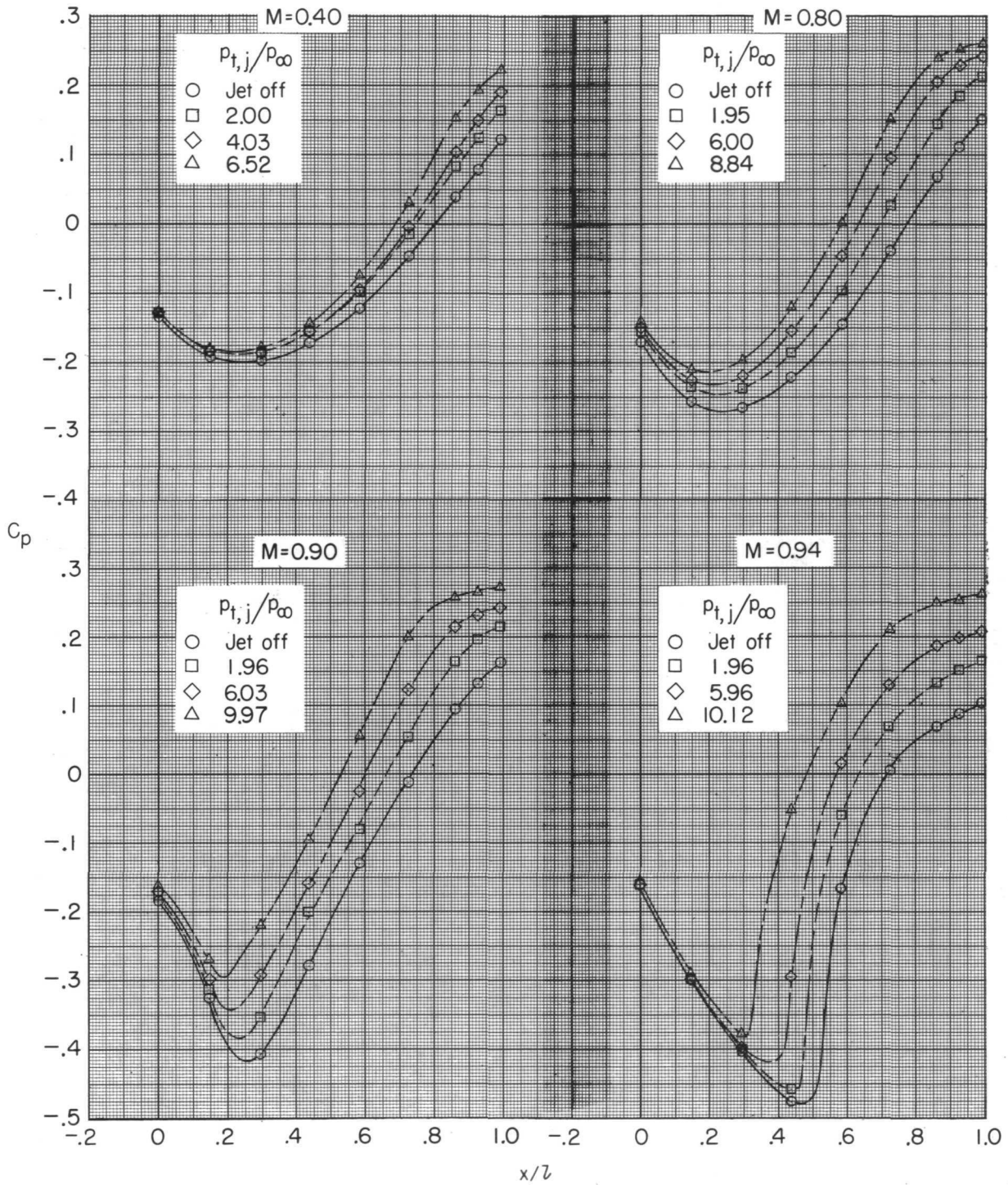

(a) M = 0.40, 0.80, 0.90, and 0.94.

Figure 15.- Boattail pressure distributions on STA configuration $(l/d_m = 1.29)$ at various Mach numbers and four values of jet total-pressure ratio.

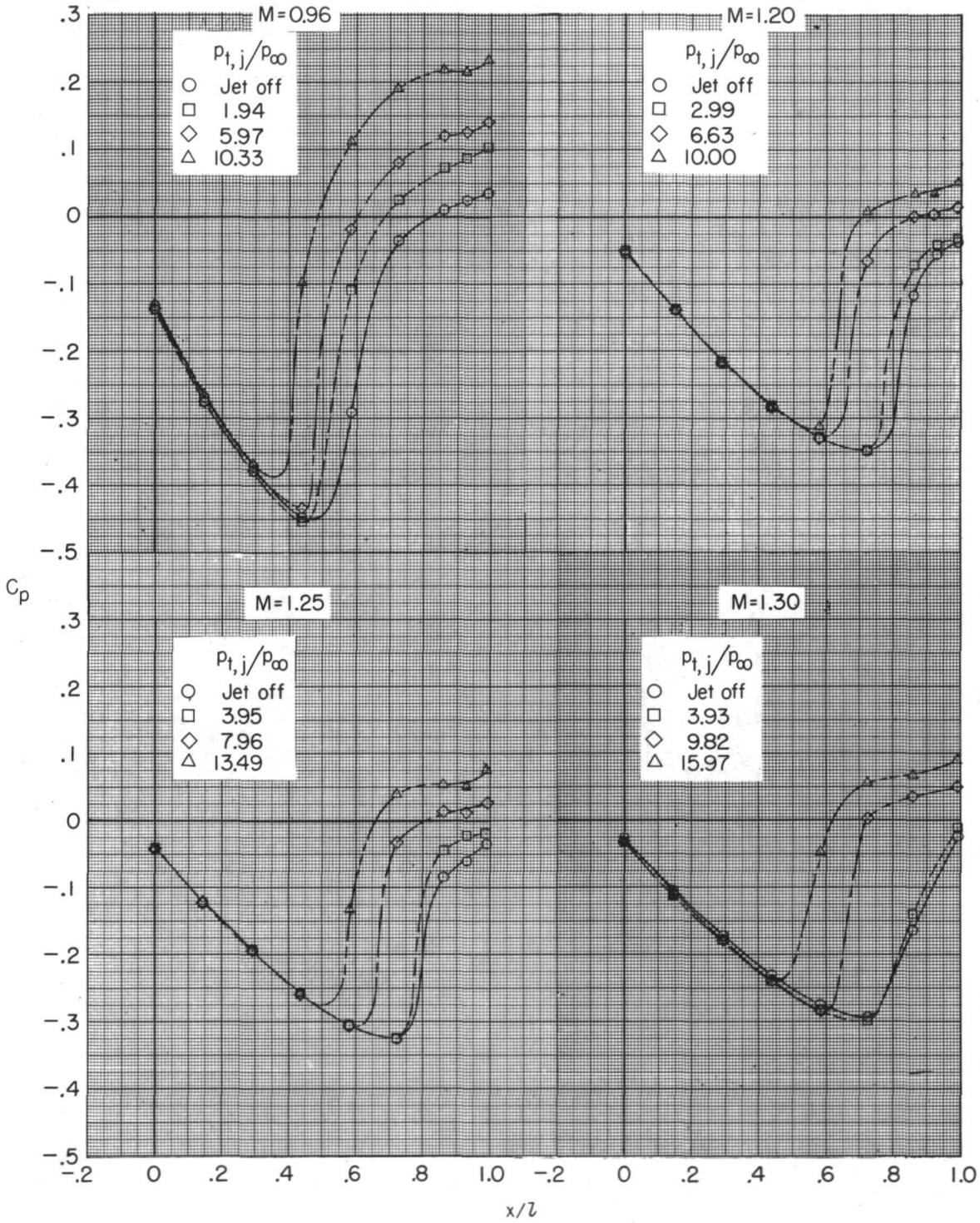

(b) M = 0.96, 1.20, 1.25, and 1.30.

Figure 15.- Concluded.

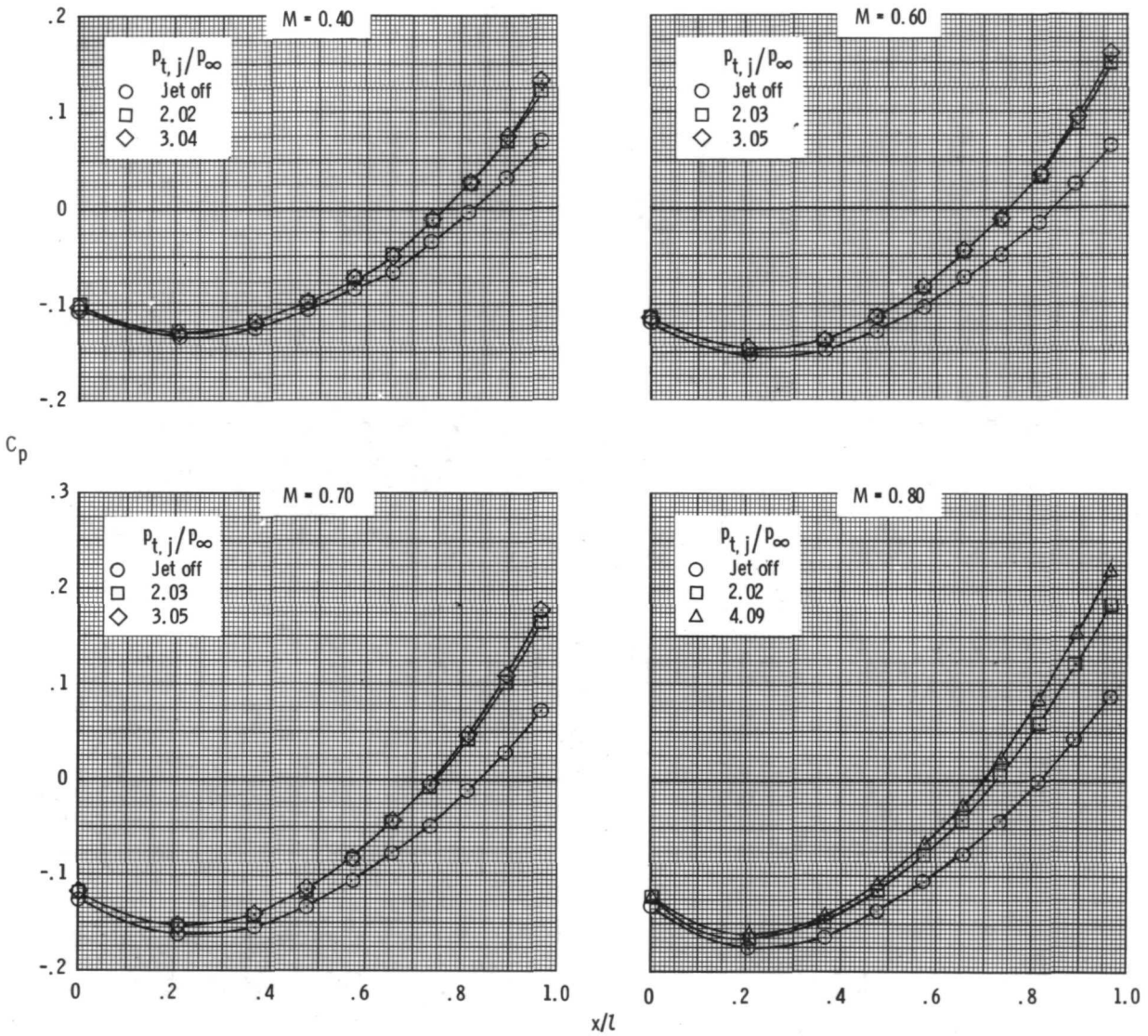

(a) M = 0.40, 0.60, 0.70, and 0.80.

Figure 16.- Boattail pressure coefficient distributions on configuration 3 $\left(l/d_m = 1.77\right)$ at various Mach numbers and three values of jet total-pressure ratio.

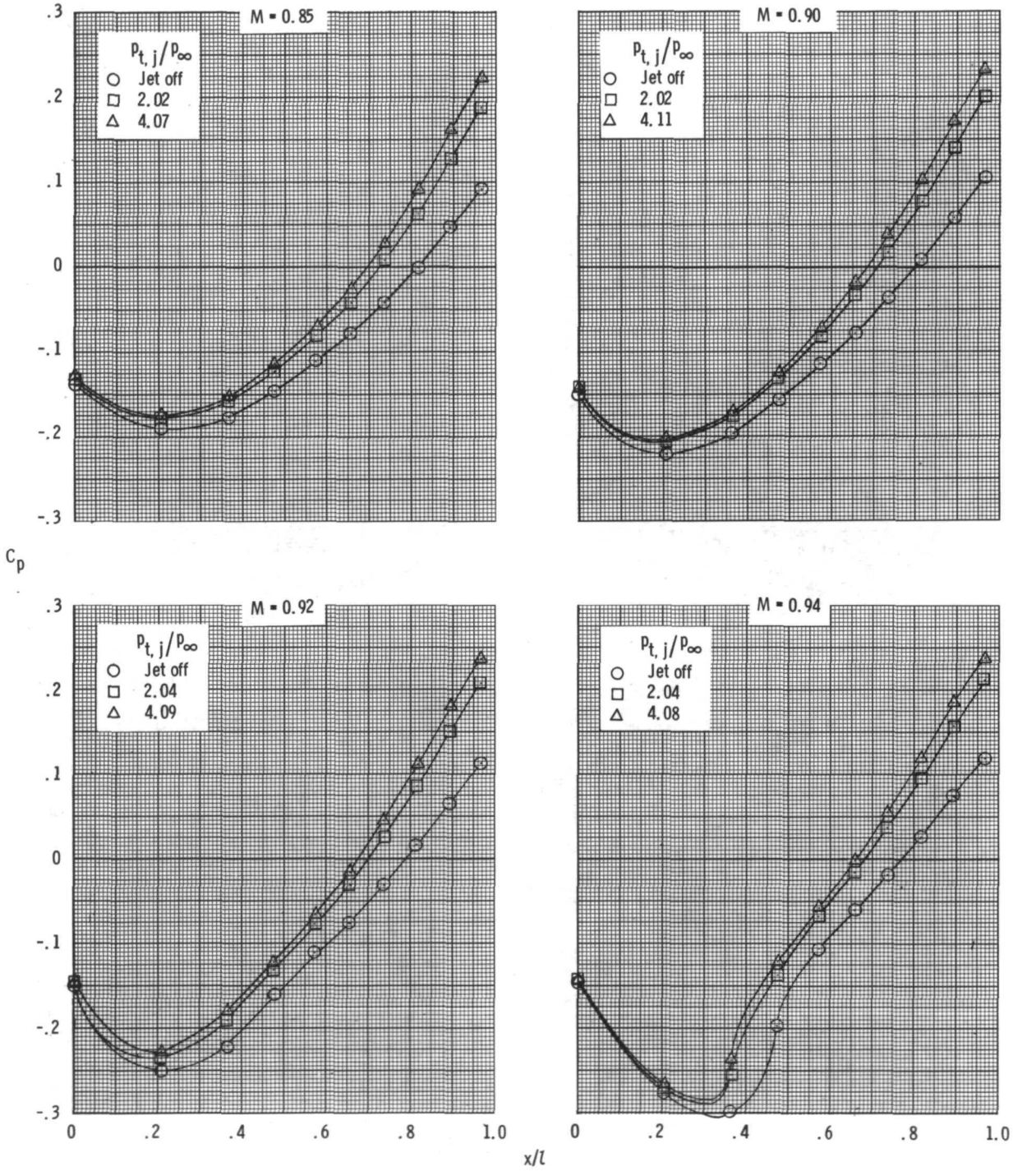

(b) M = 0.85, 0.90, 0.92, and 0.94.

Figure 16.- Continued.

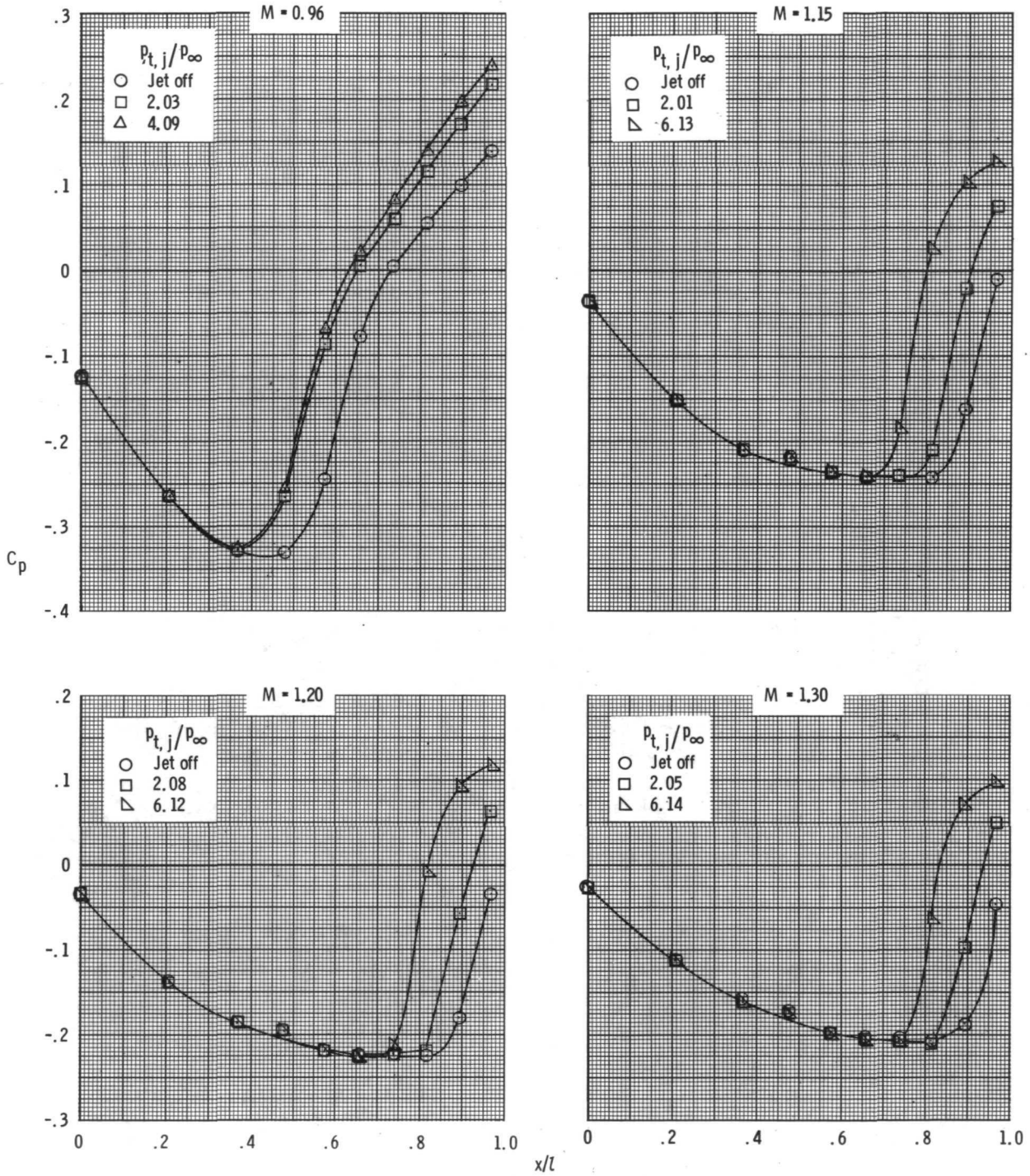

(c) M = 0.96, 1.15, 1.20, and 1.30.

Figure 16.- Concluded.

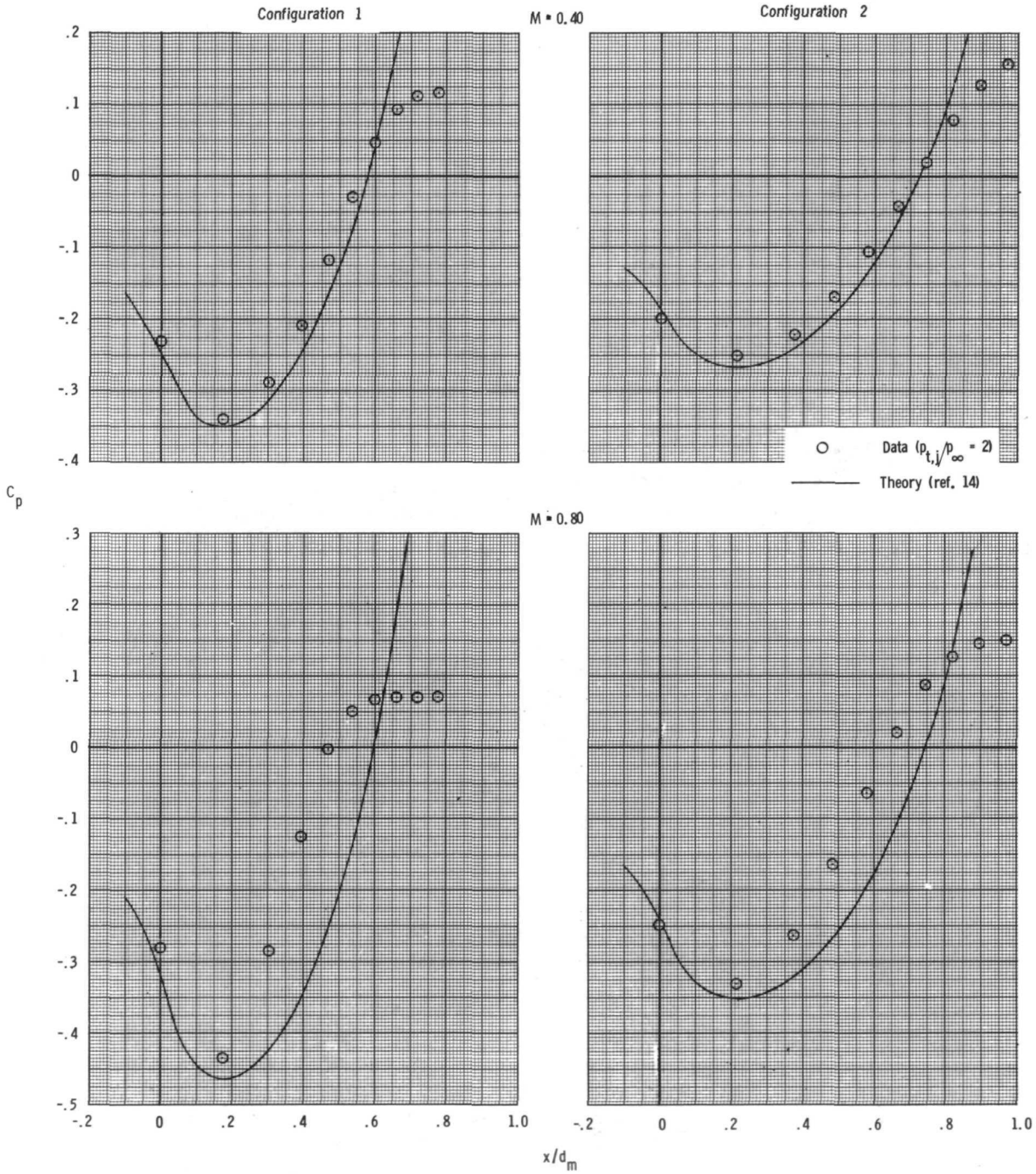

(a) Configurations 1 $\left(l/d_m = 0.80\right)$ and 2 $\left(l/d_m = 1.00\right)$.

Figure 17.- Comparison of measured boattail pressure coefficient distributions with those predicted by the theory of reference 14.

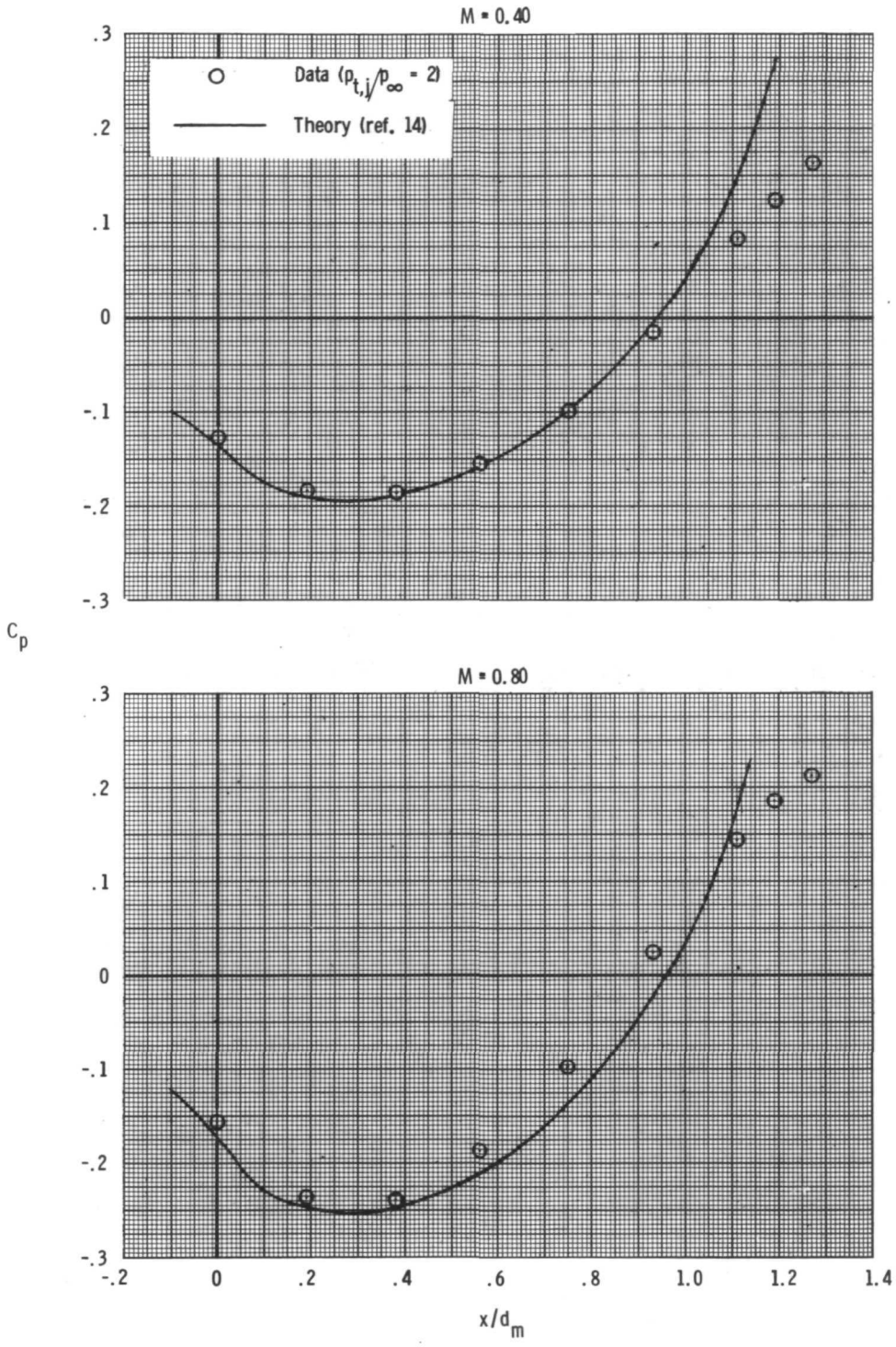

(b) STA configuration $(l/d_m = 1.29)$.

Figure 17.- Continued.

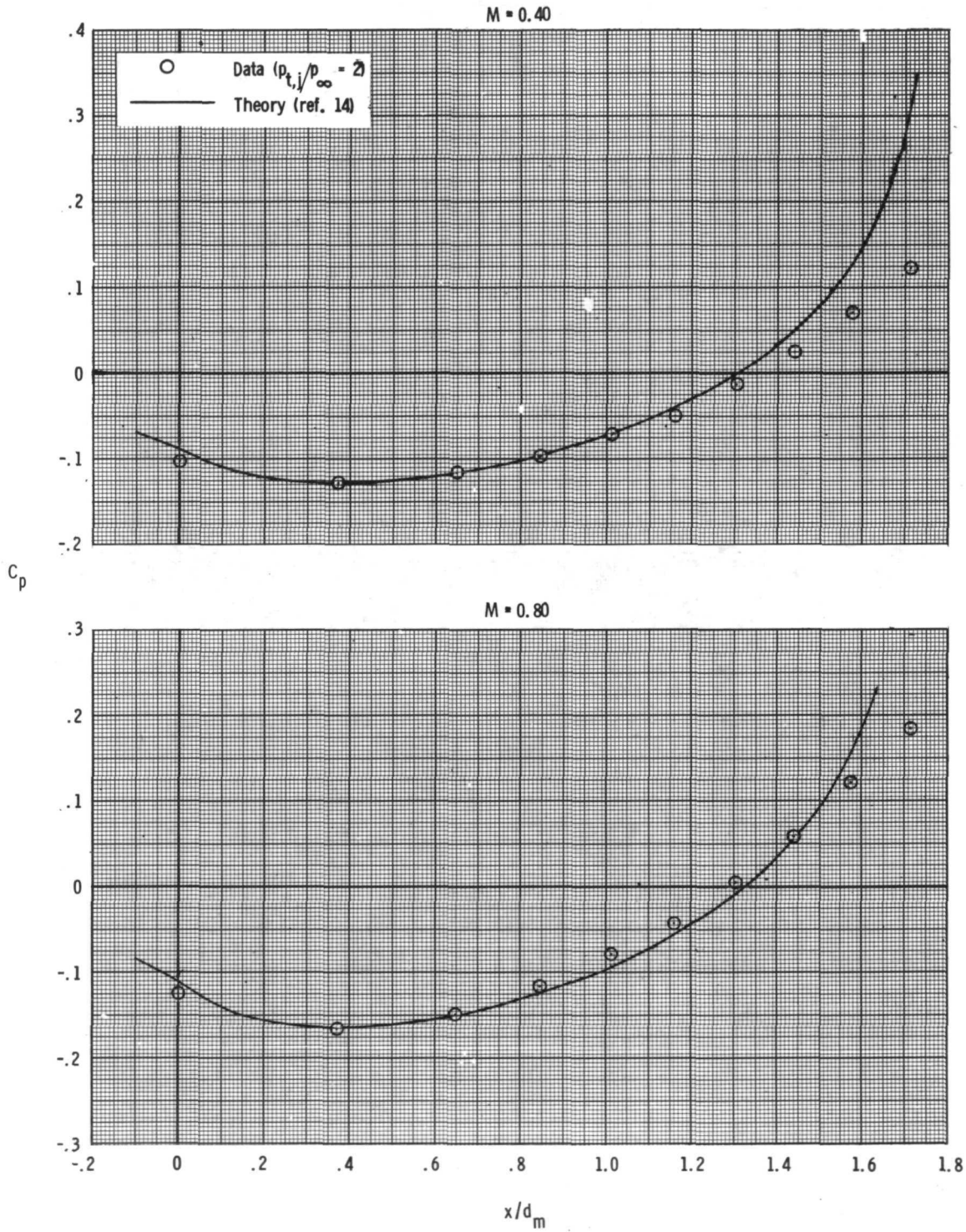

(c) Configuration 3 $\left(l/d_m = 1.77\right)$.

Figure 17.- Concluded.

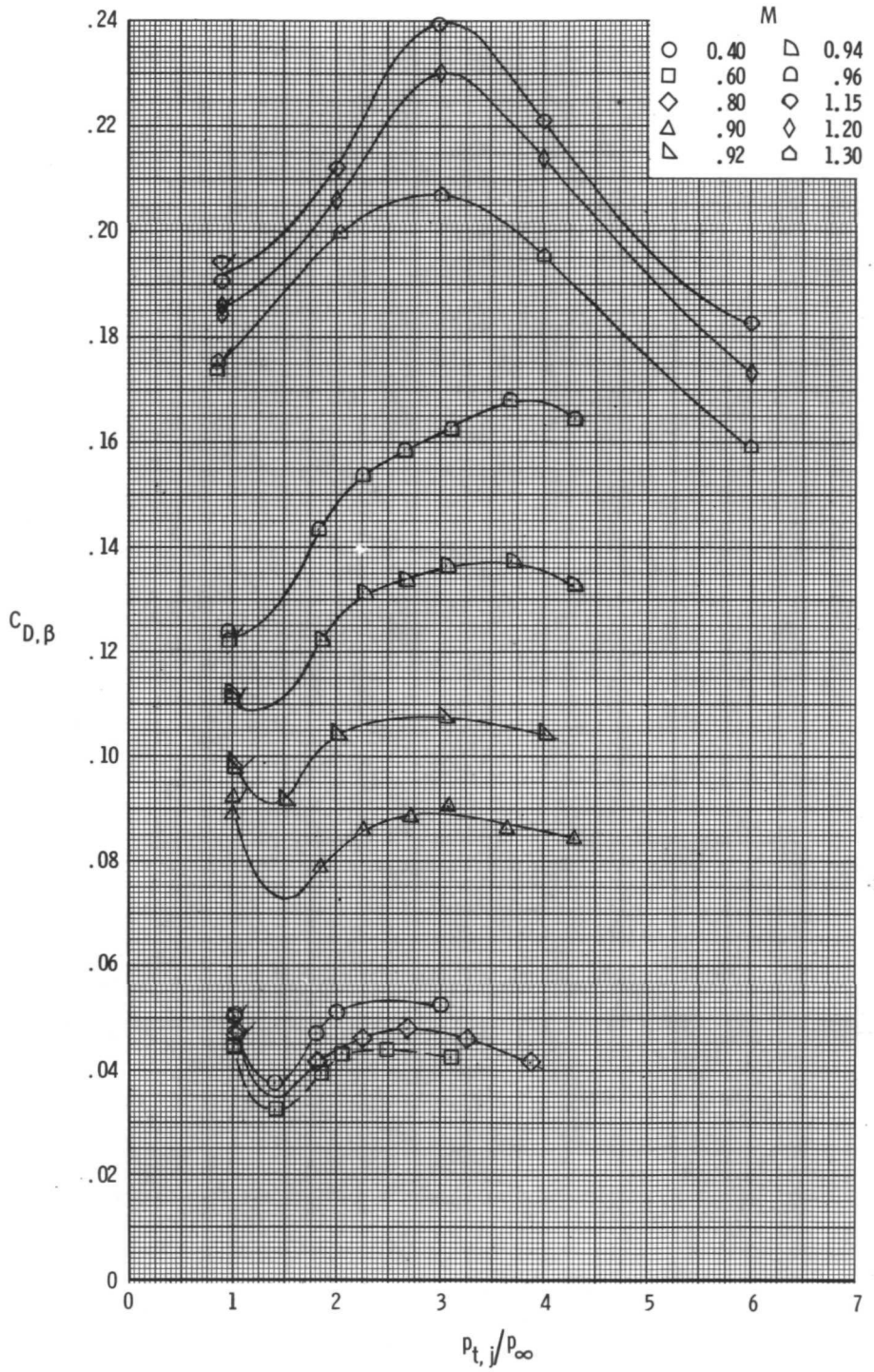

Figure 18.- Effect of jet total-pressure ratio on boattail pressure drag of configuration 1 $(l/d_m = 0.80)$ at various Mach numbers. Flags on symbols indicate repeat points.

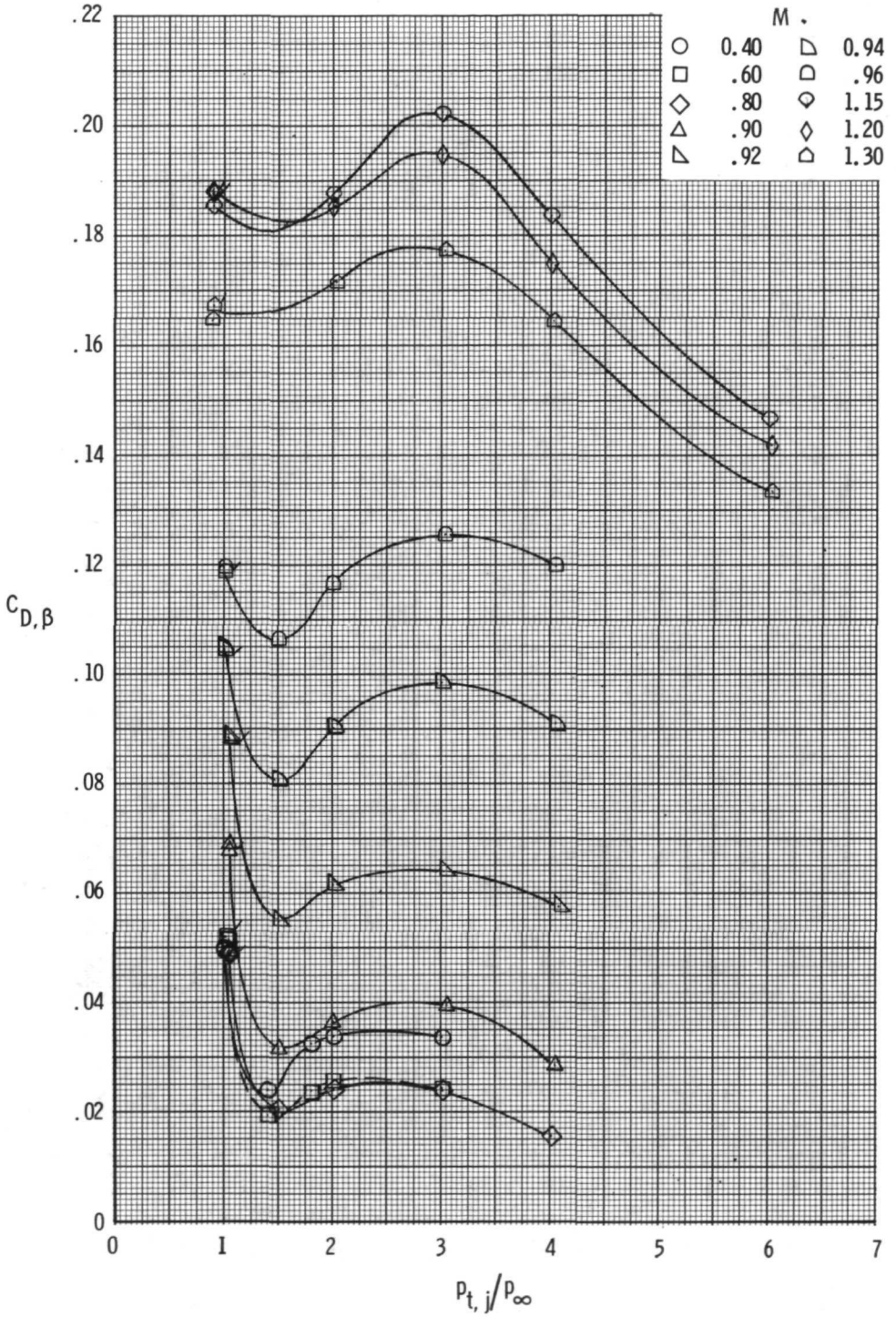

Figure 19.- Effect of jet total-pressure ratio on boattail pressure drag of configuration 2 $(l/d_m = 1.00)$ at various Mach numbers. Flags on symbols indicate repeat points.

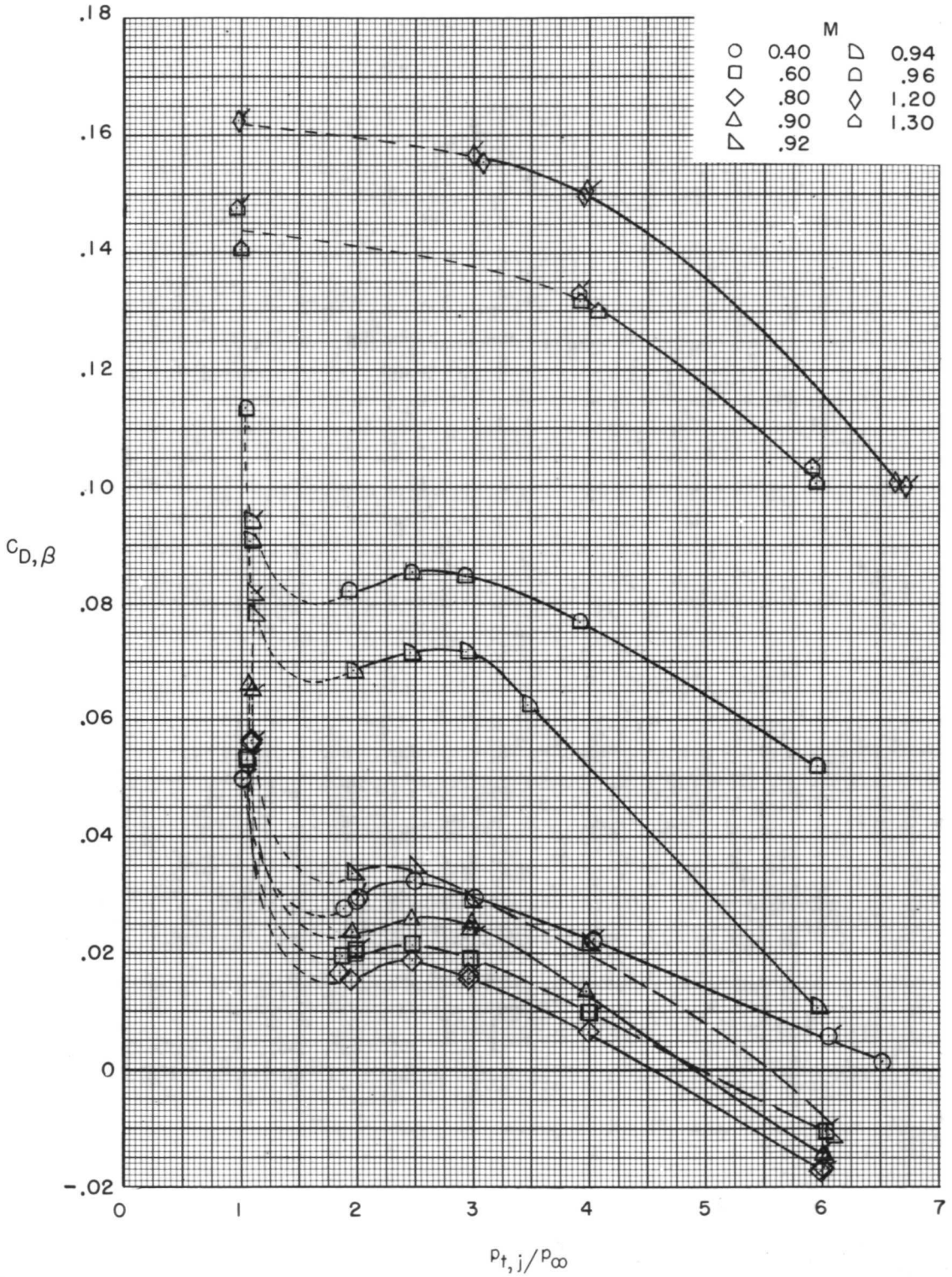

Figure 20.- Effect of jet total-pressure ratio on boattail pressure drag of STA configuration $\left(l/d_m = 1.29\right)$ at various Mach numbers. Flags on symbols indicate repeat points.

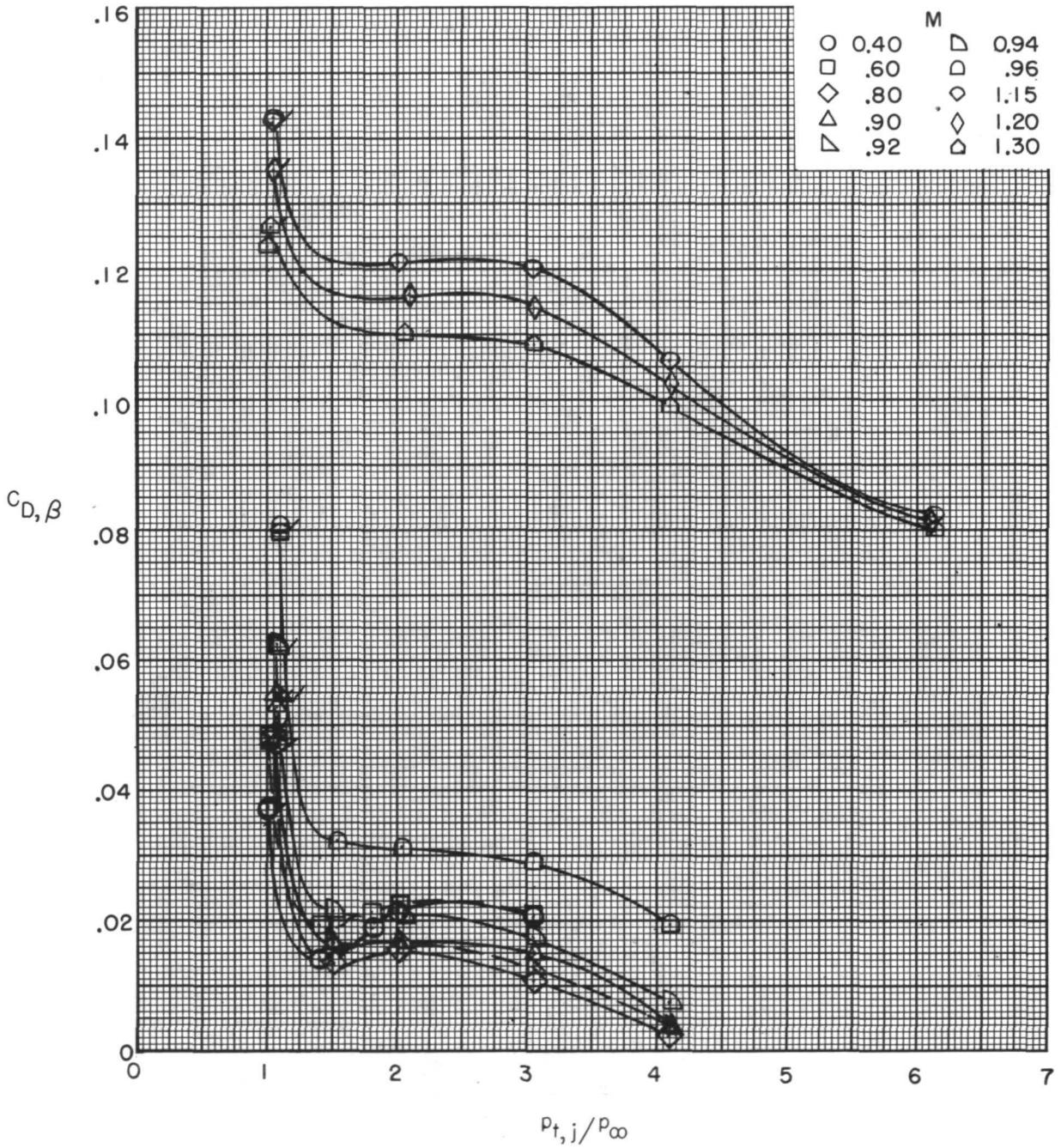

Figure 21.- Effect of jet total-pressure ratio on boattail pressure drag of configuration 3 $\left(l/d_m = 1.77\right)$ at various Mach numbers. Flags on symbols indicate repeat points.

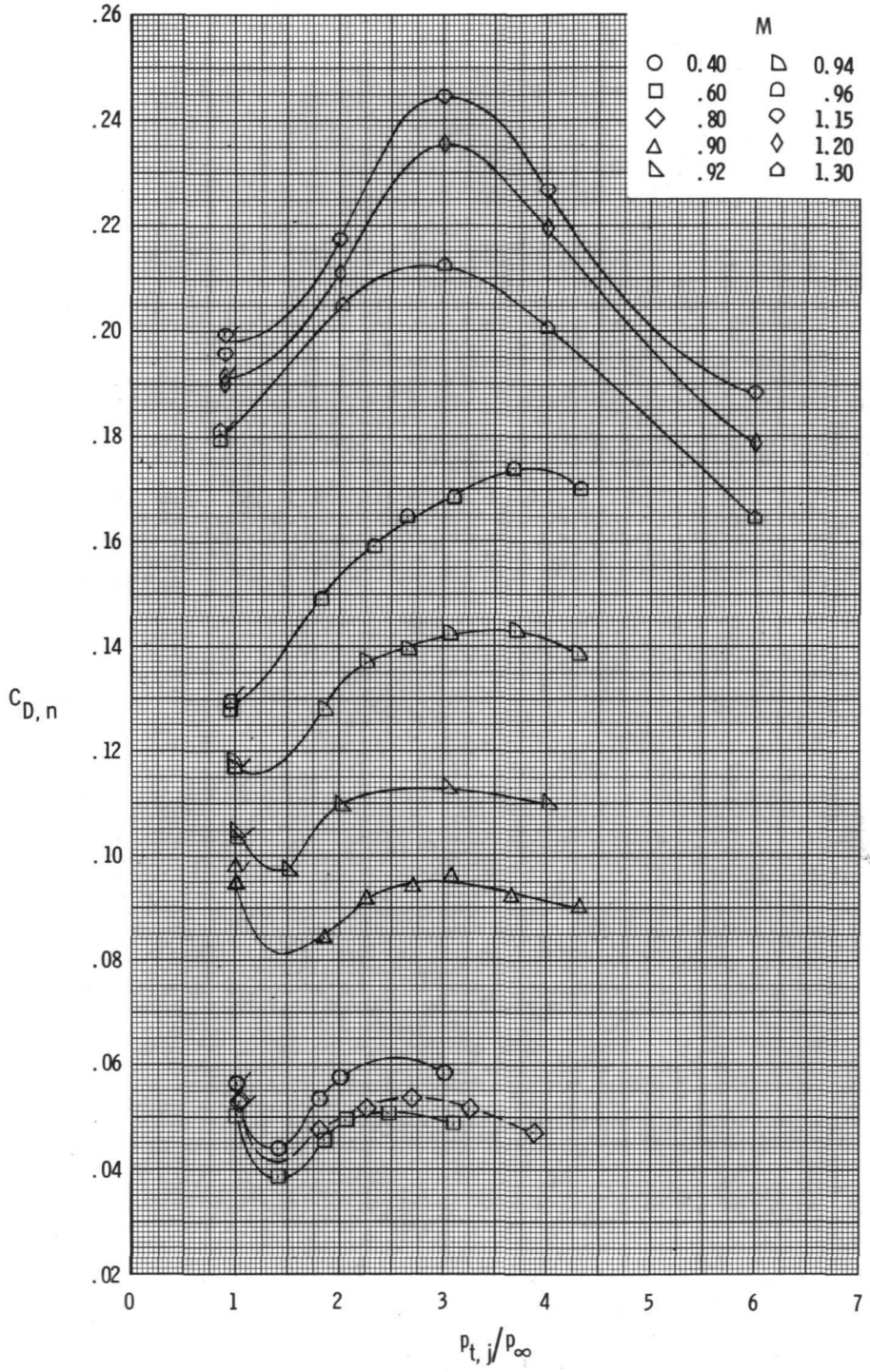

Figure 22.- Effect of jet total-pressure ratio on total boattail drag of configuration 1 $(l/d_m = 0.80)$ at various Mach numbers. Flags on symbols indicate repeat points.

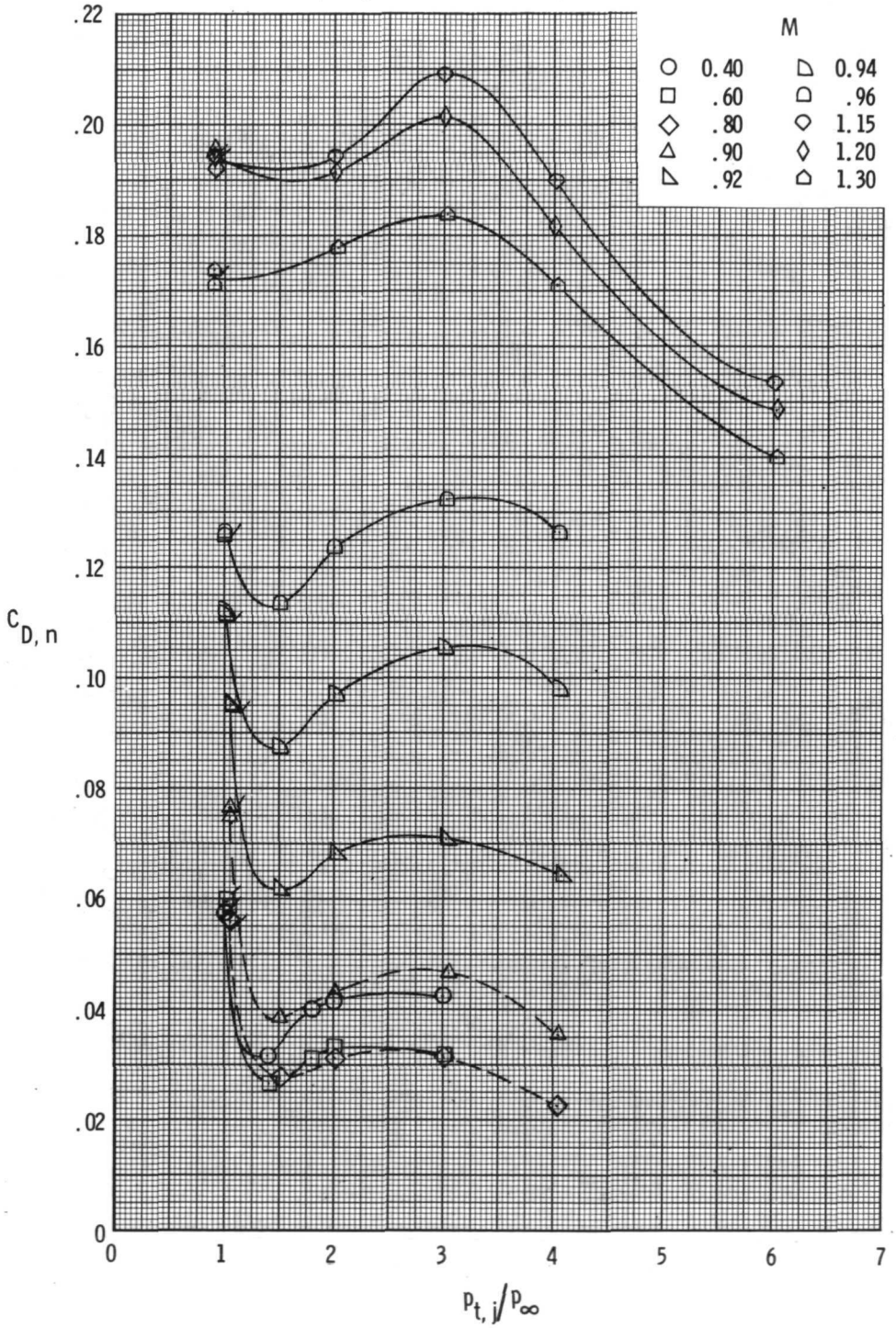

Figure 23.- Effect of jet total-pressure ratio on total boattail drag of configuration 2 $(l/d_m = 1.00)$ at various Mach numbers. Flags on symbols indicate repeat points.

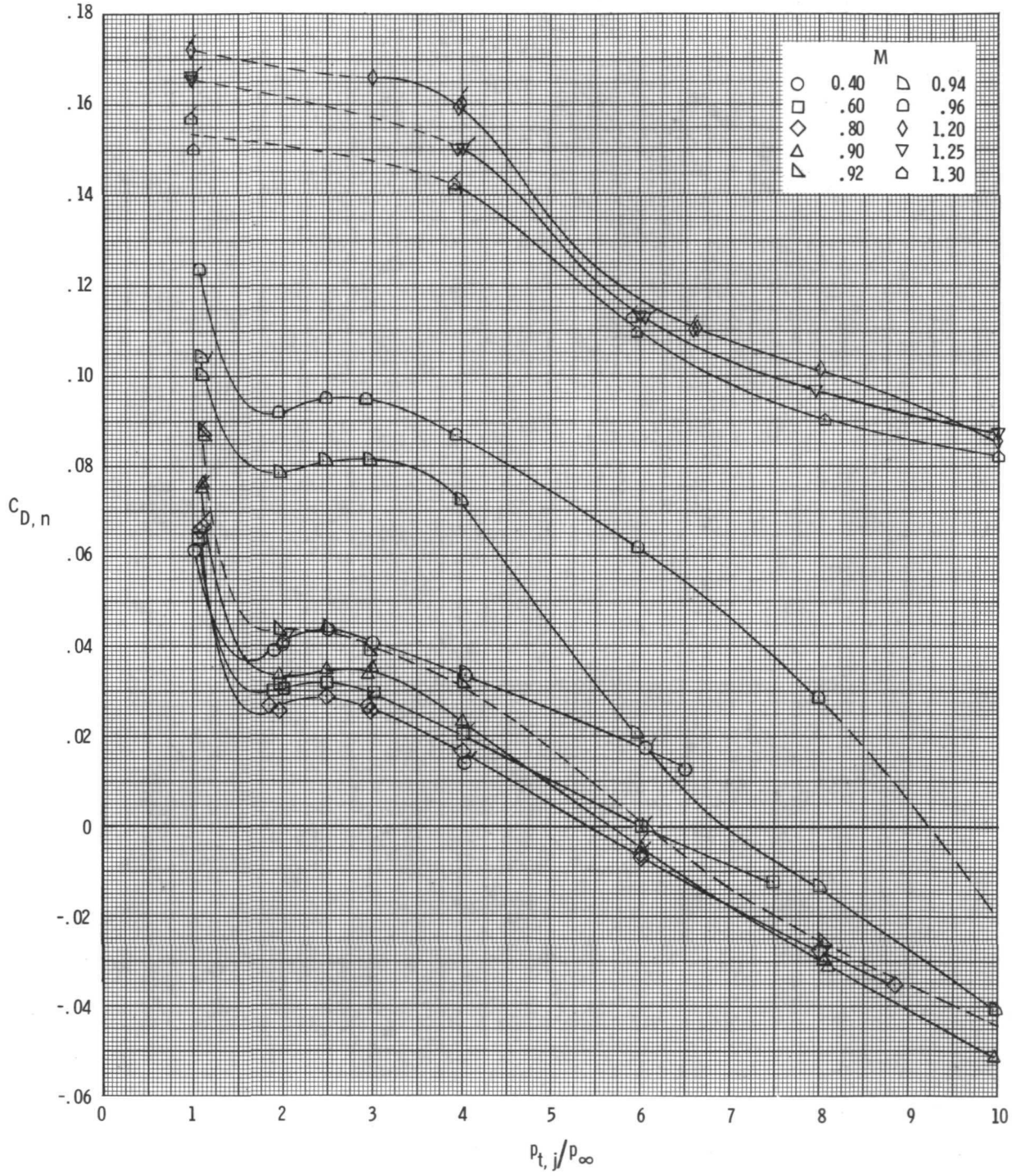

Figure 24.- Effect of jet total-pressure ratio on total boattail drag of STA configuration $(l/d_m = 1.29)$ at various Mach numbers. Flags on symbols indicate repeat points.

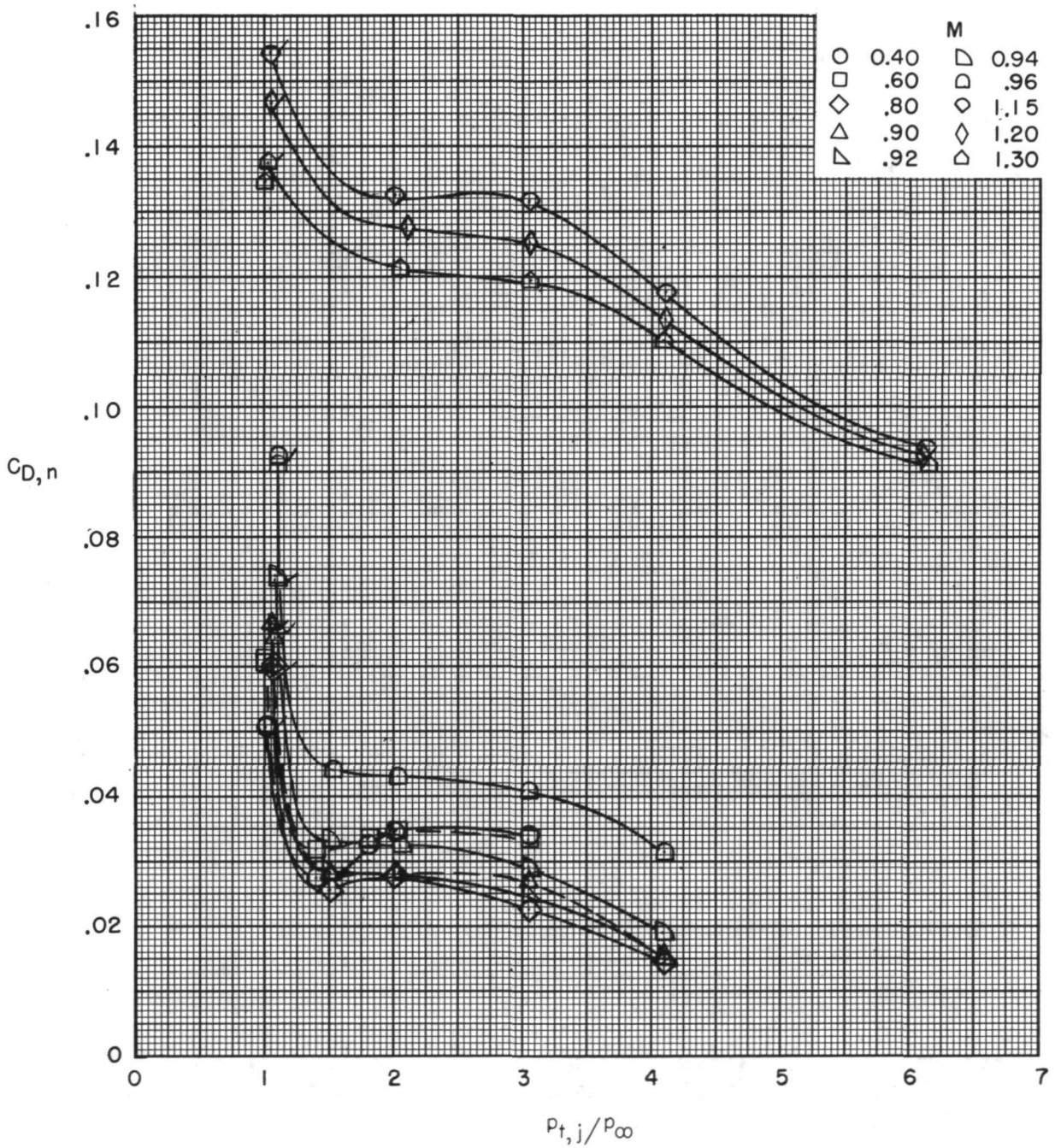

Figure 25.- Effect of jet total-pressure ratio on total boattail drag of configuration 3 $(l/d_m = 1.77)$ at various Mach numbers. Flags on symbols indicate repeat points.

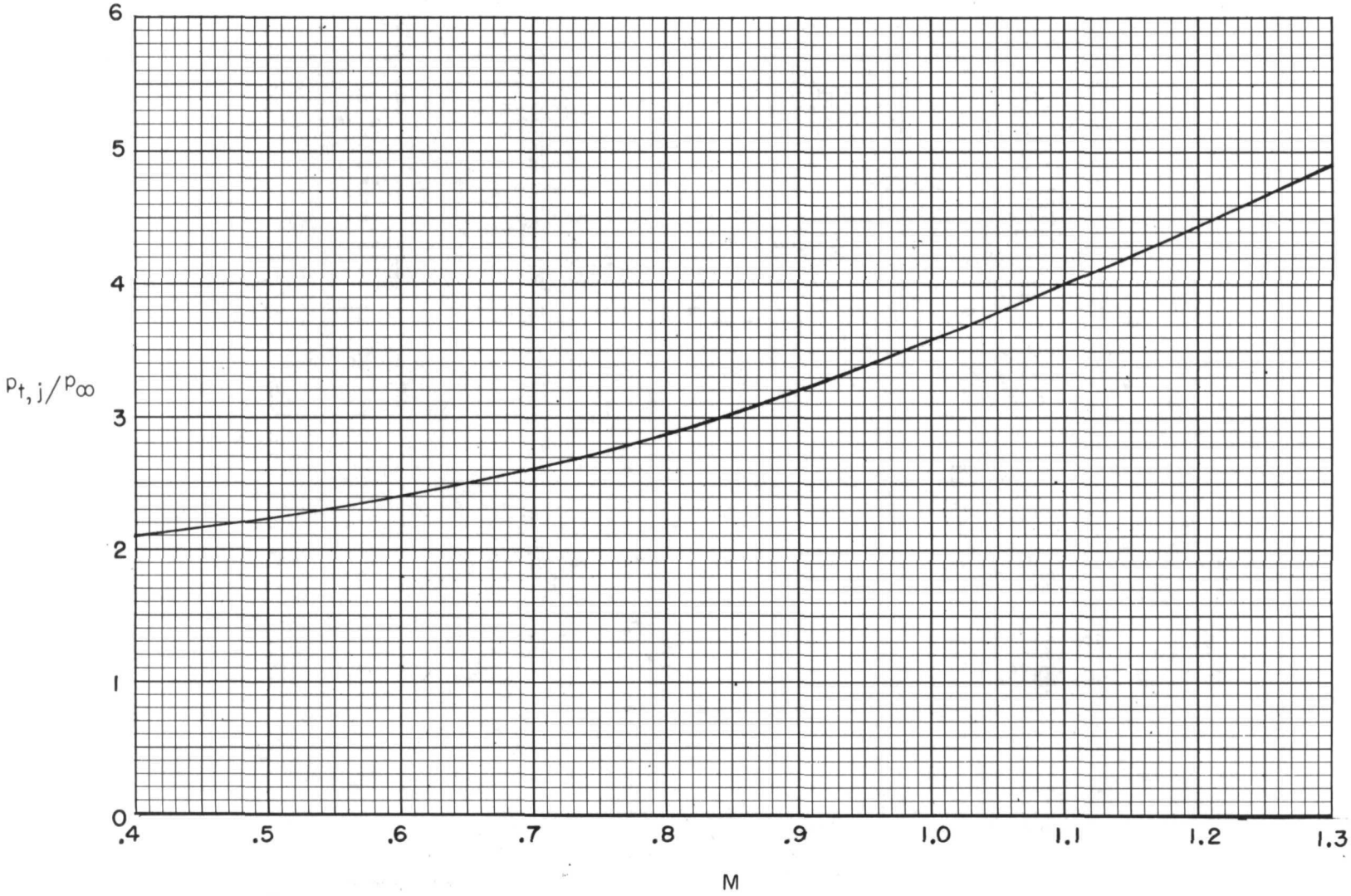

Figure 26.- Variation of nozzle pressure ratio with Mach number for a typical fighter airplane.

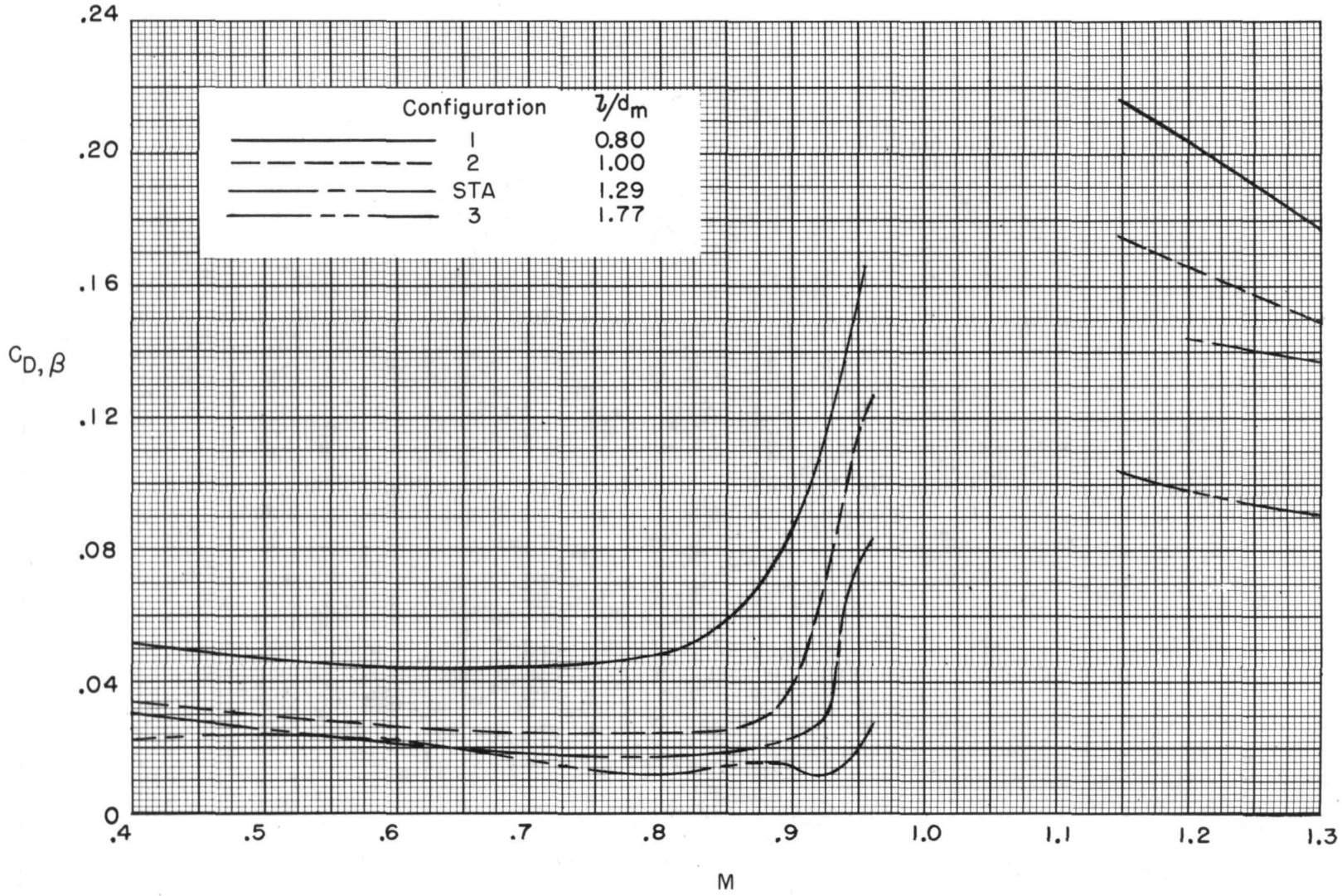

Figure 27.- Variation of boattail pressure drag with Mach number for all configurations at the pressure-ratio schedule of figure 26. .

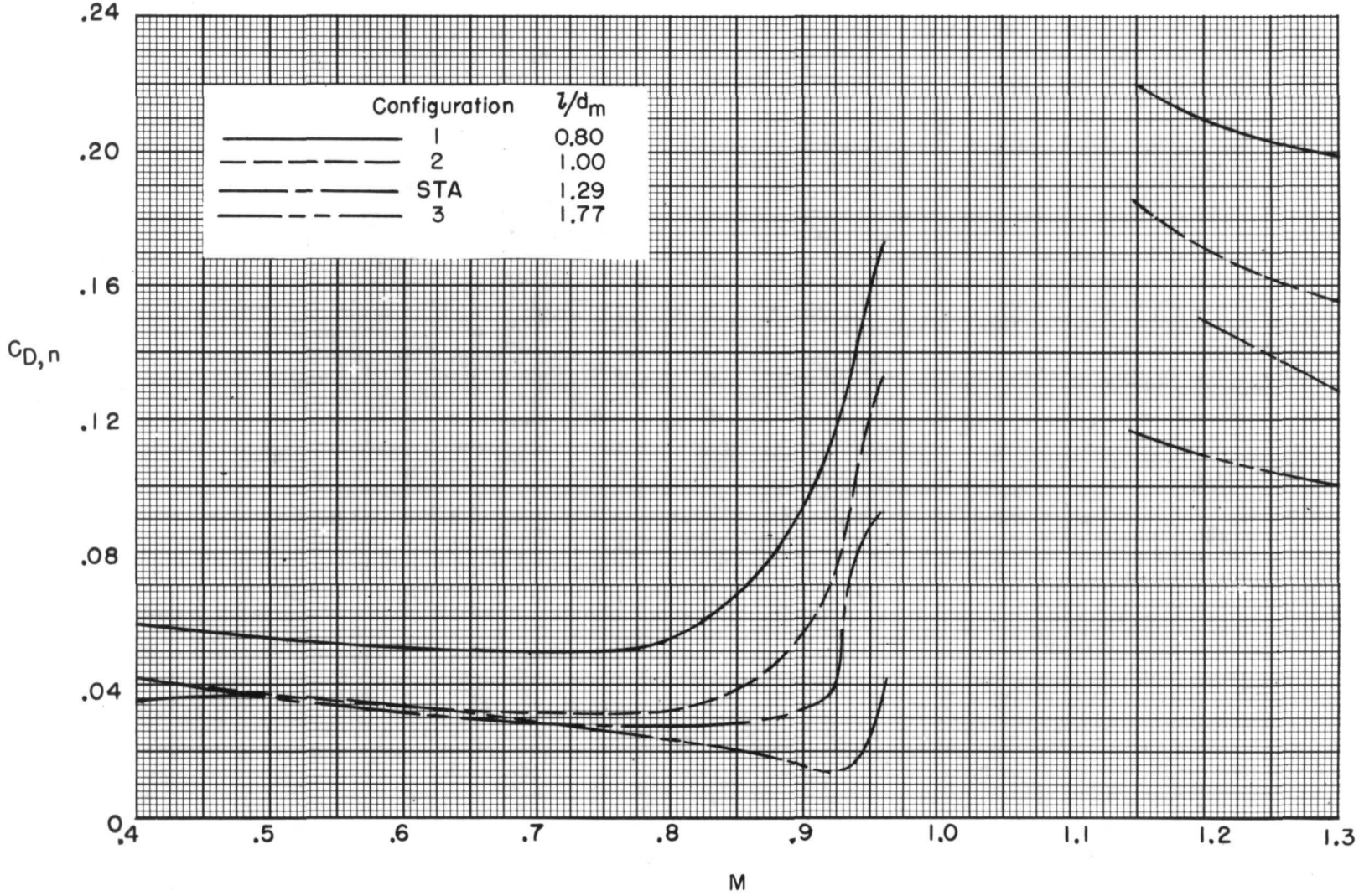

Figure 28.- Variation of total boattail drag with Mach number for all configurations at the pressure-ratio schedule of figure 26.

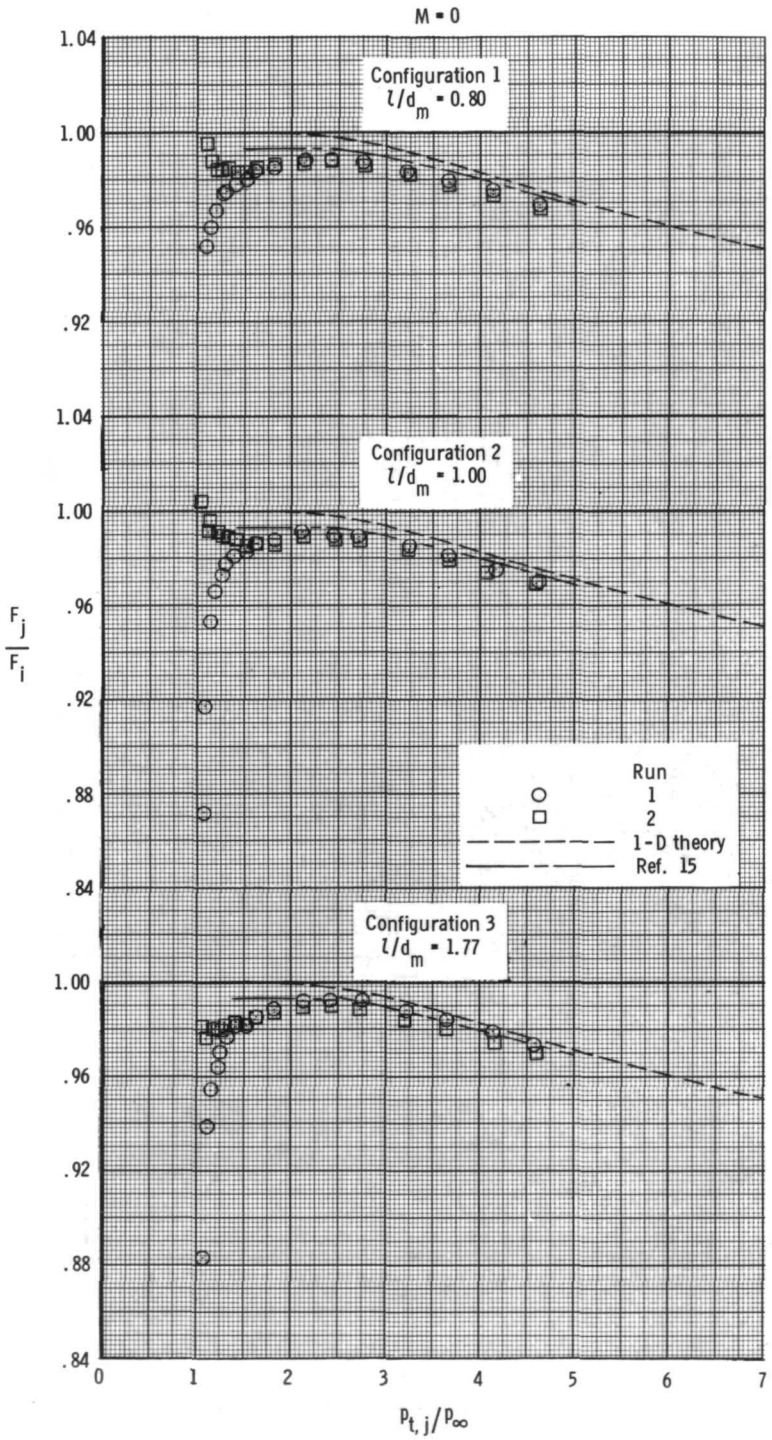

Figure 29.- Variation of static thrust ratio with jet total-pressure ratio for configurations 1, 2, and 3.

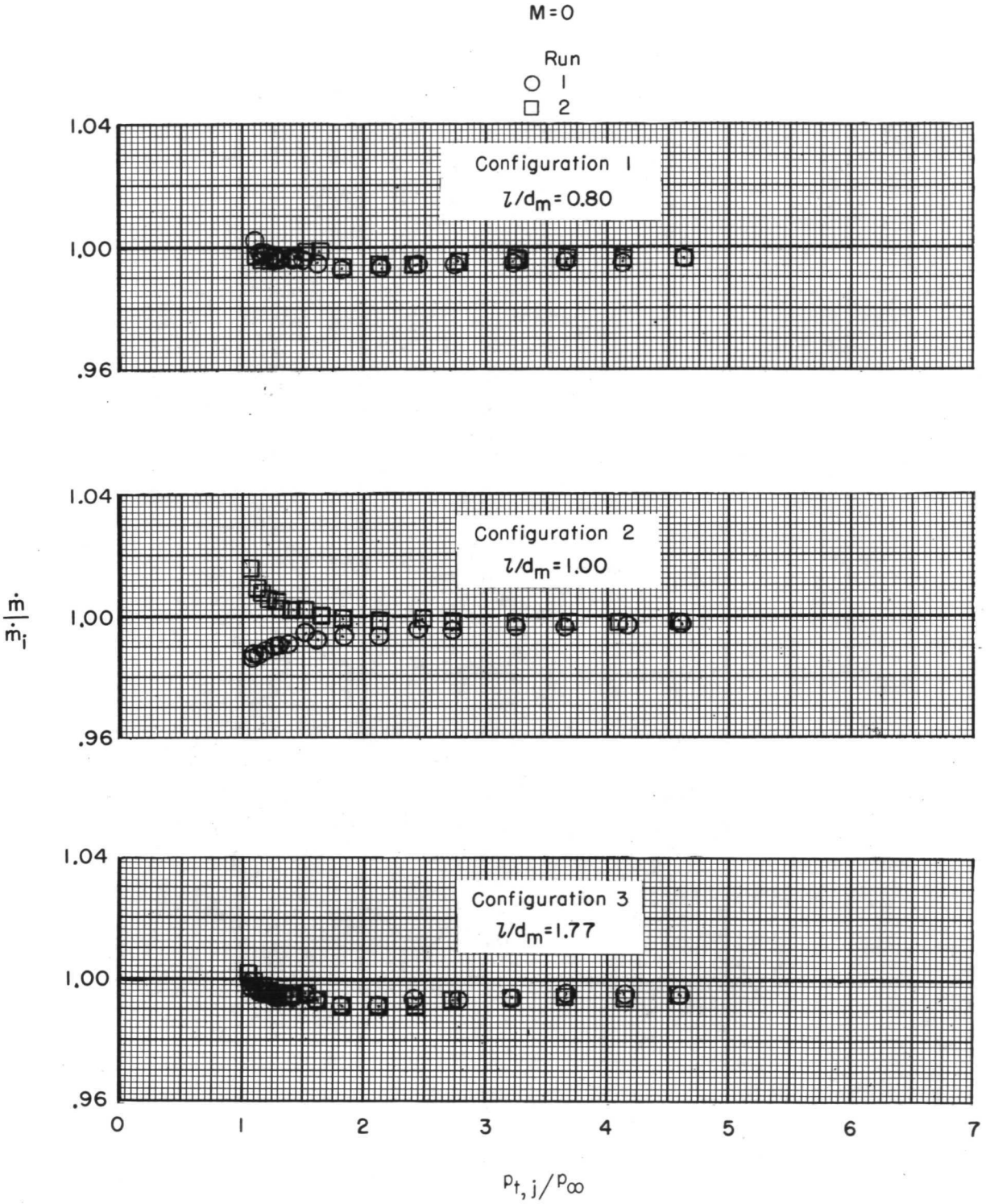

Figure 30.- Variation of static mass-flow ratio with jet total-pressure ratio for configurations 1, 2, and 3.

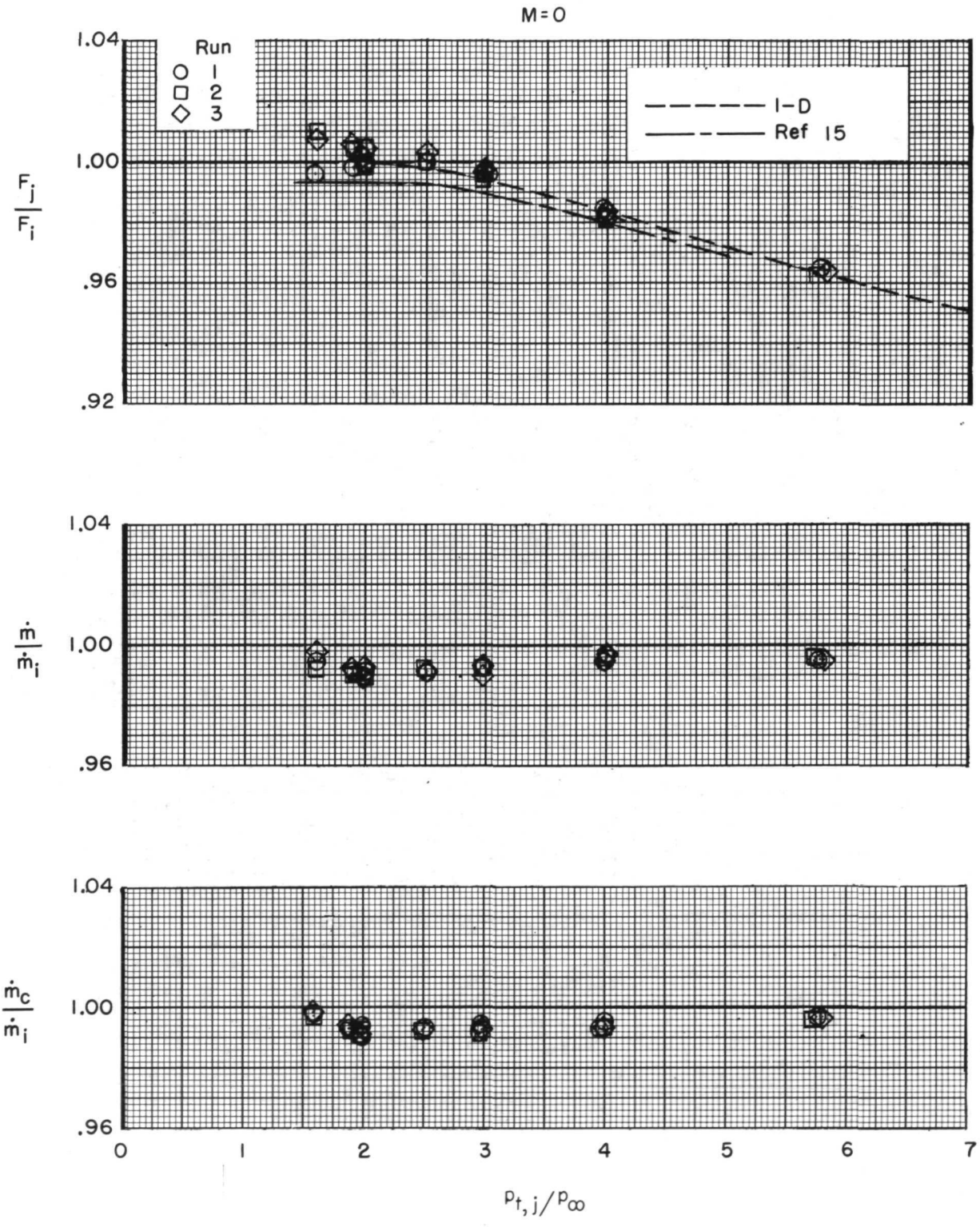

Figure 31.- Variation of static thrust ratio and mass-flow ratio with jet total-pressure ratio for STA configuration.

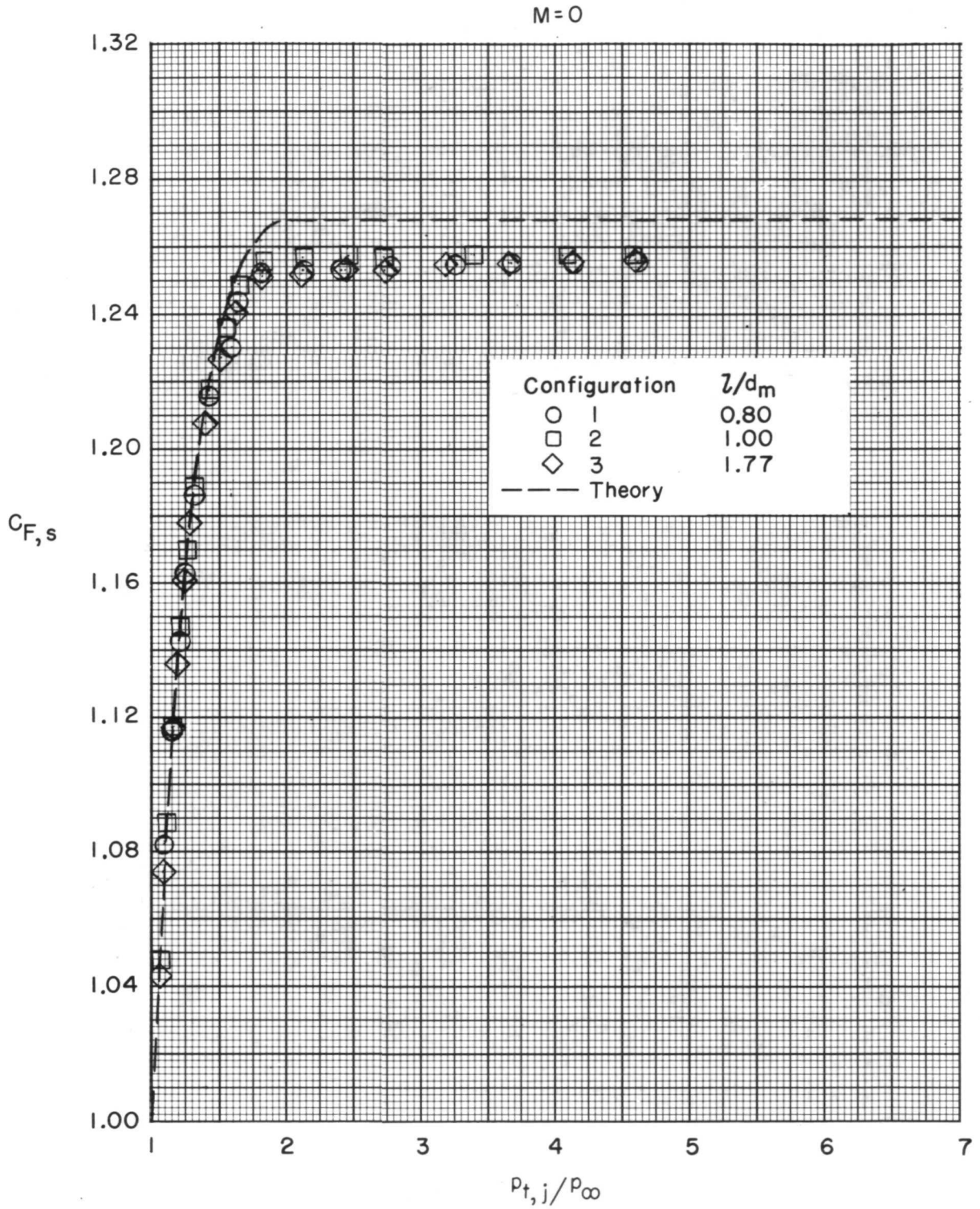

(a) Configurations 1, 2, and 3.

Figure 32.- Variation of static stream thrust coefficient with jet total-pressure ratio.

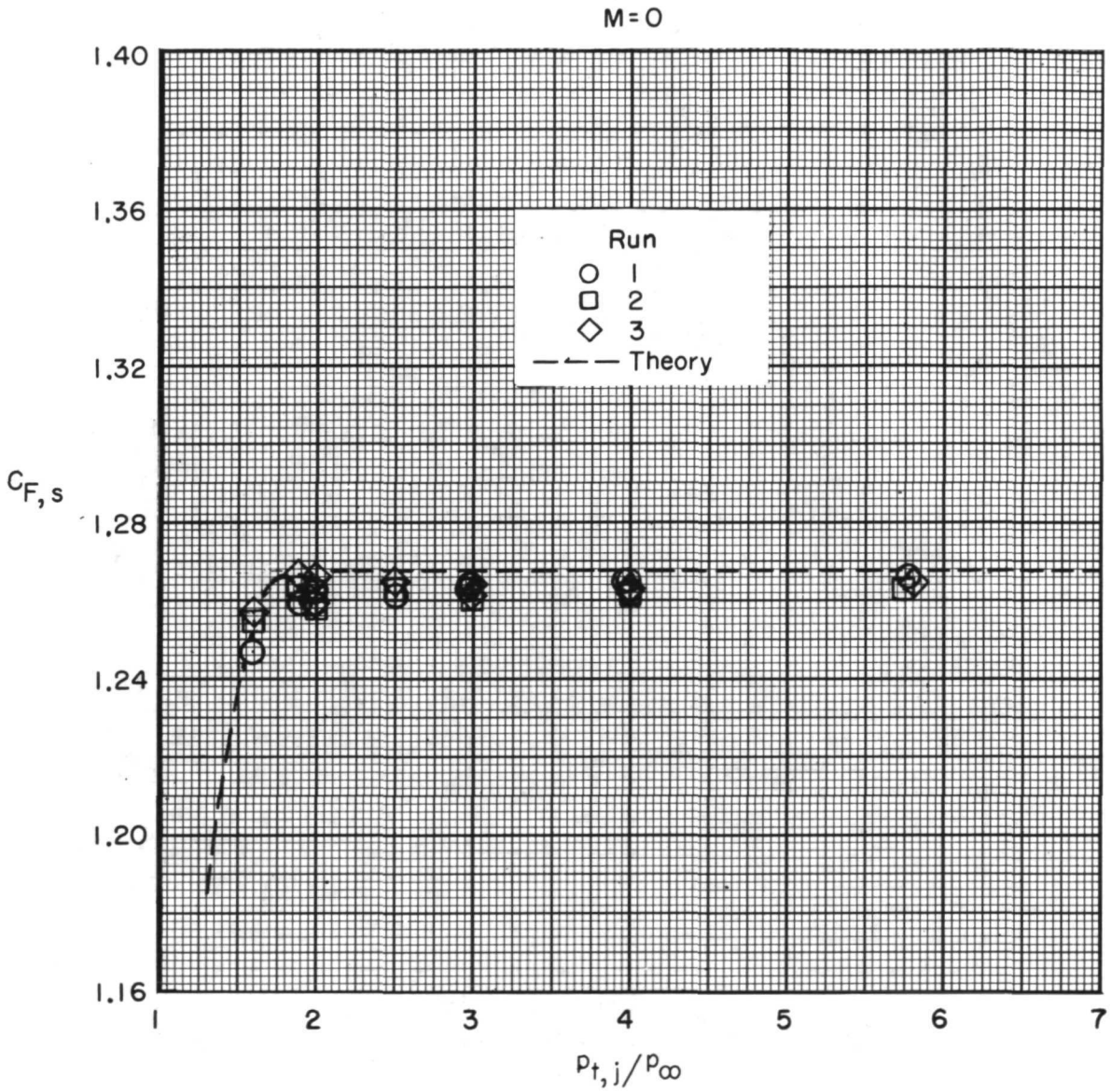

(b) STA configuration.

Figure 32.- Concluded.

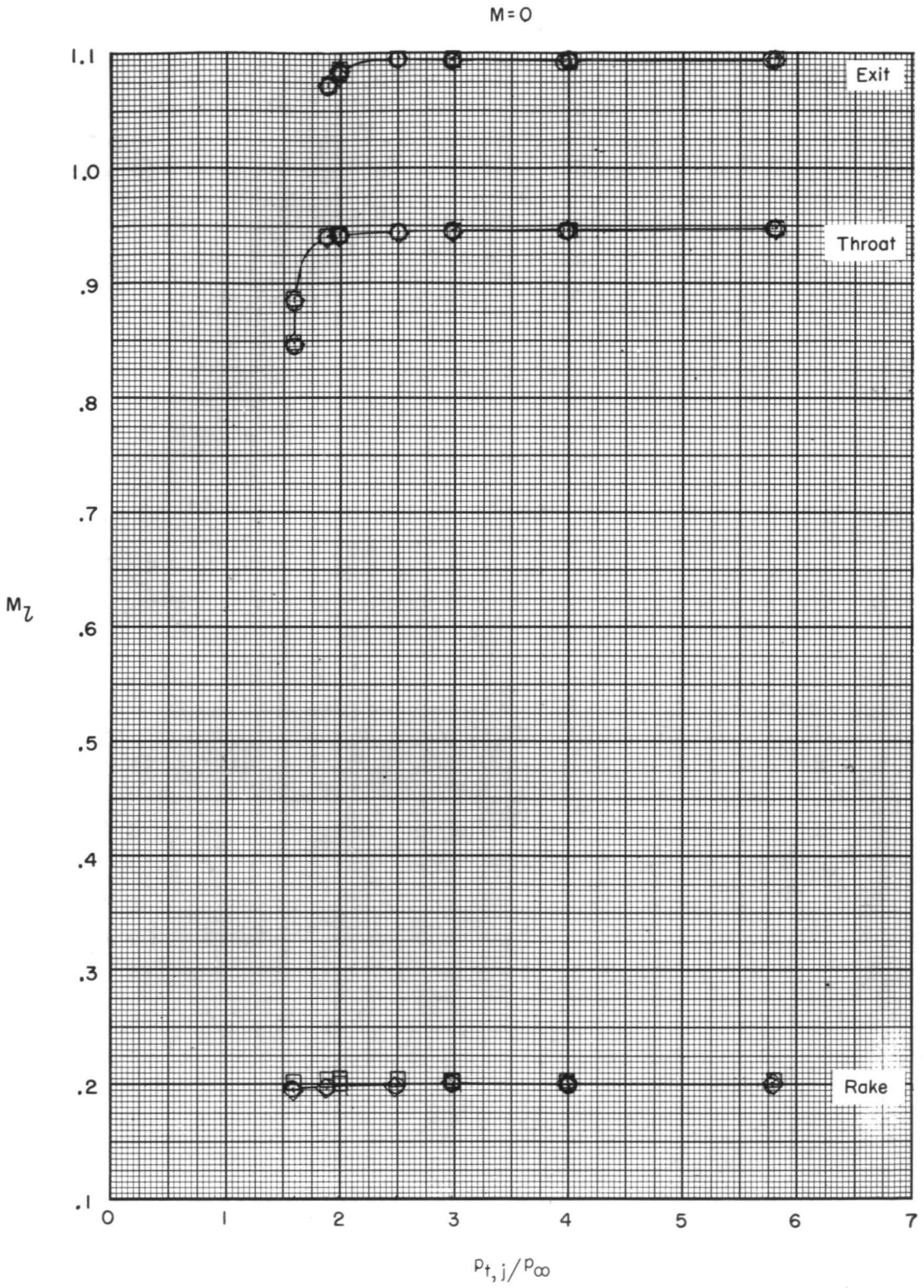

Figure 33.- Internal Mach numbers in STA configuration.

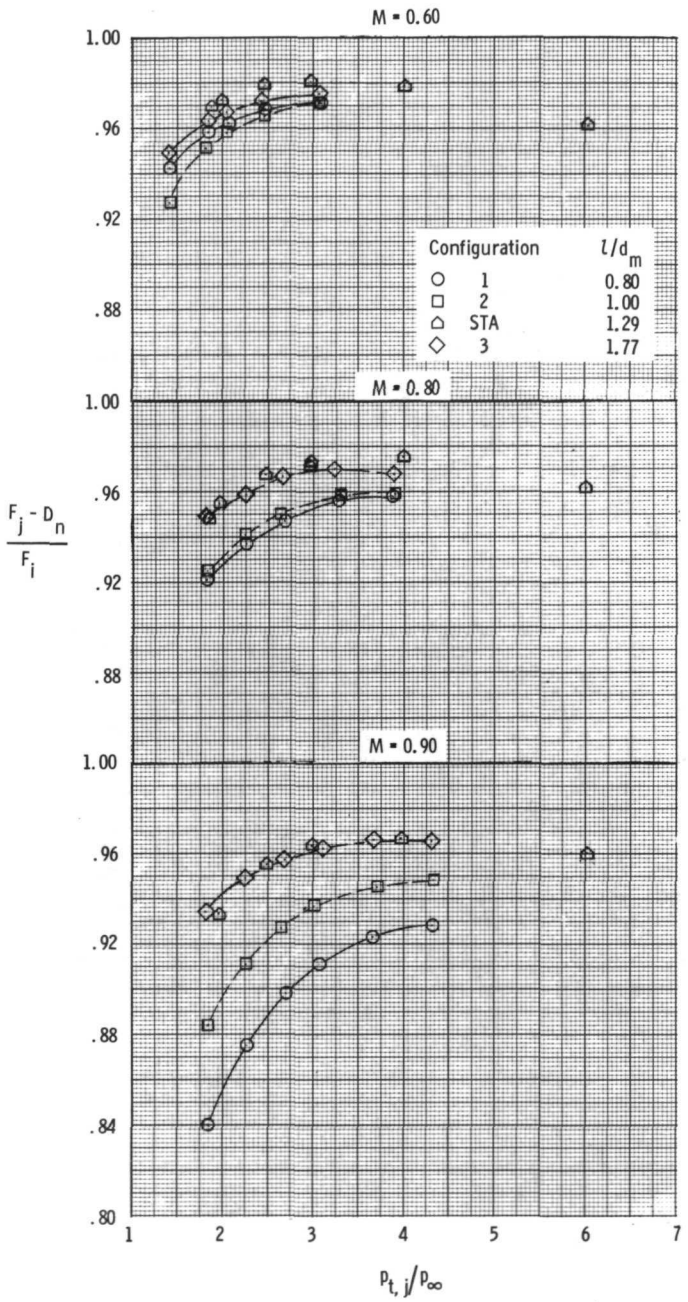

(a) M = 0.60, 0.80, and 0.90.

Figure 34.- Variation of thrust-minus-drag ratio with jet total-pressure ratio at several Mach numbers for all configurations.

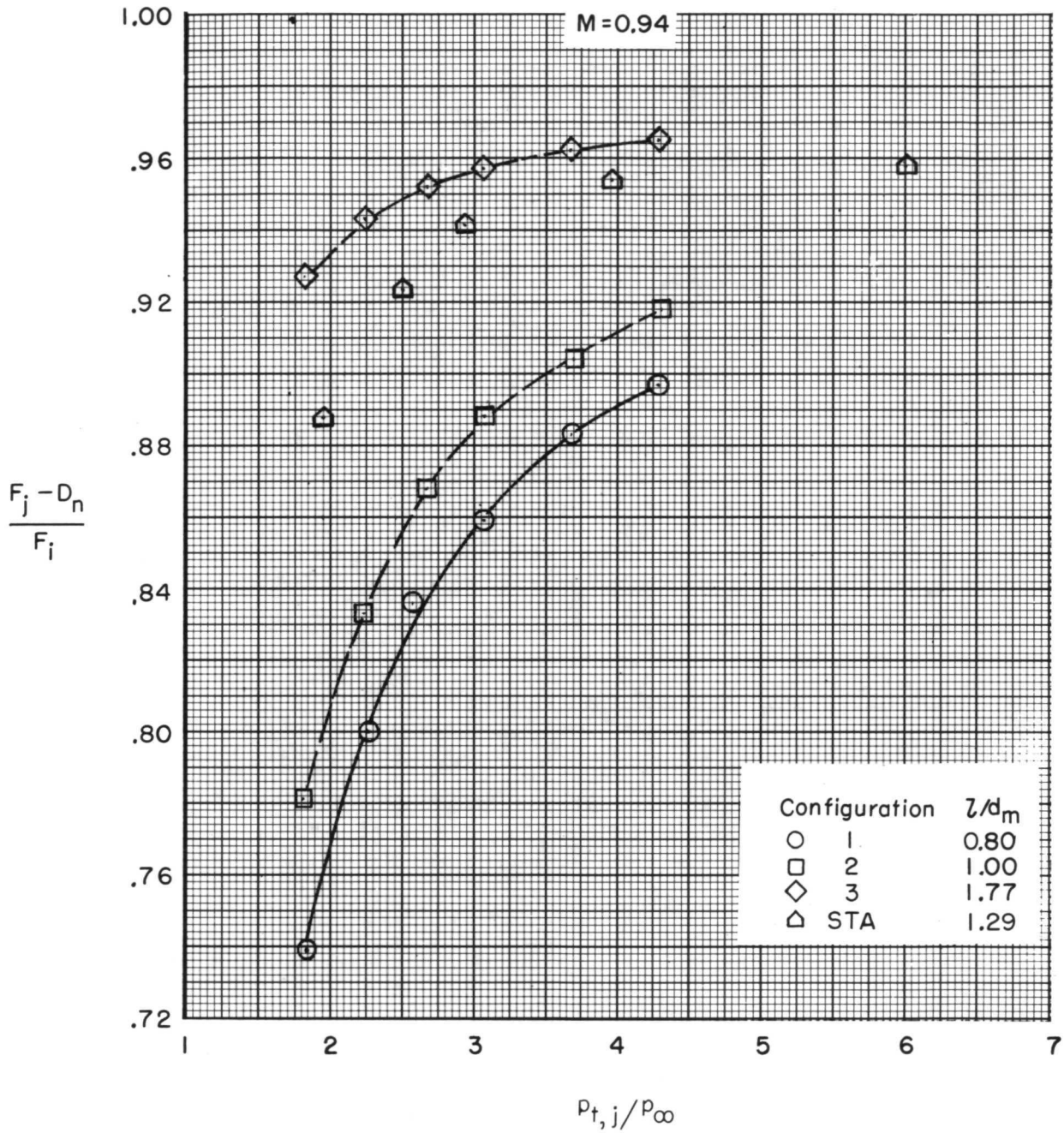

(b) M = 0.94.

Figure 34.- Continued.

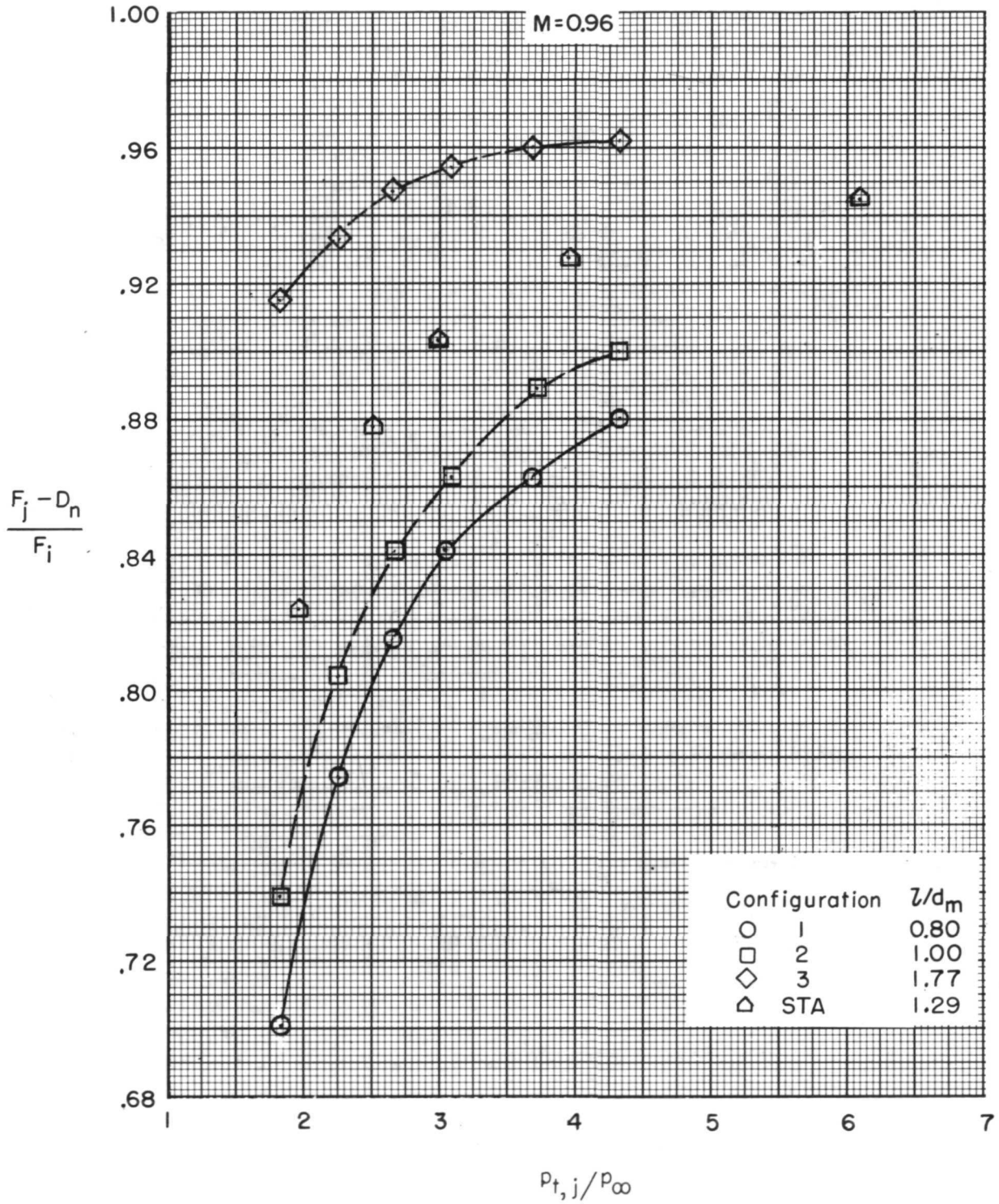

(c) M = 0.96.

Figure 34.- Concluded.

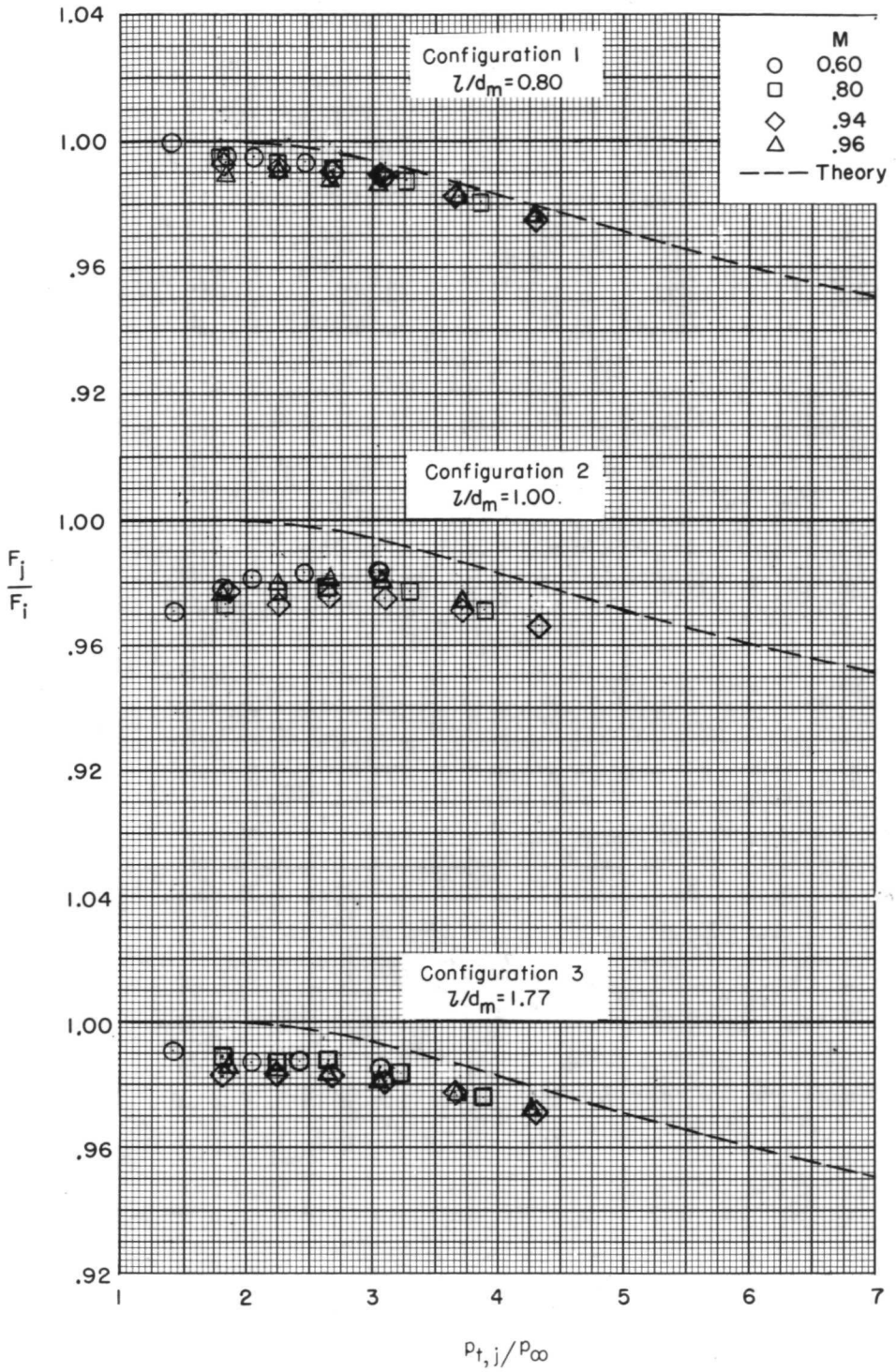

(a) Configurations 1, 2, and 3.

Figure 35.- Variation of thrust ratio with jet total-pressure ratio at various Mach numbers.

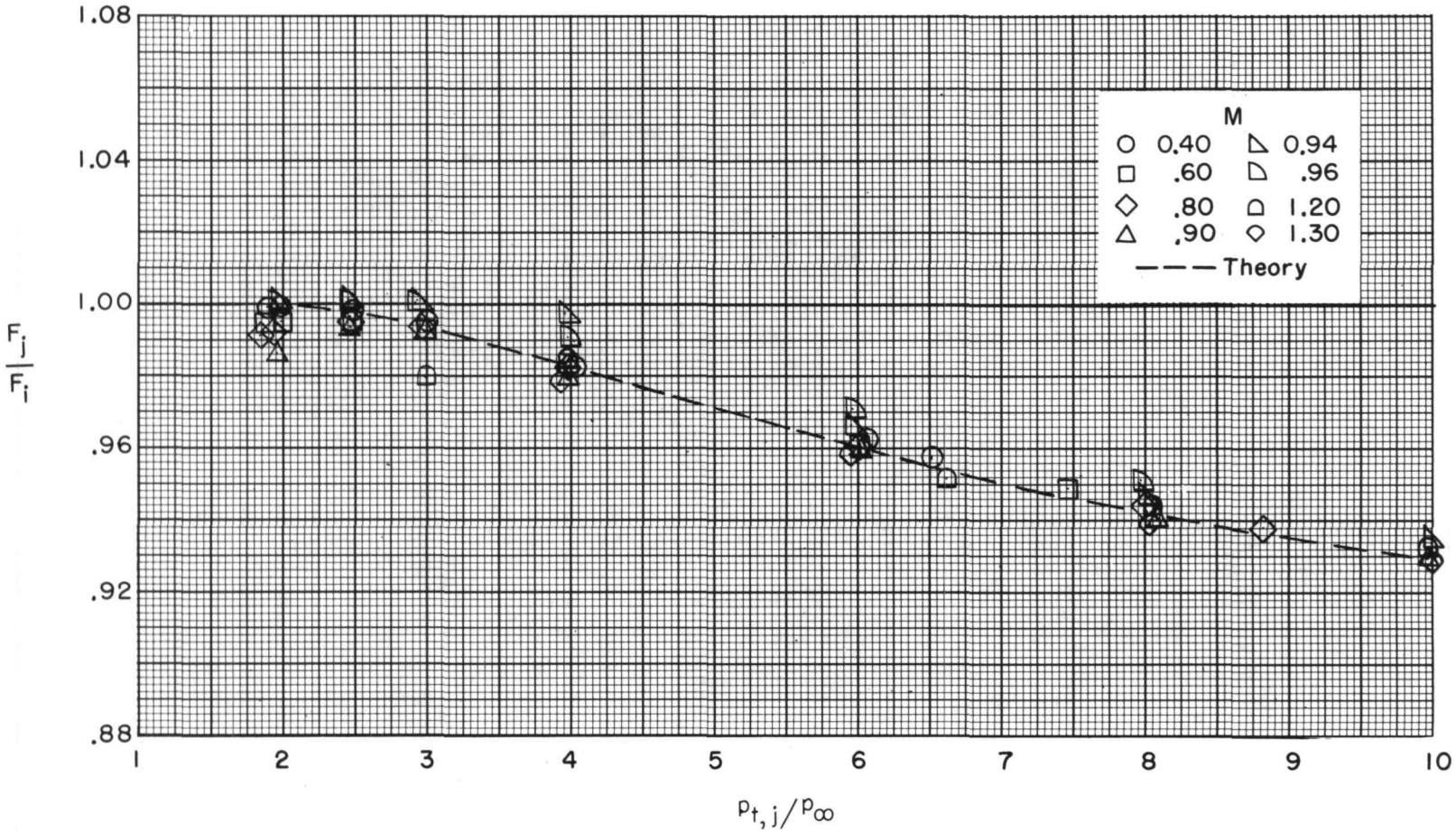

(b) STA configuration.

Figure 35.- Concluded.

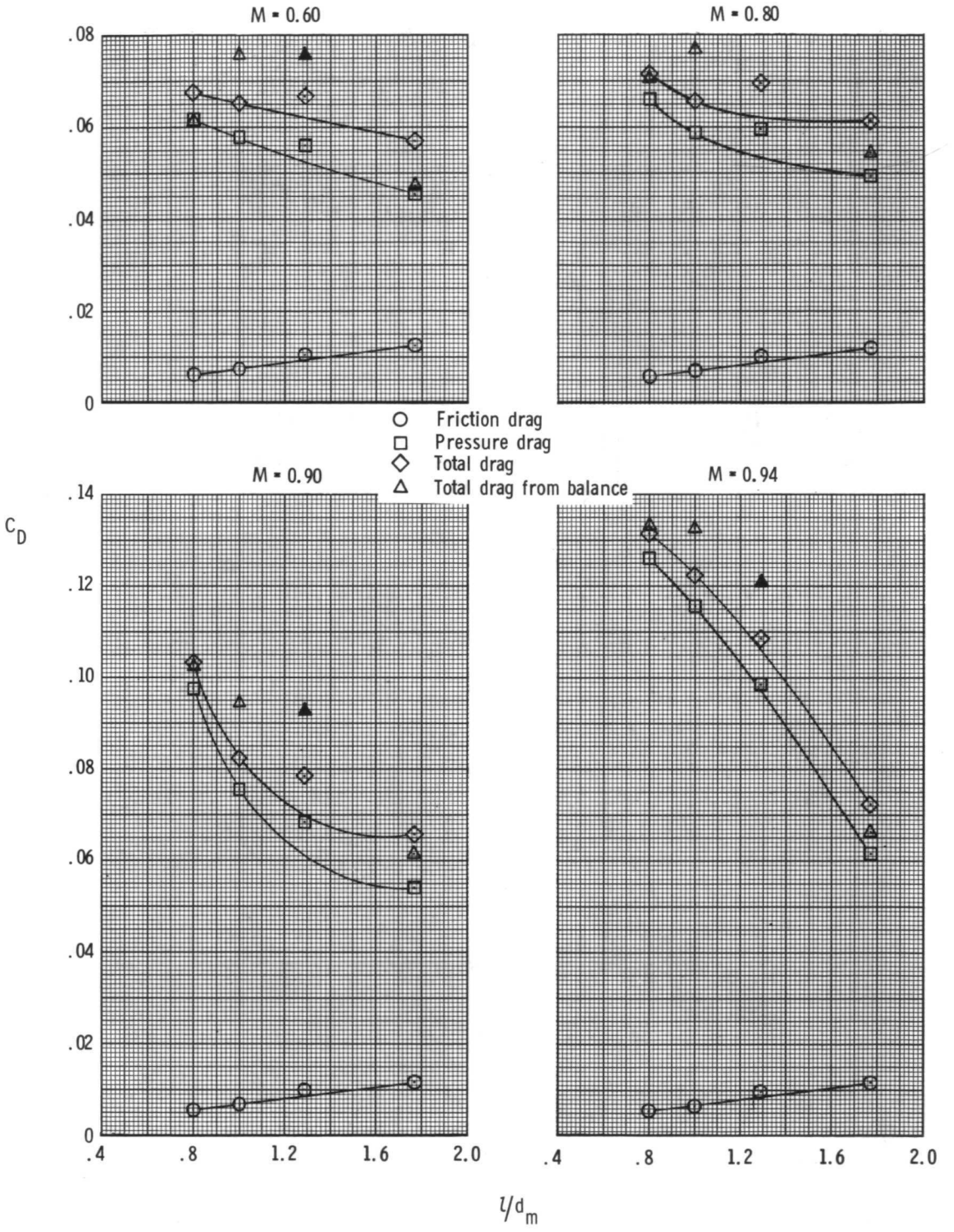

(a) M = 0.60, 0.80, 0.90, and 0.94.

Figure 36.- Comparison of jet-off drag coefficients based on pressure data with those based on force data. STA data shown as solid symbols because they are known to be high.

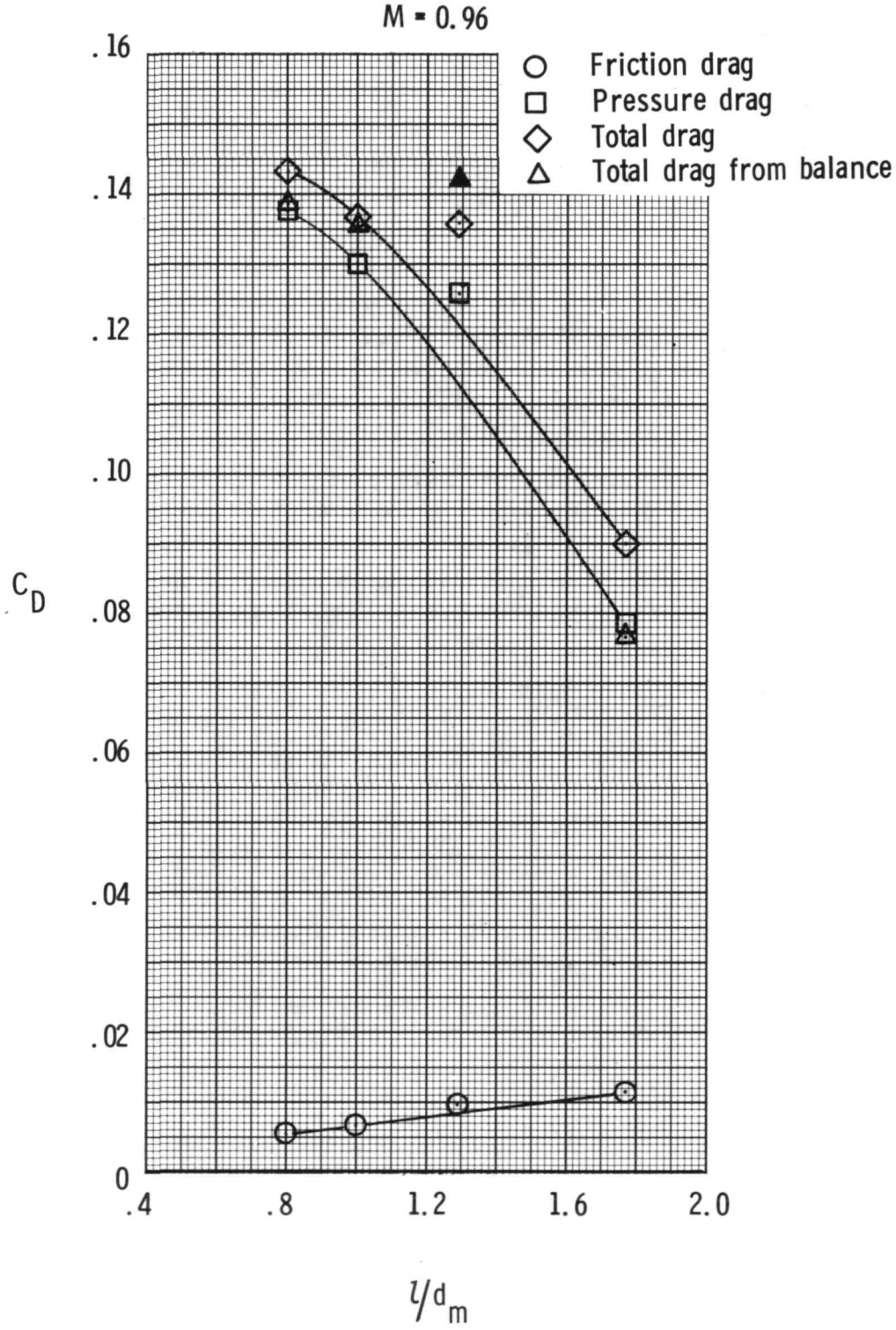

(b) M = 0.96.

Figure 36.- Concluded.

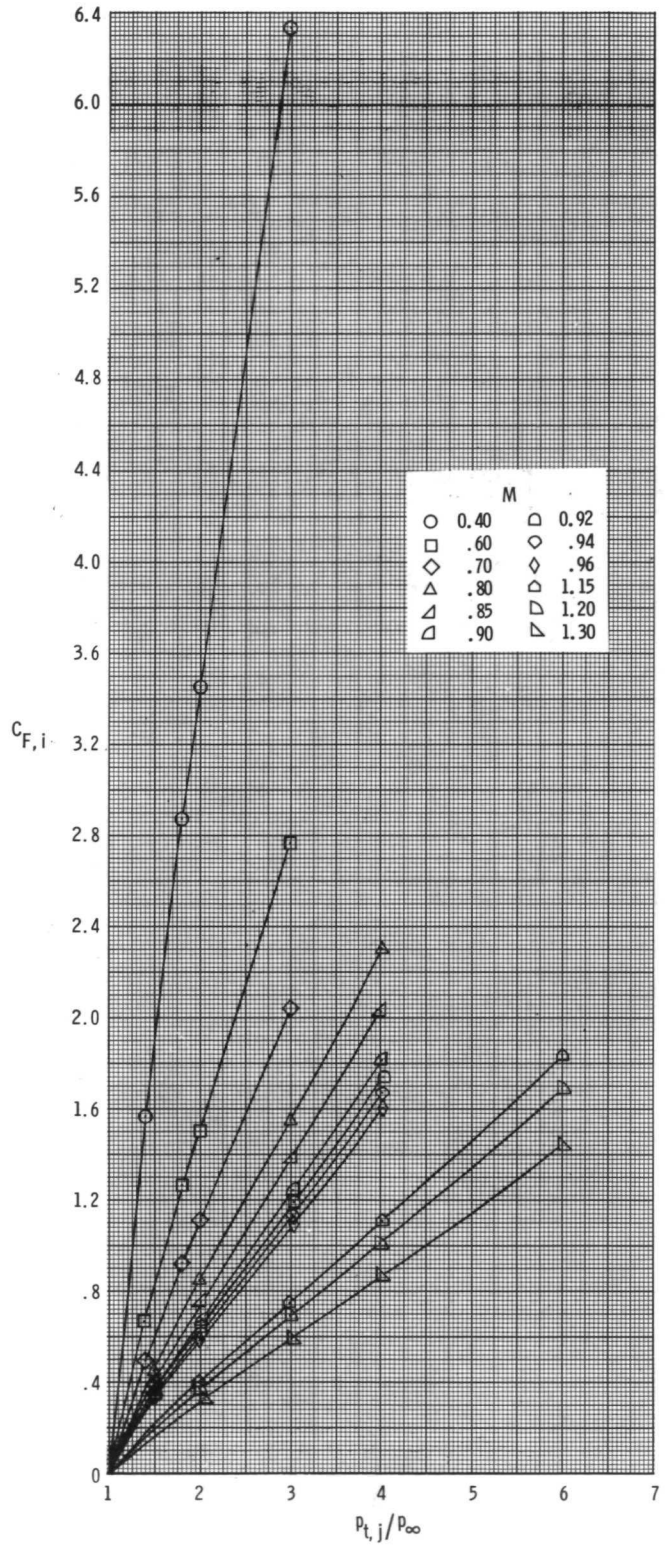

Figure 37.- Variation of aerodynamic ideal thrust coefficient with jet total-pressure ratio.

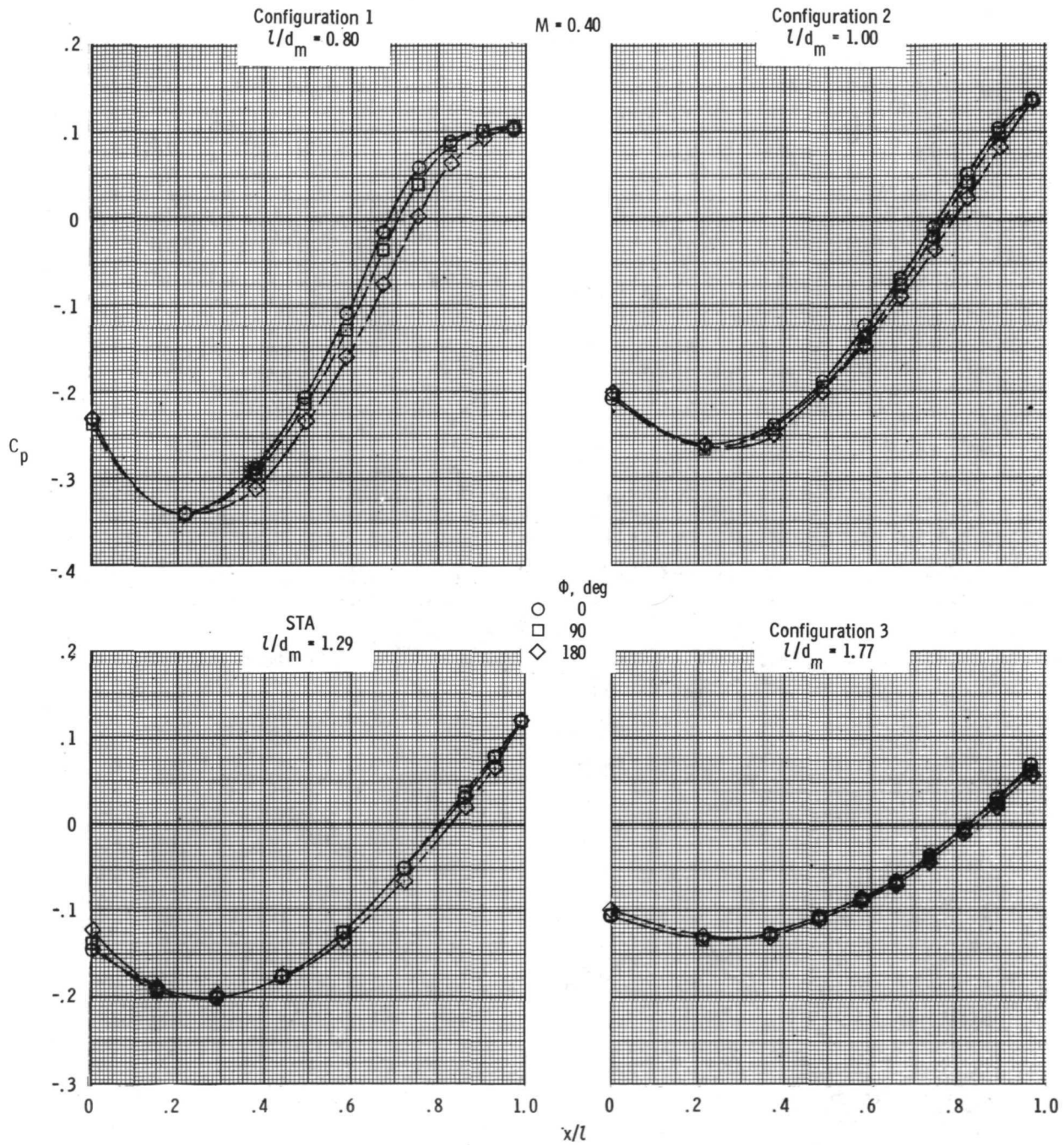

(a) M = 0.40.

Figure 38.- Jet-off boattail longitudinal pressure coefficient distributions for several values of ϕ at three selected Mach numbers.

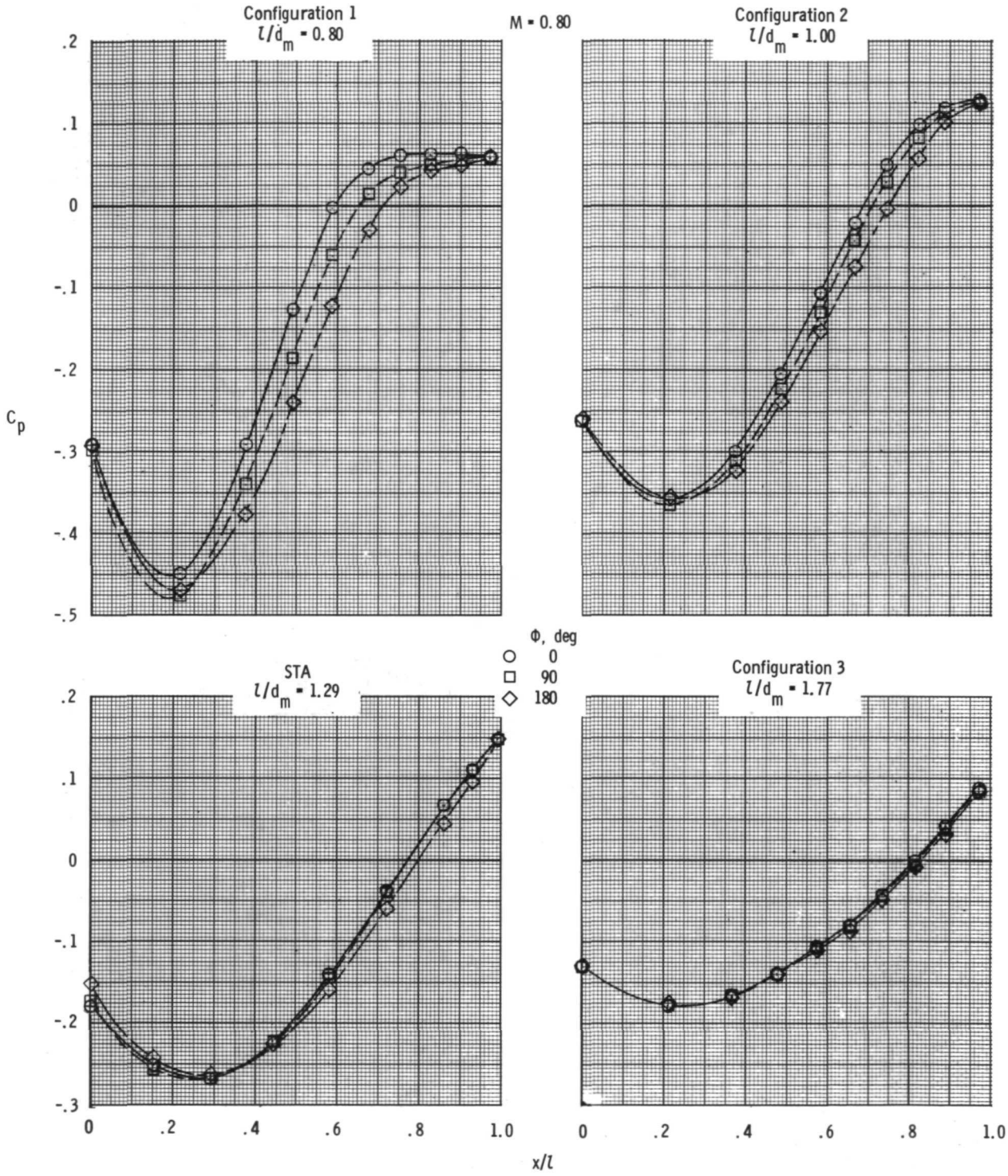

(b) M = 0.80.

Figure 38.- Continued.

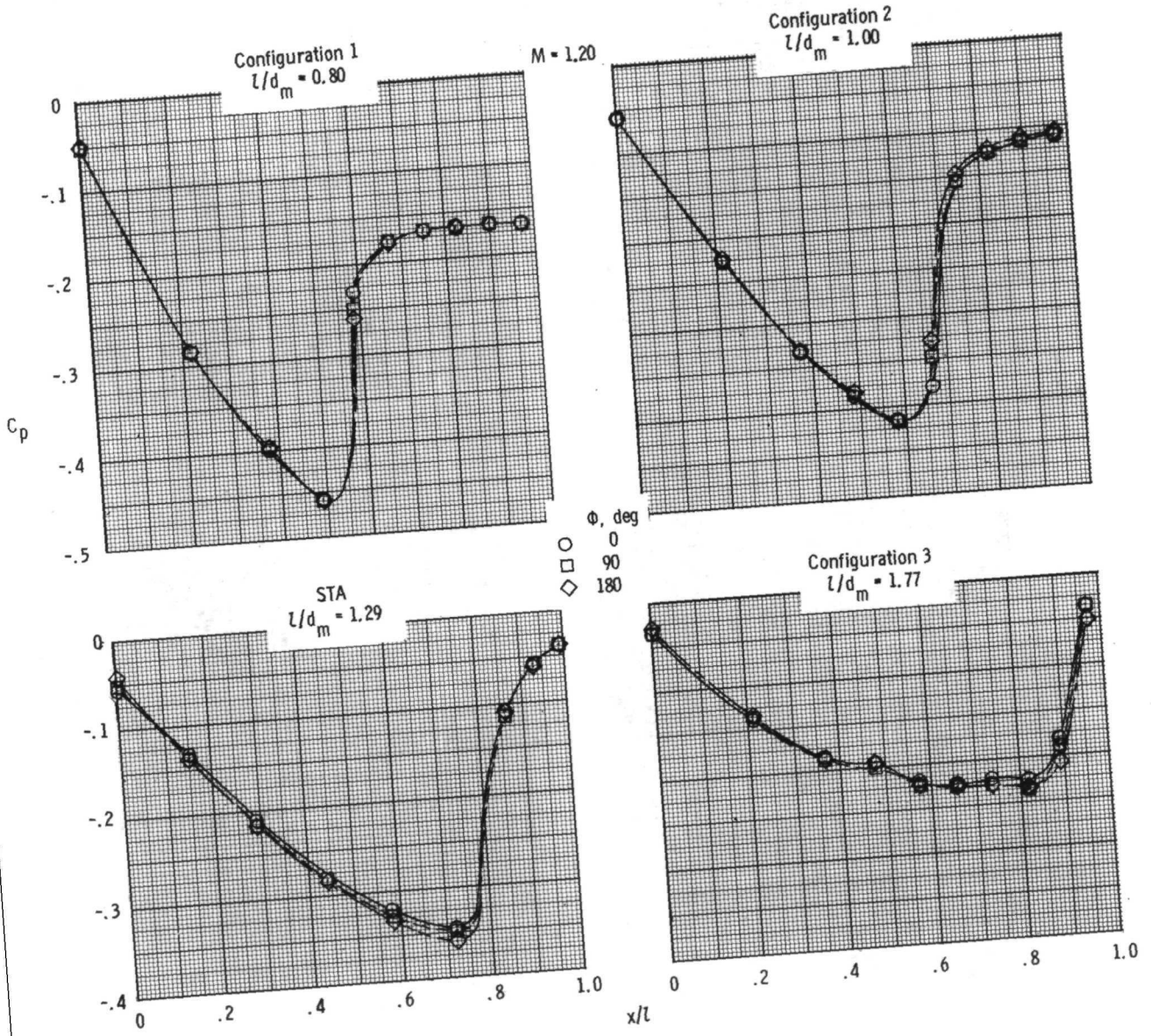

(c) M = 1.20.

Figure 38.- Concluded.

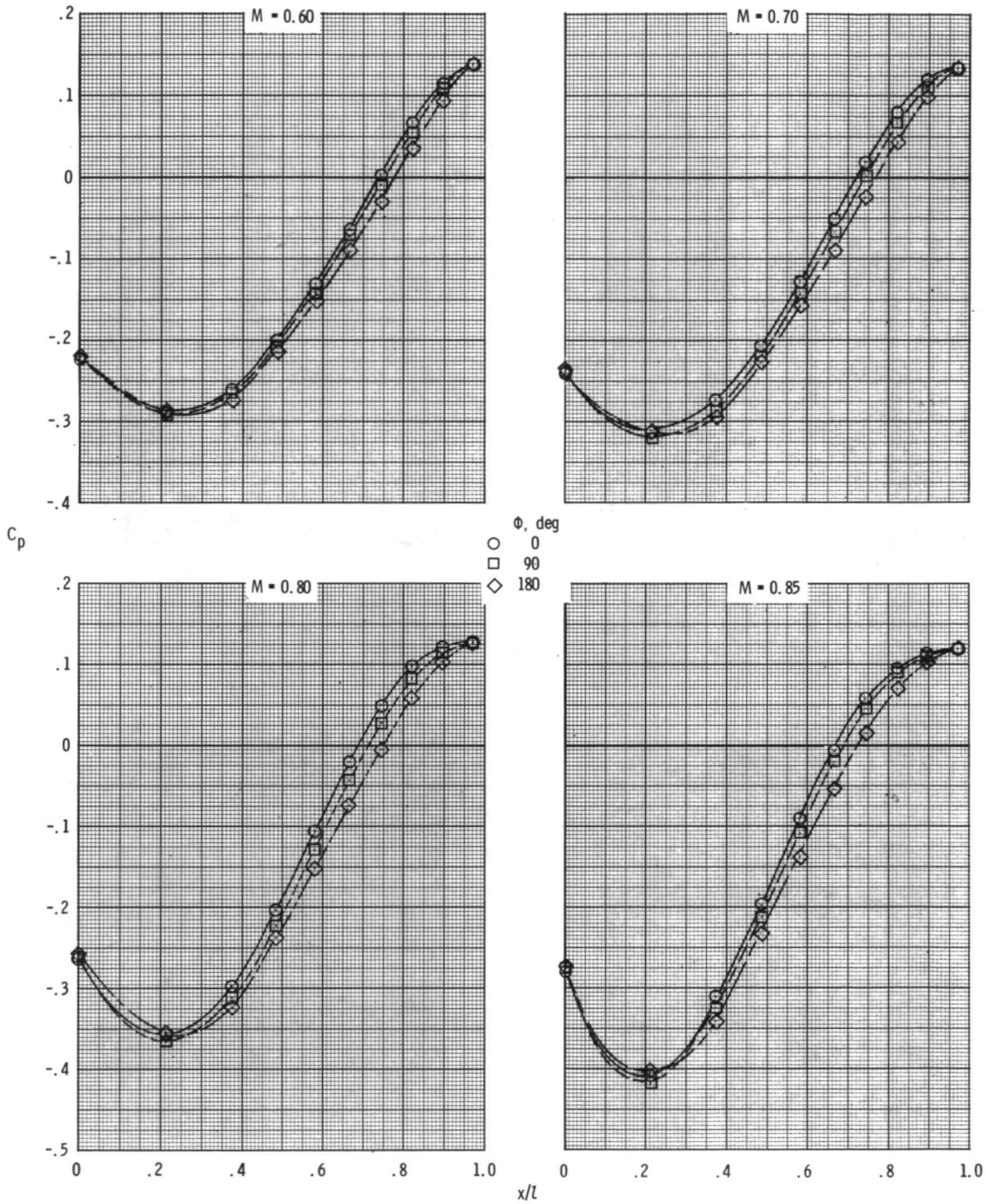

(a) M = 0.60, 0.70, 0.80, and 0.85.

Figure 39.- Jet-off boattail longitudinal pressure coefficient distributions for configuration 2 $\left(l/d_m = 1.00\right)$ for several values of ϕ at various Mach numbers.

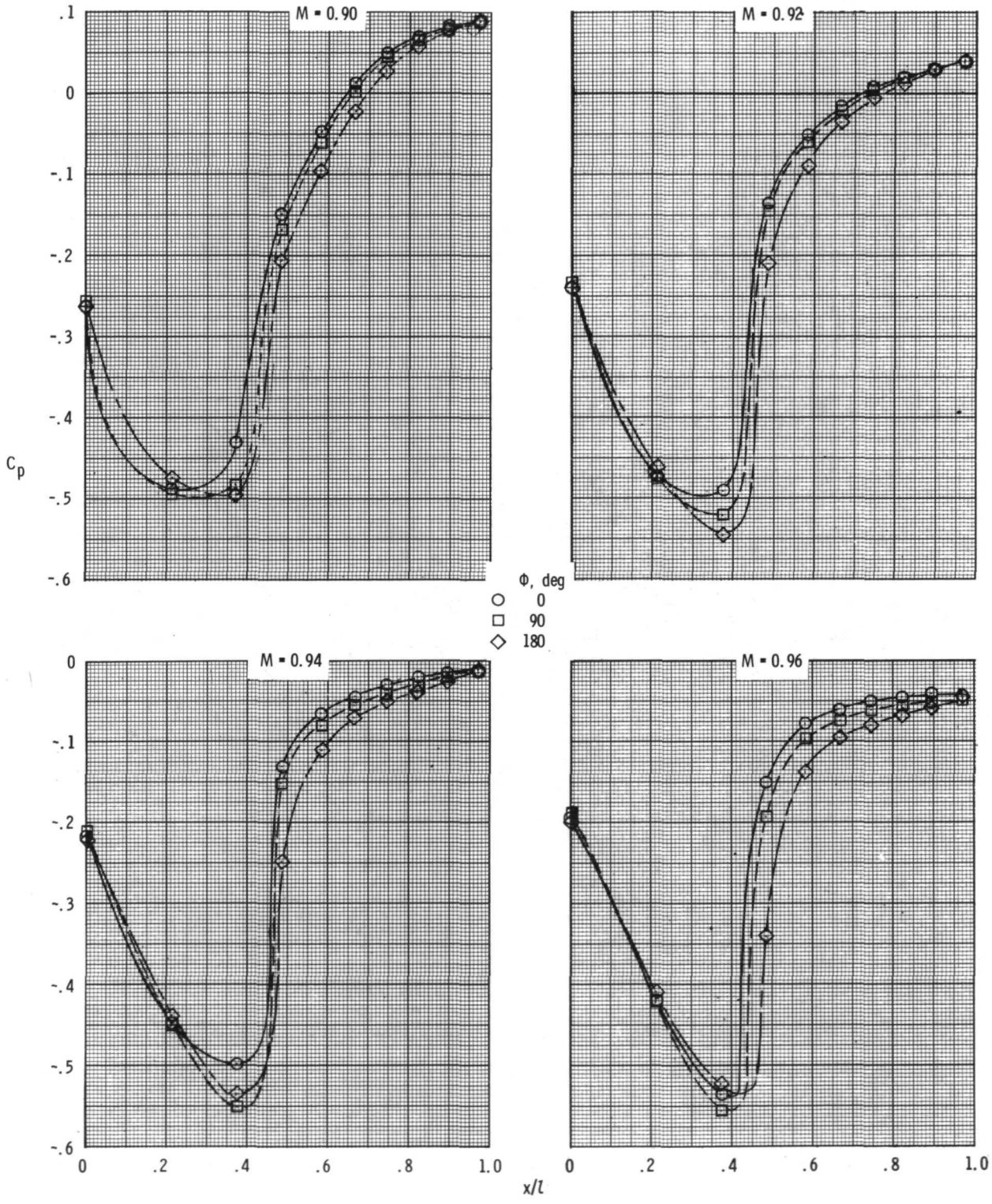

(b) M = 0.90, 0.92, 0.94, and 0.96.

Figure 39.- Concluded.

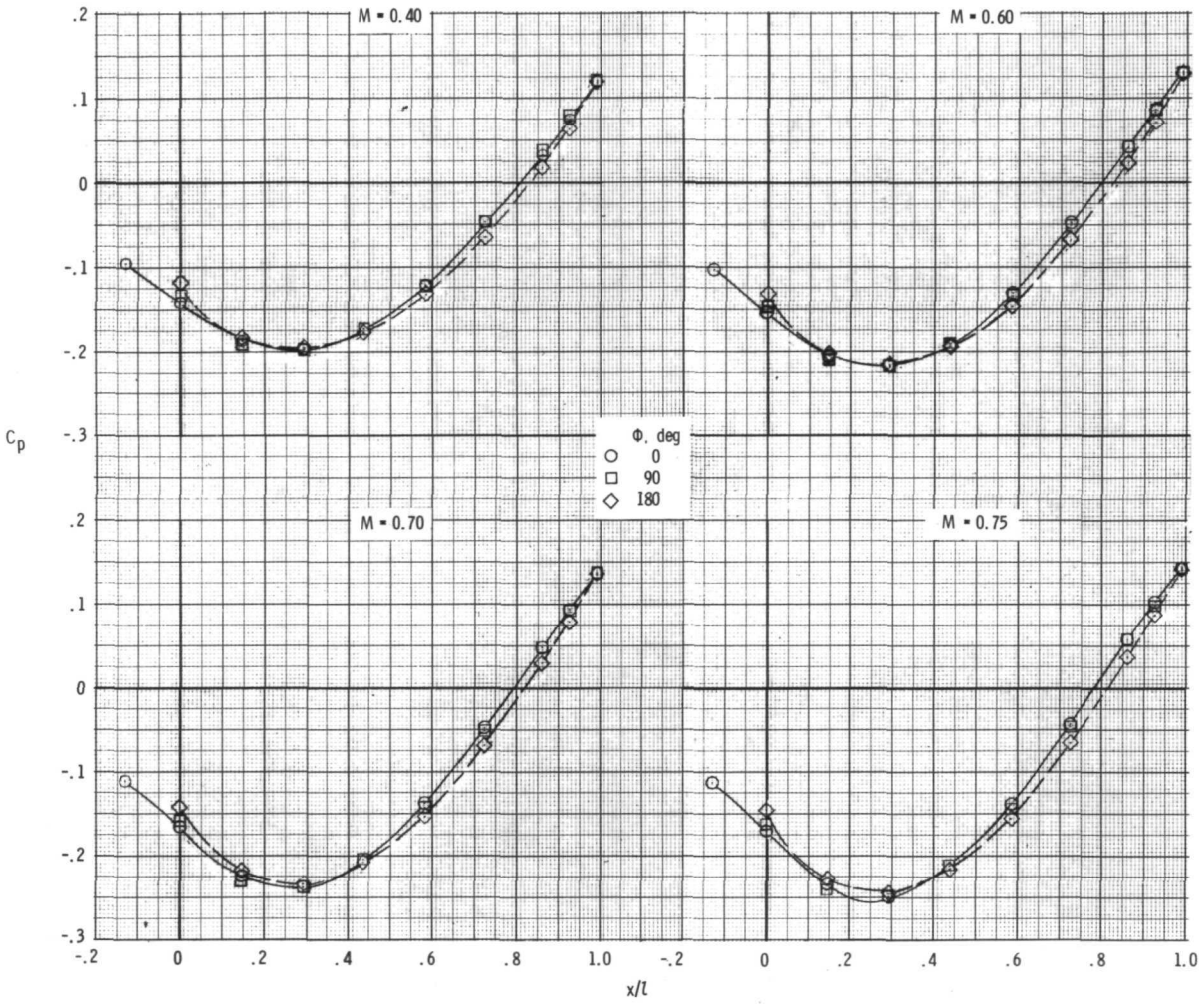

(a) M = 0.40, 0.60, 0.70, and 0.75.

Figure 40.- Jet-off boattail longitudinal pressure coefficient distributions for STA configuration $\left(l/d_m = 1.29\right)$ at several values of ϕ at various Mach numbers.

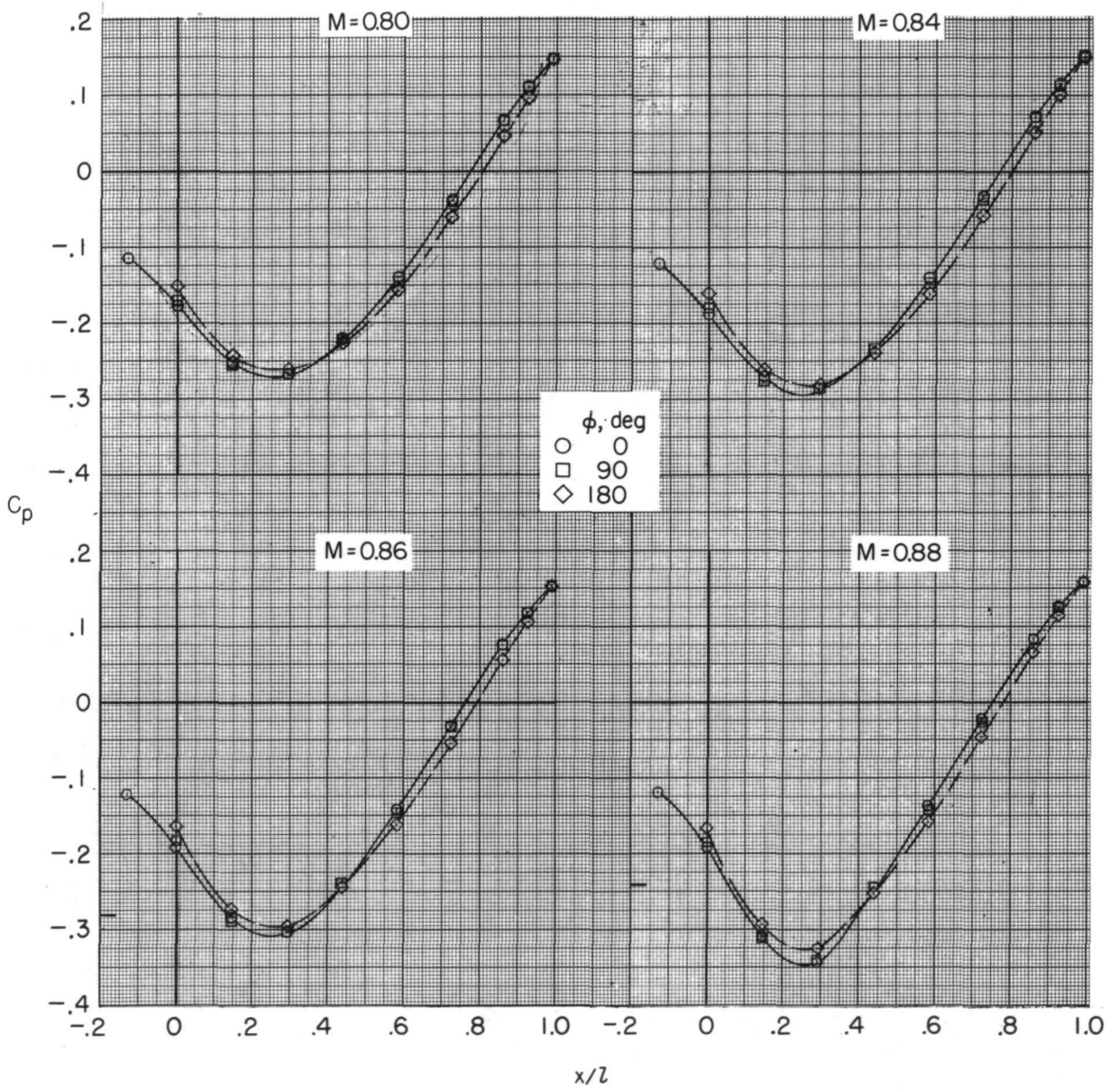

(b) M = 0.80, 0.84, 0.86, and 0.88.

Figure 40.- Continued.

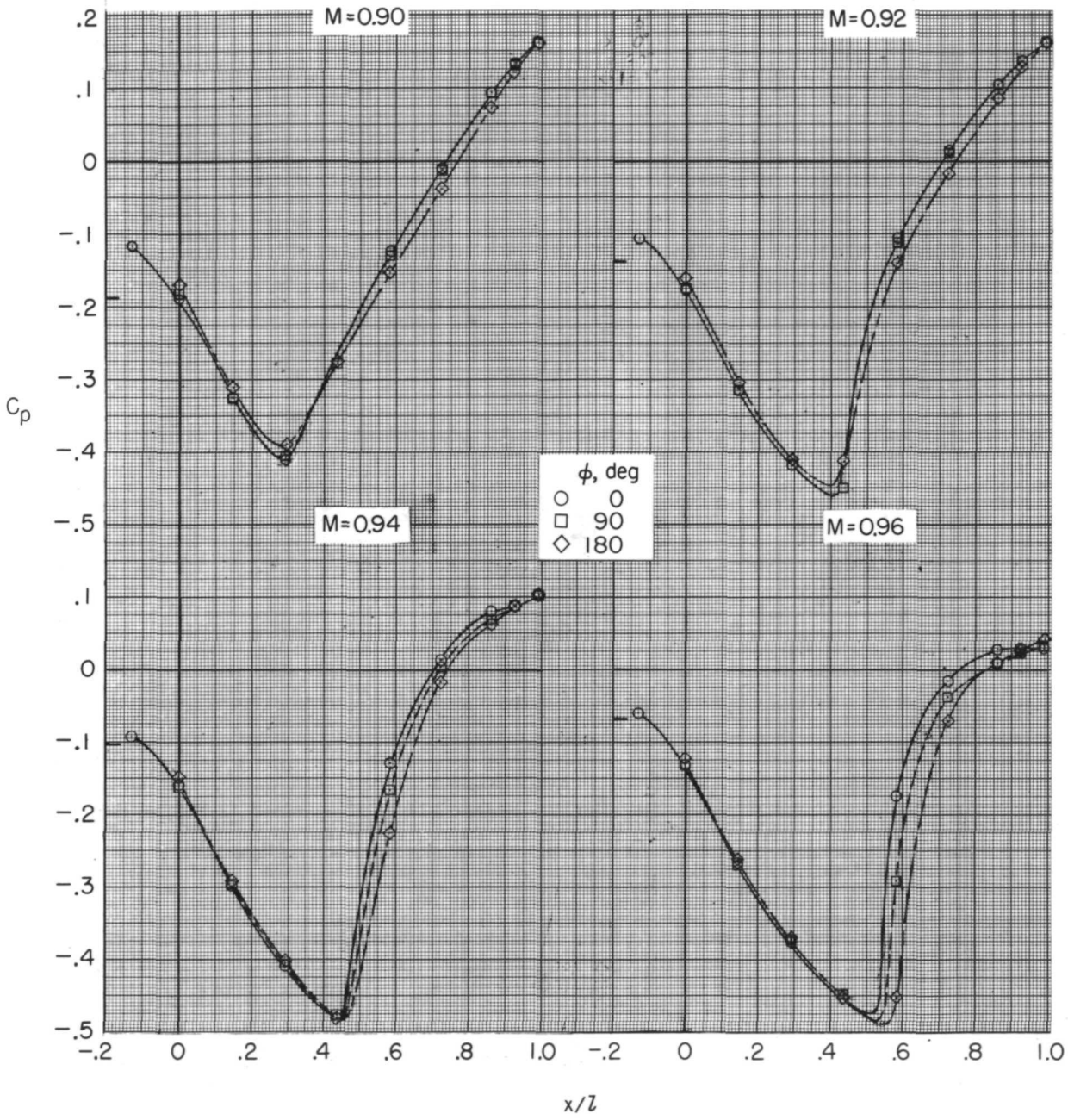

(c) M = 0.90, 0.92, 0.94, and 0.96.

Figure 40.- Concluded.

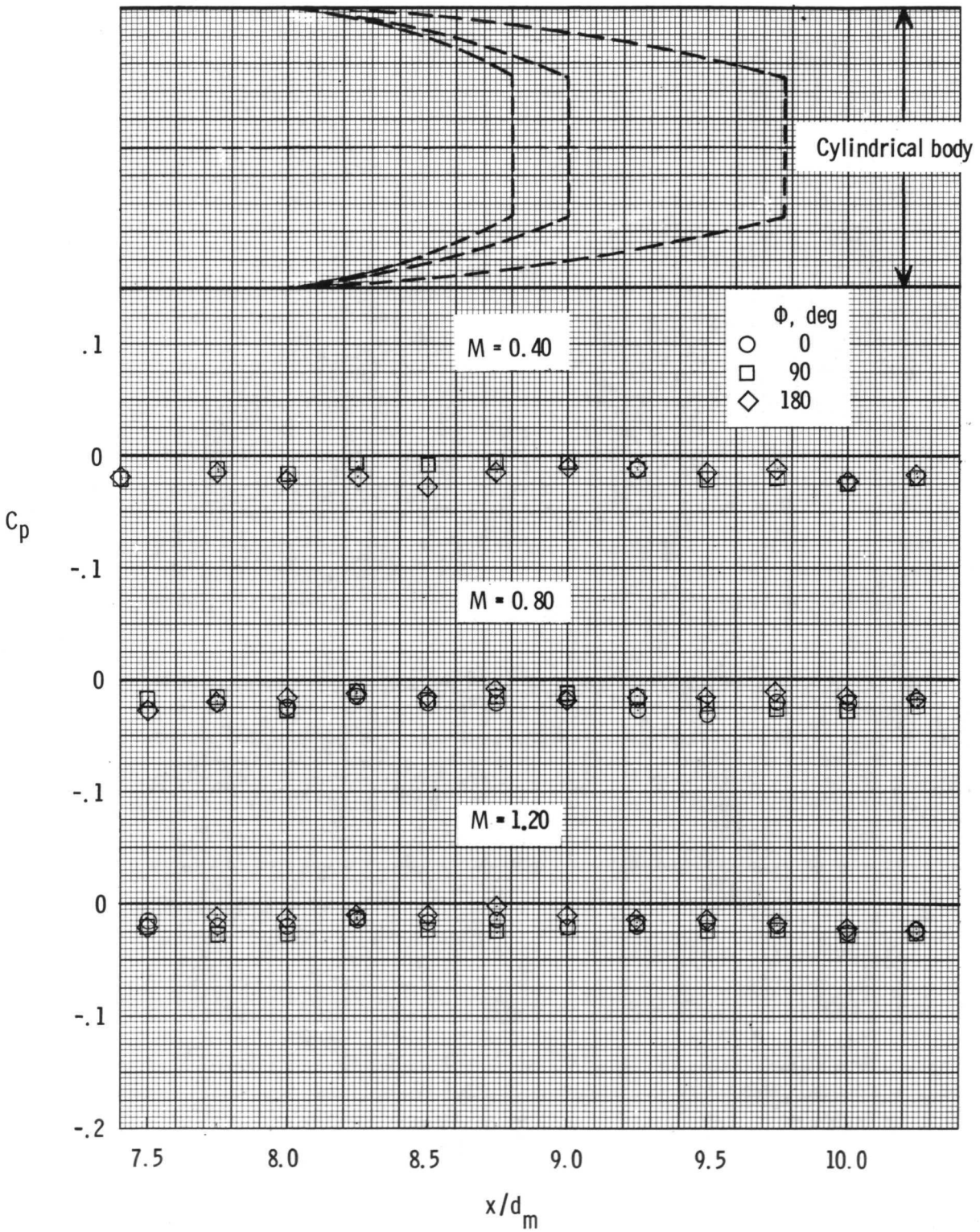

Figure 41.- Pressure coefficients at three values of ϕ for cylindrical afterbody.

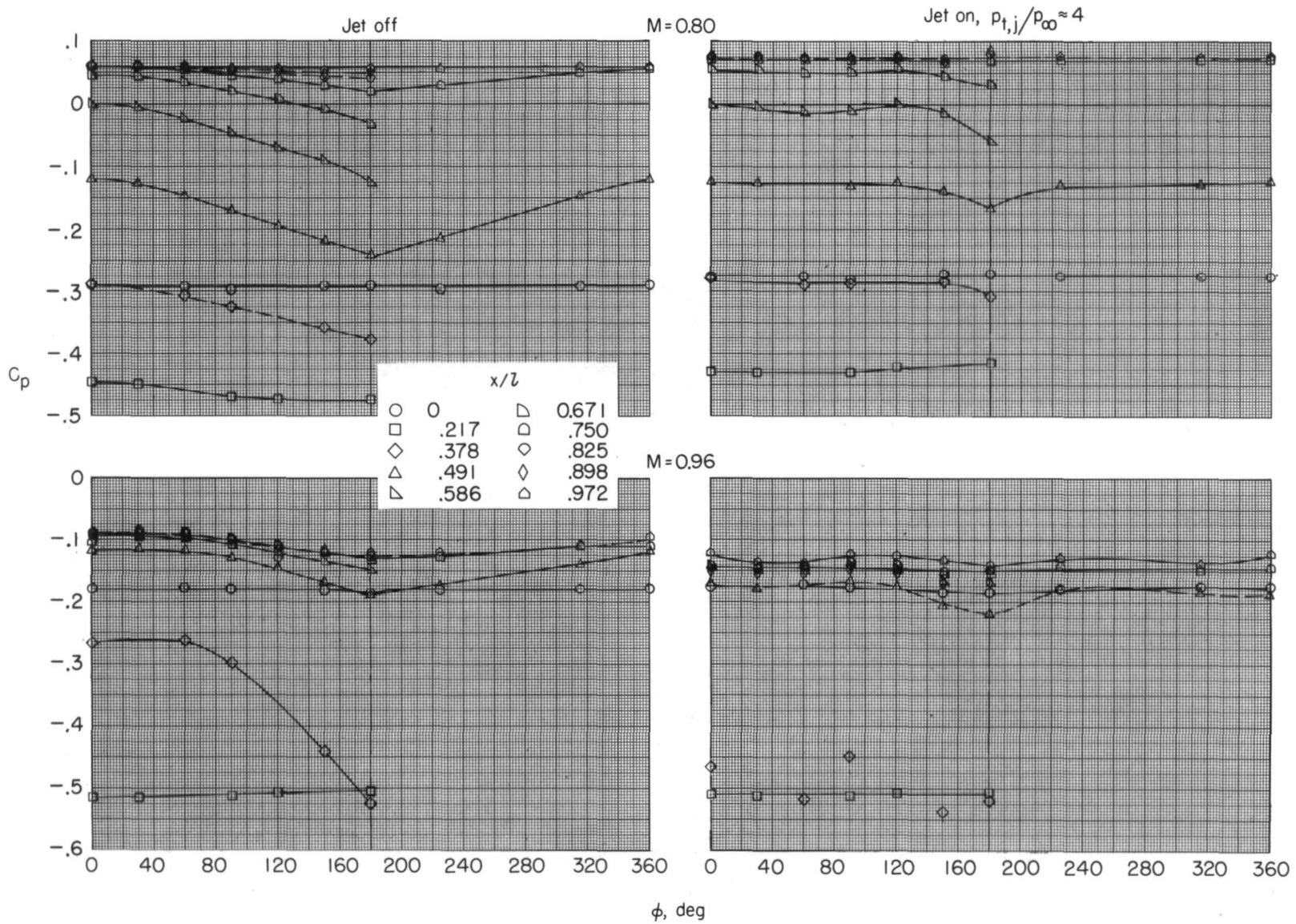

(a) Configuration 1 $(l/d_m = 0.80)$.

Figure 42.- Variation of boattail pressure coefficients with ϕ for two Mach numbers and various x/l stations.

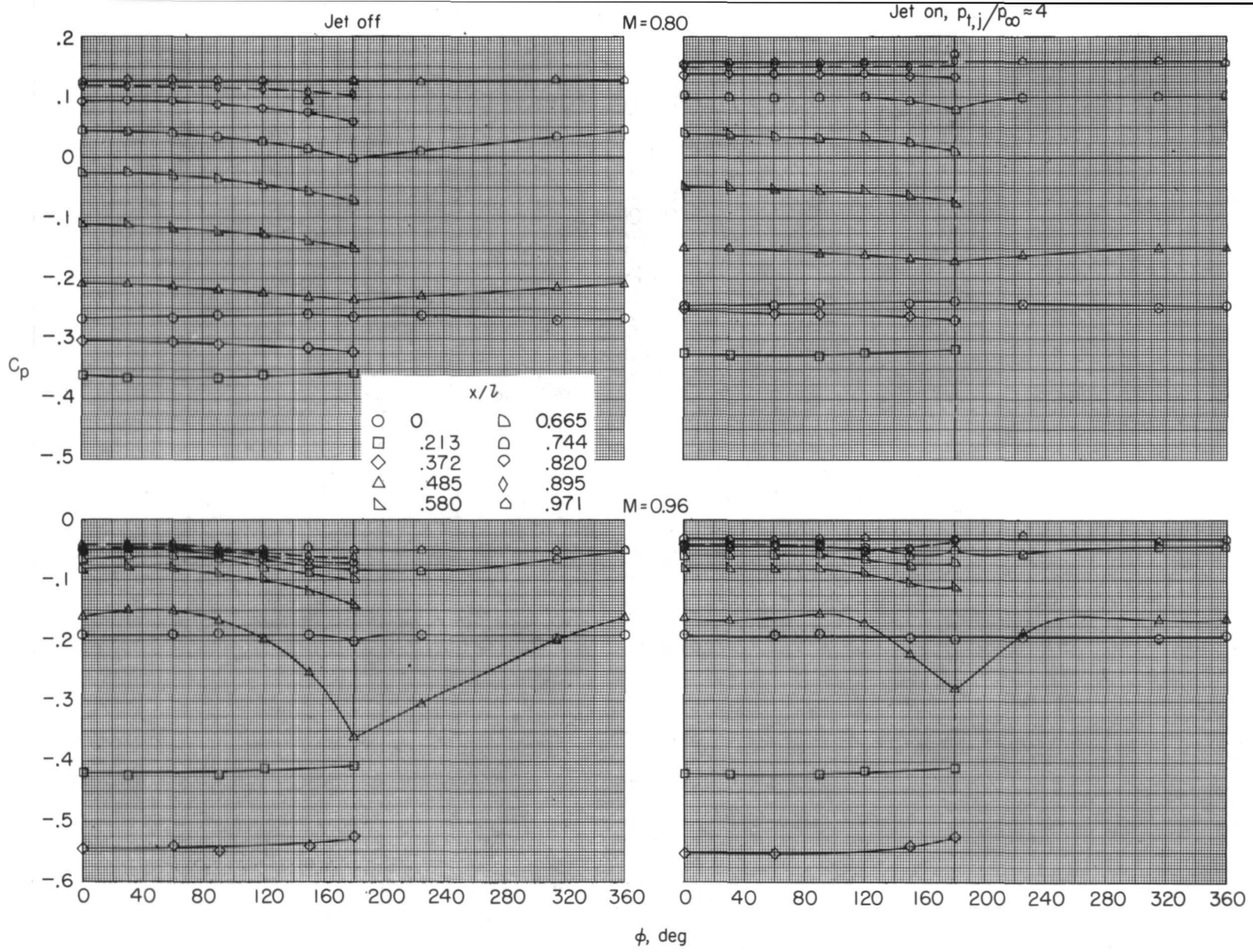

(b) Configuration 2 $\left(l/d_m = 1.00\right)$.

Figure 42.- Continued.

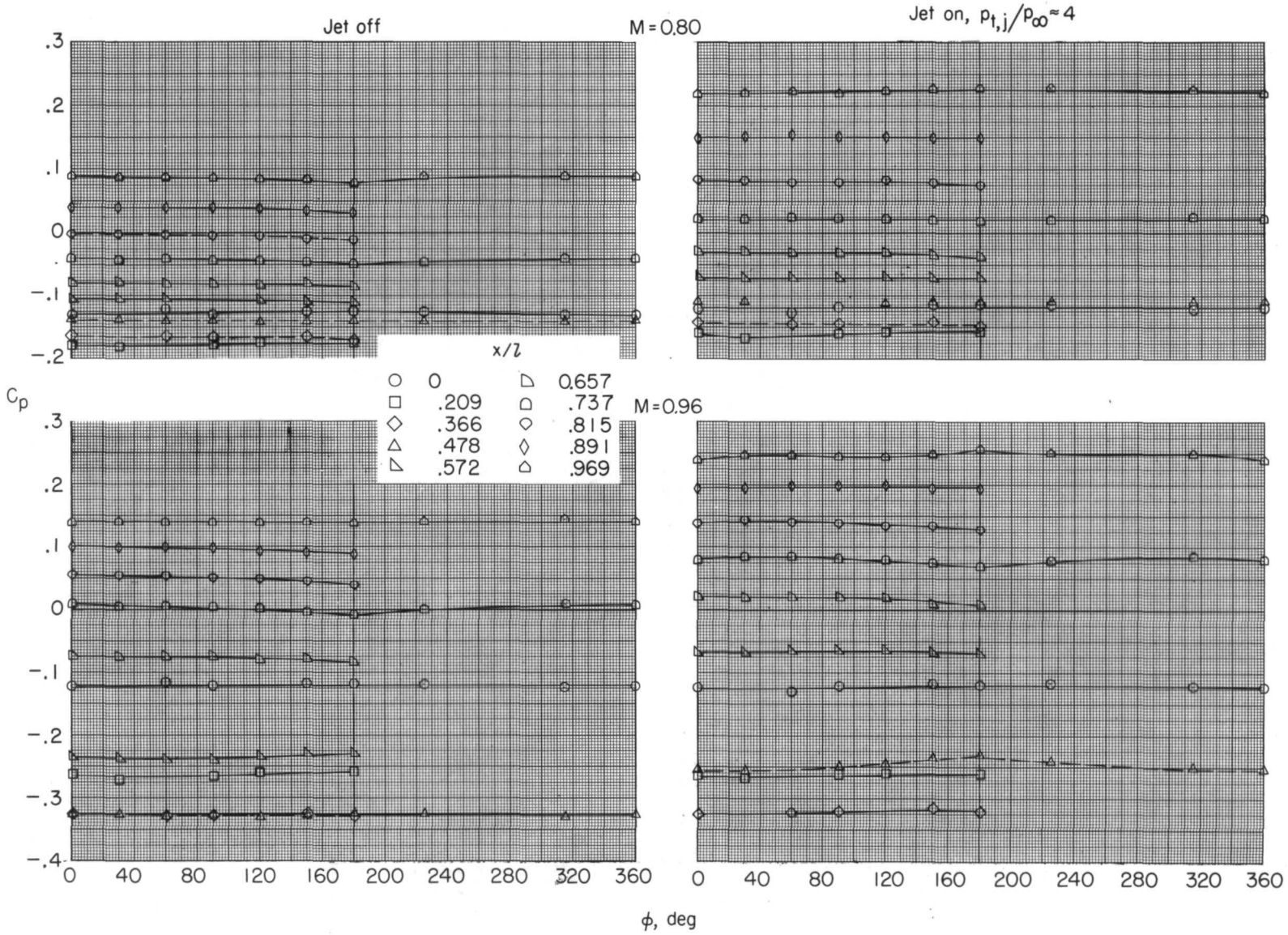

(c) Configuration 3 $\left(l/d_m = 1.77\right)$.

Figure 42.- Concluded.

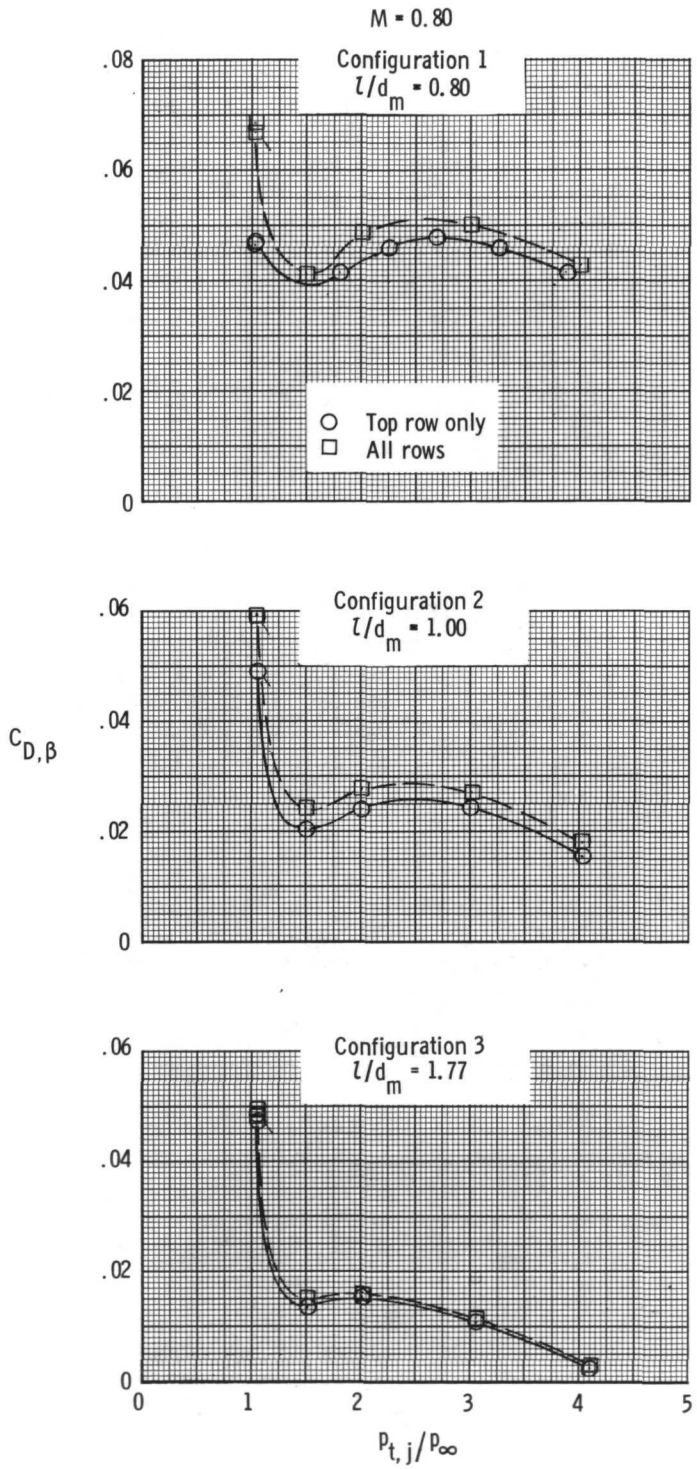

(a) M = 0.80.

Figure 43.- Comparison of boattail-pressure-drag variation with jet total-pressure ratio for integrations based on all orifices and on the top row of orifices only at two Mach numbers. Flags on symbols indicate repeat points.

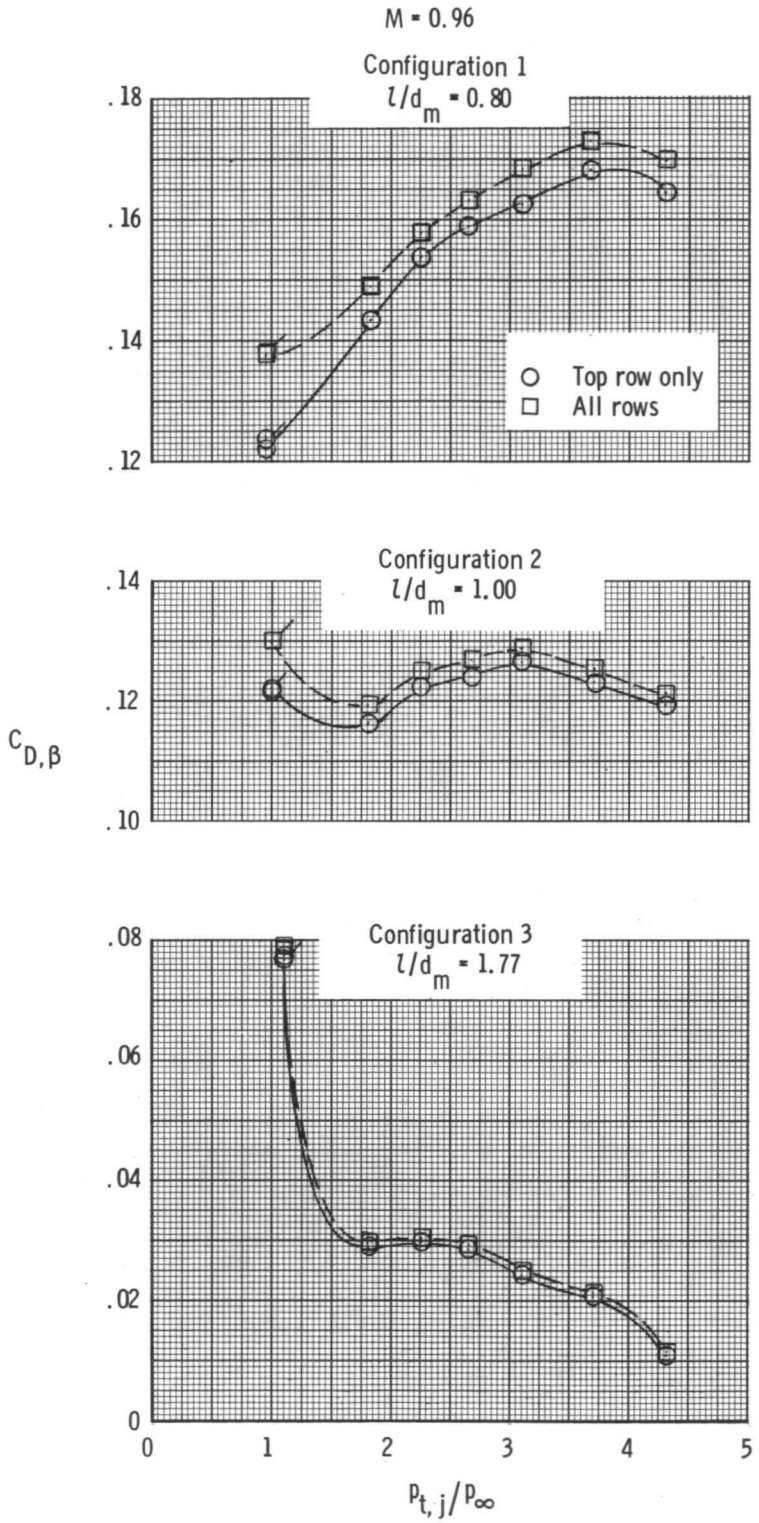

(b) M = 0.96.

Figure 43.- Concluded.

NASA-Langley, 1973 —— 28 L-8705

NATIONAL AERONAUTICS AND SPACE ADMINISTRATION
WASHINGTON, D.C. 20546

OFFICIAL BUSINESS
PENALTY FOR PRIVATE USE $300

SPECIAL FOURTH-CLASS RATE
BOOK

POSTAGE AND FEES PAID
NATIONAL AERONAUTICS AND
SPACE ADMINISTRATION
451

U.S.MAIL

POSTMASTER : If Undeliverable (Section 158 Postal Manual) Do Not Return

"The aeronautical and space activities of the United States shall be conducted so as to contribute . . . to the expansion of human knowledge of phenomena in the atmosphere and space. The Administration shall provide for the widest practicable and appropriate dissemination of information concerning its activities and the results thereof."

—NATIONAL AERONAUTICS AND SPACE ACT OF 1958

NASA SCIENTIFIC AND TECHNICAL PUBLICATIONS

TECHNICAL REPORTS: Scientific and technical information considered important, complete, and a lasting contribution to existing knowledge.

TECHNICAL NOTES: Information less broad in scope but nevertheless of importance as a contribution to existing knowledge.

TECHNICAL MEMORANDUMS: Information receiving limited distribution because of preliminary data, security classification, or other reasons. Also includes conference proceedings with either limited or unlimited distribution.

CONTRACTOR REPORTS: Scientific and technical information generated under a NASA contract or grant and considered an important contribution to existing knowledge.

TECHNICAL TRANSLATIONS: Information published in a foreign language considered to merit NASA distribution in English.

SPECIAL PUBLICATIONS: Information derived from or of value to NASA activities. Publications include final reports of major projects, monographs, data compilations, handbooks, sourcebooks, and special bibliographies.

TECHNOLOGY UTILIZATION PUBLICATIONS: Information on technology used by NASA that may be of particular interest in commercial and other non-aerospace applications. Publications include Tech Briefs, Technology Utilization Reports and Technology Surveys.

Details on the availability of these publications may be obtained from:

SCIENTIFIC AND TECHNICAL INFORMATION OFFICE

NATIONAL AERONAUTICS AND SPACE ADMINISTRATION

Washington, D.C. 20546